HORIZON 2020
The EU Framework Programme for Research and Innovation

European Commission

Urban Cross-cutting Applications Methods

Deliverable D3.2

DATE
31 December 2021

ISSUE
1.0

GRANT AGREEMENT
no 870337

DISSEMINATION LEVEL
PU

PROJECT WEB-SITE
http://cure-copernicus.eu/

LEAD AUTHOR
Dirk Lauwaet (VITO)

CO-AUTHORS
Nektarios Chrysoulakis, Zina Mitraka, Giannis Lantzanakis (FORTH), Benjamin Leutner, Mattia Marconcini (DLR), Christian Feigenwinter (UNIBAS), Katerina Jupova, Jan Kolomaznik, Miroslav Kopecky, Erika Orlitova, Tomas Soukup (GISAT), Hans Hooyberghs (VITO), Alessandra Gandini, Laura Gutierrez, Efren Feliu (TECNALIA), Birgitte Holt Andersen, Louise Kjær-Hansen (CWare)

CONTENTS

LIST OF TABLES

LIST OF FIGURES

1 INTRODUCTION

1.1 Purpose of this document

This document is the second deliverable of Work Package (WP) 3 of the CURE (Copernicus for Urban Resilience in Europe) Project, Deliverable D3.2 'Urban Cross-cutting Applications Methods'. The goal of this deliverable is to describe the final updated methodology of the CURE Cross-Cutting Applications (after their first description in Deliverable 3.1) and to describe and explain in more detail the sample results for the front-runner and follower cities that are submitted in Deliverable 3.3.

The CURE applications are developed for at least one front-runner city and one or more follower cities. Table 1 lists the applications per city, as decided after consultation with the users (detailed in D1.1).

Figure 1 shows the dependency of the CURE applications to the Copernicus Core Services.

In the next Chapters, the applications are presented one by one, in the same order as Table 1.

Table 1. CURE Applications study sites.

AP	Cross-cutting applications	Berlin	Copenhagen	Sofia	Heraklion	Bristol	Ostrava	Basel	Munich	Vitoria-Gasteiz	San Sebastian
01	Local Scale Surface Temperature Dynamics (FORTH)	●	●	●	●	●	●	●	●	●	●
02	Surface Urban Heat Island Assessment (DLR)	●	●	●	●	●	●	●	●	●	●
03	Urban Heat Emissions Monitoring (UNIBAS)				●			●			
04	Urban CO$_2$ Emissions Monitoring (UNIBAS)				●			●			
05	Urban Flood Risk (GISAT)				●		●				
06	Urban Subsidence, Movements and Deformation Risk (GISAT)				●		●				
07	Urban Air Quality (VITO)			●		●	●				
08	Urban Thermal Comfort (VITO)		●	●				●			●
09	Urban Heat Storage Monitoring (FORTH)				●				●		
10	Nature Based Solutions (TECNALIA)			●						●	●
11	Health Impacts (socioeconomic perspective) (ApHER)		●	●		●					
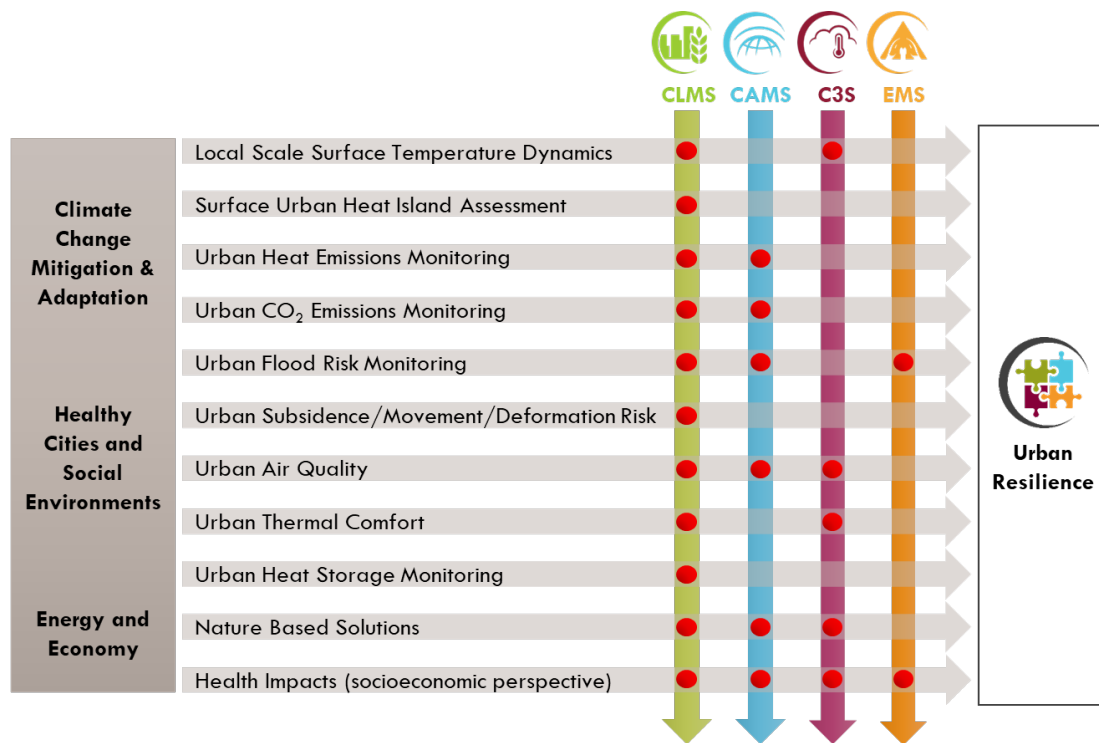
Figure 1. *CURE cross-cutting applications among the Copernicus Core Services.*

1.2 Definitions and acronyms

Acronyms

AOI	Area of Interest
ARM	Aerodynamic Resistance Method
C3S	Copernicus Climate Change Service
CAMS	Copernicus Atmospheric Service
CLMS	Copernicus Land Monitoring Service
CURE	Copernicus for Urban Resilience in Europe
DOM	Digital Object Model
DSM	Digital Surface Model
DTM	Detailed terrain model
EC	Eddy Covariance
EMS	Copernicus Emergency Service
EO	Earth Observation
EVA	Economic Valuation of Air pollution
IFDM	Immission Frequency Distribution Model
IMD HRL	imperviousness density
InSAR	Synthetic Aperture Radar Interferometry
LST	Land Surface Temperature
MOST	Monin-Obukhov similarity theory
NBS	Nature-based solutions
NRT	Near Real Time
PSI	Persistent Scatterer Interferometry
QA/QC	quality assessment and quality control
SUHII	Surface Heat Island Intensity Indicator
UHI	Urban Heat Island
UHII	UHI indicators
UMEP	Urban Multi-scale Environmental Predictor
WP	Work Package
WSFE	World Surface Footprint Evolution

2 AP01 LOCAL SCALE SURFACE TEMPERATURE DYNAMICS

2.1 Final Input Data & Methodology

2.1.1 Data

AP01 is implemented for all CURE front-runners cities: Berlin, Copenhagen, Heraklion and Sofia and all the follower cities: Bristol, Ostrava, Basel, Munich, San Sebastian and Vitoria-Gasteiz.

Table 2 lists the data used for the AP01. AP01 is using data from two Copernicus Services (CLMS and C3S), data from two Copernicus Satellites, Sentinel-2 and Sentinel-3, and very high resolution optical third-party data from the Copernicus Contributing missions Data Warehouse (Copernicus, 2020).

Table 2. Summary of data used for AP01.

Data Source	Description of the Product
CLMS	Imperviousness
CLMS	Urban Atlas
CLMS	Urban Atlas: Building Heights
CLMS	High Resolution Vegetation Phenology and Productivity
C3S	UERRA regional reanalysis for Europe on single levels from 1961 to 2019
C3S	ERA5 hourly data on single levels from 1979 to present
Copernicus Satellite	Sentinel-2, Level-2A Bottom Of Atmosphere (BOA) reflectance images
Copernicus Satellite	Sentinel-3, SLSTR Level-1B thermal imagery
Third-party	Baseline Land Cover from VHR (from the DWH)
Third-party	Material emissivity information from spectral libraries (Kotthaus et al., 2014)

2.1.2 Methodology

The CURE methodology for deriving the local scale urban surface temperature dynamics is outlined in Figure 2. Data from various sources, including the CLMS, are used to achieve the surface characterization and this information is then used to estimate the urban surface emissivity and to downscale the thermal imagery in order to retrieve land surface temperature (LST), given atmospheric information from C3S. The methodology described in Mitraka et al. (2015) is used to downscale the Sentinel-3, 1 km spatial resolution thermal infrared (TIR) imagery, to retrieve the final LST products at local scale (100 m). The methodology for downscaling the thermal bands, requires higher spatial resolution surface cover information. For this VHR land cover information is derived from the VHR optical third-party data available

from the Copernicus Contributing missions Data Warehouse (Copernicus, 2020) is used, as described in D3.5-D3.8. The VHR land cover map is used to derive a local scale (100 m) surface cover fractions map, which contains information on the abundance of each land cover class in 100 m pixel. The surface cover fractions baseline map is updated to capture changes in time, using information from Sentinel-2imagery. Emissivity maps are estimated using the surface cover maps and ancillary information from spectral libraries. The LST time series is estimated from the downscaled TIR information (using the surface cover), the emissivity and C3S water vapour products.
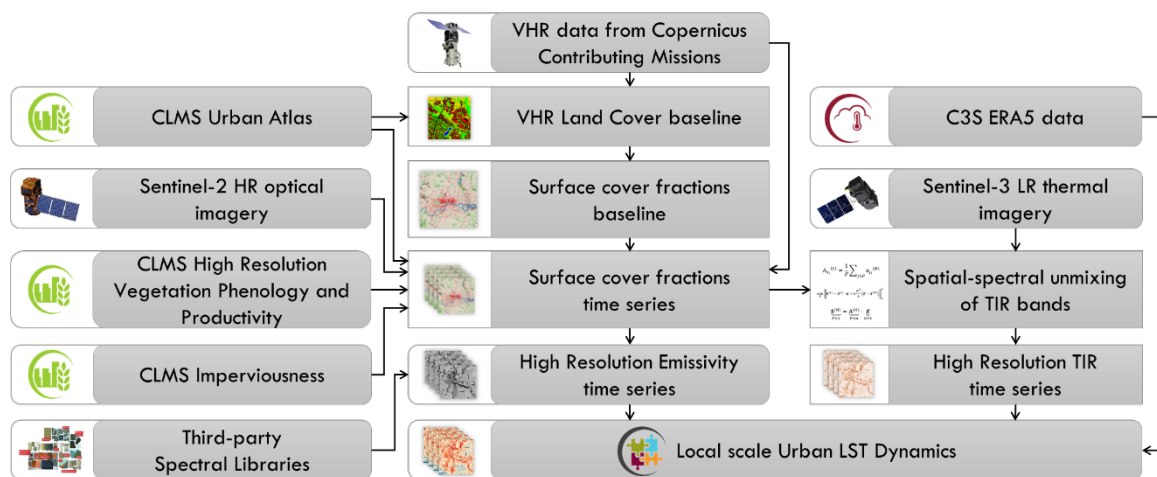
Figure 2. *Methodology for the estimation of Urban Land surface Temperature (LST) dynamics at local scale.*

A surface cover map of very high spatial resolution (2 m) is initially created, from the VHR data available from the DWH (Copernicus, 2020) to serve as baseline, assuming 5 classes (i.e. buildings, paved surfaces, bare soil, vegetation, water surfaces). It is essential to have this information in VHR, to ensure the quality of the resulting products. Surface cover fractions of 100 m spatial resolution are then estimated from the VHR surface cover map, to be used as baseline. The update in time of the baseline map is performed using Sentinel-2 imagery and (when available) CLMS Vegetation Phenology and Productivity data, to capture the changes of the 5 classes.

The vegetation, bare soil and water surfaces classes update is performed using vegetation and water indices approach. The buildings and paved surfaces classes are updated using VHR imagery, CLMS Urban Atlas and CLMS imperviousness data when available and Sentinel-2 optical imagery in the meantime.

The resulting surface cover maps are used to downscale the thermal measurements and to estimate the surface emissivity in local scale using ancillary information from third-party spectral libraries (Mitraka et al., 2012). Different spectral libraries are considered, in order to obtain emissivity information for the different classes. The emissivity information along with the local scale thermal products are then used along with water vapour information from C3S, for the derivation of LST maps using a split-window algorithm (Mitraka et al., 2015).
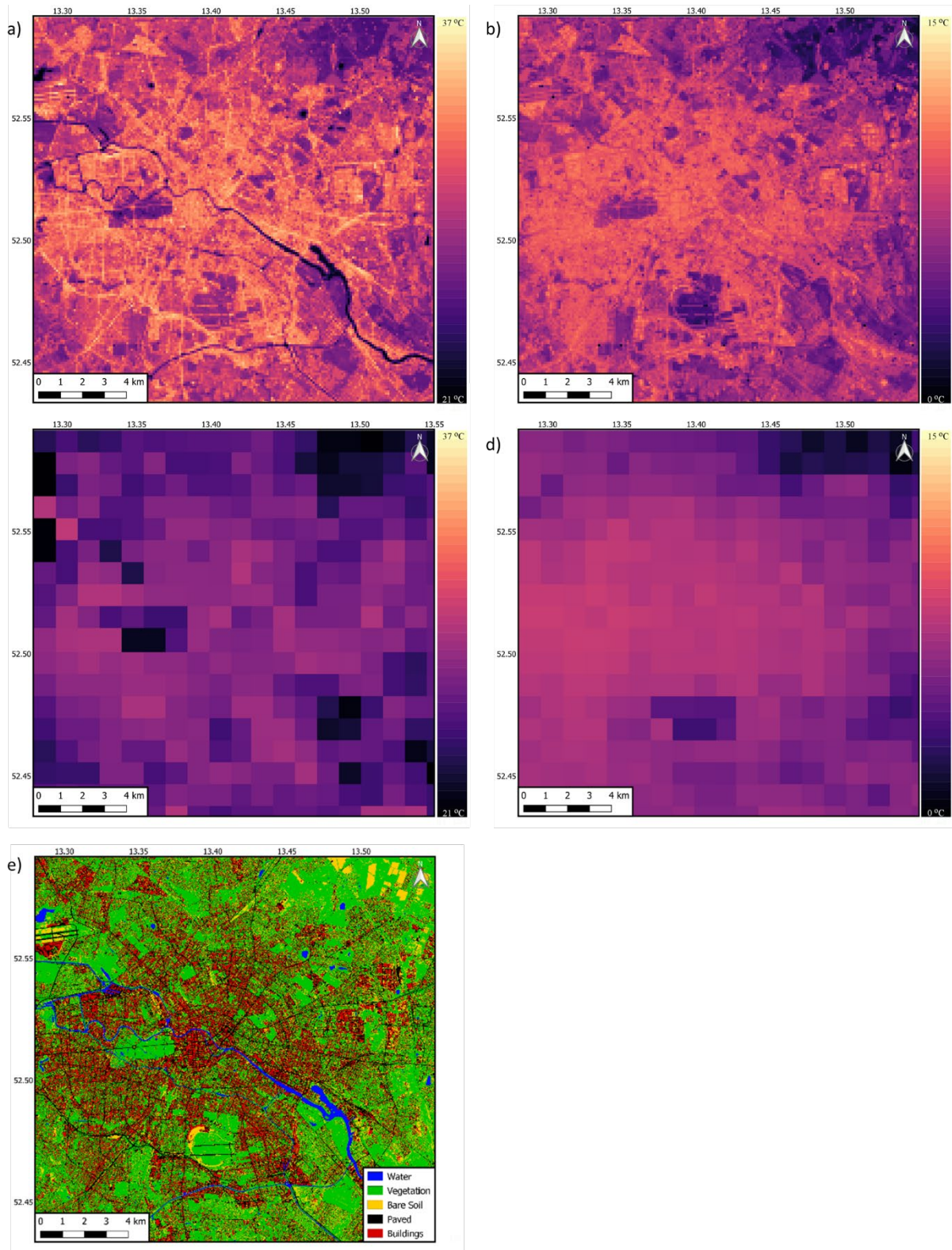
Figure 3. Sample products of AP01: a) Daytime (11.26 local time 30/05/2019) and b) Nighttime (22.32 local time 16/04/2019) Land Surface Temperature (LST) map of 100 m spatial resolution for the city of Berlin and b), c) the respective 1 km spatial resolution products. e) The VHR baseline land cover map is shown for reference.

2.2   Sample results for the front-runner cities

The CURE AP01 products are detailed LST maps, which reveal information on the surface temperature of the individual urban surfaces. Figure 3 shows two sample LST product maps for the city of Berlin. The level of detail emerging in the 100 m spatial resolution products (Figure 3a and b) is evident, particularly compared to the 1 km products (Figure 3c and d). In the daytime product (Figure 3a) of May 2019, mid-day (11.26 local time) individual temperatures are observed for different surface covers, i.e. paved surfaces like the road network, the parking lots and airport runaways present higher surface temperatures than urban green spaces, reaching up to 37 $^{\circ}$C.). The nighttime product (Figure 3b) corresponds to mid-April 2019, a couple of hours after the sunset. The slow release of heat in the urban surfaces is evident in this surface temperature map, which remain hot compared to the surroundings after the sunset.

While surface temperature maps like this, can directly provide quantitative information for the impact interventions like the application of cool materials in paved surfaces, which immediately would reduce the surface temperature, in order to have a comprehensive overview of the city's heat load, the combination of all CURE heat related applications in needed.

3 AP02 SURFACE URBAN HEAT ISLAND ASSESSMENT

3.1 Final Input Data & Methodology

Theoretically, the SUHII is defined as the difference in temperature between urban and surrounding rural regions. Traditionally, the quantification of UHII is conducted at two fixed in-situ stations, one in urban and the other in rural regions. Similarly, the remote sensing-based variant, the SUHII, has been derived using selected pixels that are located in the urban and rural regions, respectively. However, it is immediately clear, that single locations or pixels can only reflect part of the SUHI characteristics, especially in cities with multiple UHI centres, and do not necessarily generalize to an entire city. Moreover, the different definitions of "urban" and "rural" regions make the inter-comparison study of SUHII among different cities particularly challenging. To overcome these limitations, the methodology recently presented by Li et al. (2018) is used in CURE. In particular, the intended approach will allow calculating SUHII and its temporal dynamics by exploiting the relationship between land surface temperature (LST) and the percentage impervious surface (PIS), which – according to the literature – proved consistent for cities in biomes dominated by forests and grasslands as in Europe.

3.1.1 Input Data

There are a number of urban imperviousness products provided through the Copernicus program. In particular, AP02 will make use of the CLMS High Resolution Layers of imperviousness density (IMD HRL), which have been published for the years 2006, 2009, 2012, 2015 and 2018. These will serve as the primary data source for the PIS layer. These status layers are available in 20m spatial resolution for the years 2006 to 2015 and 10m spatial resolution for the year 2018.

Figure 4 displays the 2018 IMD HRL for the CURE front-runner cities after pre-processing with the convolution step described in the Methodology section.
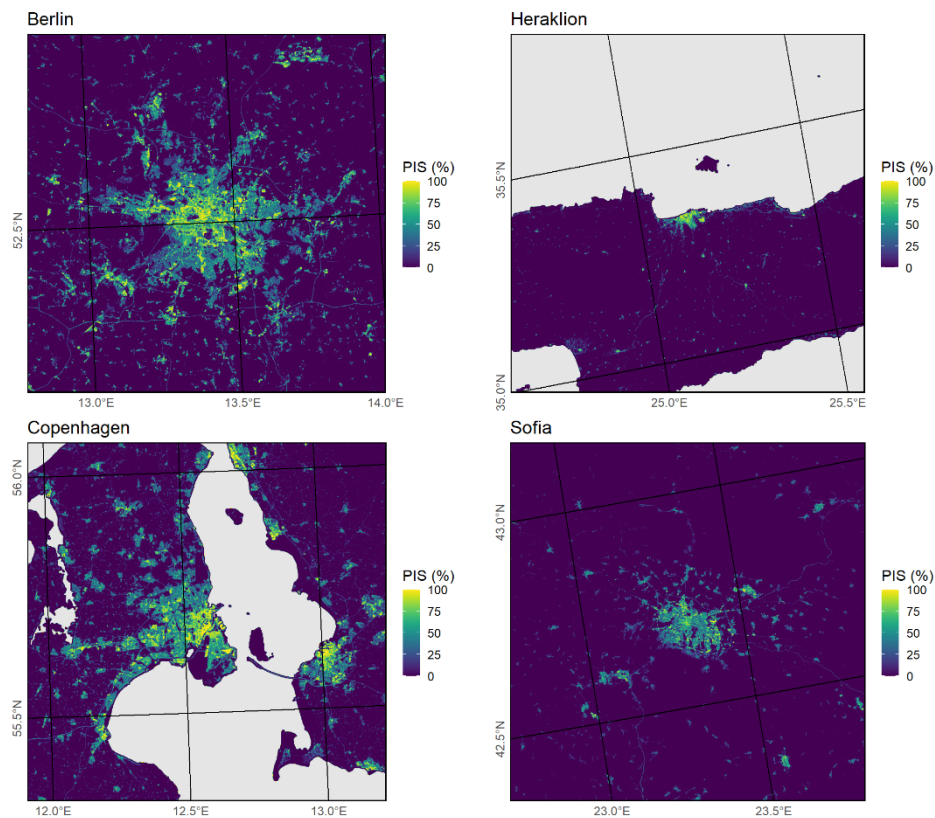
Figure 4. *PIS layer derived from CLMS IMD HRL 2018 for the CURE front-runner cities after convolution with PSF kernel.*

Furthermore, it is anticipated to base the framework in addition also on an improved imperviousness product developed in the processing framework of the World Settlement Footprint (Marconcini et al. 2020), which is based on Copernicus Sentinel-2 data for the year 2019 (which can be extended backwards to 2015) and on Landsat-5/7/8 for the period 1985-2015.

For the LST layer, AP02 relies on land surface temperature data developed and processed in AP01, thus making use of both CLMS and CAMS data sources. For initial development and pre-Sentinel era analyses, AP02 made use of Landsat 5, Landsat 7 and Landsat 8 derived LST data (Parastatidis et al. 2017).

Figure 5 displays LST composites derived from Landsat 8 TIRS data over the summer months of 2017-2018 for all CURE front-runner as described in the Methodology section.
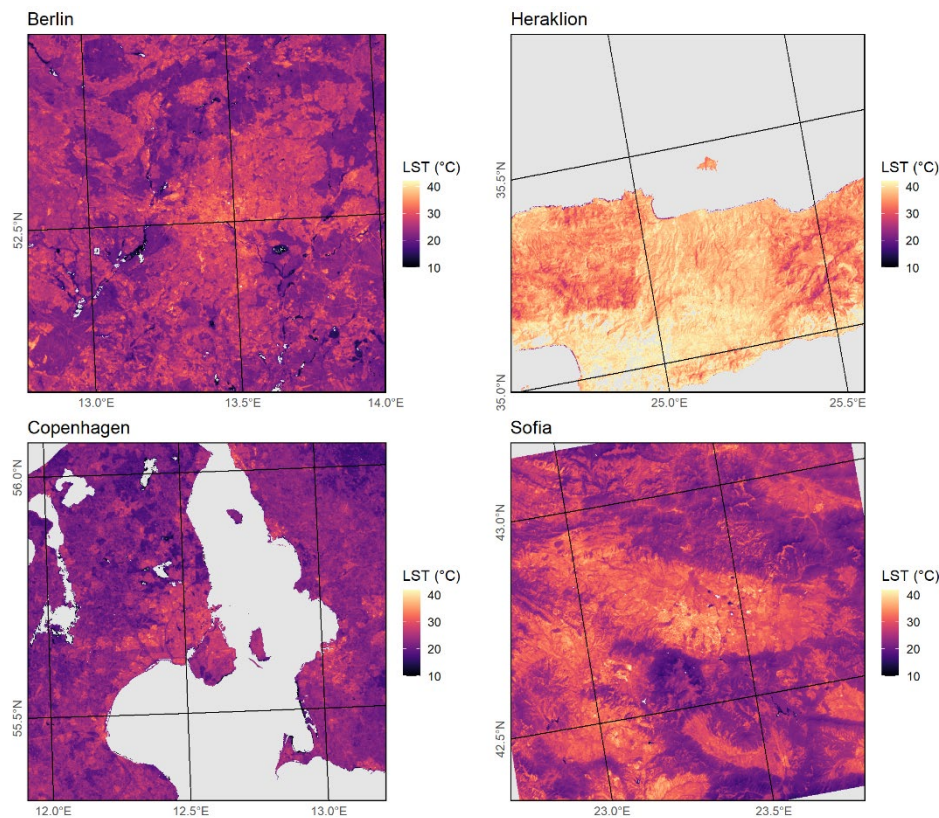
Figure 5. *LST multi-temporal composite layer derived from Landsat 8 TIRS data for the CURE front-runner cities.*

3.1.2   Methodology

Following the state-of-the-art summary given in D1.3, the selected methodology for SUHII derivation is based on performing a regression of the measured LST against the imperviousness degree following the method of Li et al. (2018). The SUHII is then defined as the slope of a linear regression line. While this method avoids having to define "urban" and "rural" pixels explicitly, defining the cutoff distance or condition of which rural surroundings around a city to consider, is still an unsolved challenge and is part of the development analyses within AP02.

Figure 6 summarizes the processing steps needed to implement the AP02 processor. The LST data from AP01 described in the previous section will be provided on a per-scene basis. LST from individual acquisitions is subject to gaps due to cloud-cover, as well as natural variability of temperatures due to weather. Therefore, in order to obtain a robust characterization of the LST properties, the individual acquisitions are composited by calculating the median over a given timeframe, to be determined by a dedicated sensitivity analysis. In our preliminary experiments with the Landsat-based LST, to take into consideration the months May to October for two consecutive years proved to be a promising choice. However, this is mostly driven by the 16-day Landsat acquisition frequency in contrast to the daily information expected to be derived based on Sentinel-3 imagery by AP01.

Next, the imperviousness layer from the CLMS IMD HRLs is processed to match the LST data. Since the spatial resolution of the thermal Landsat bands is 100m plus adjacency effects due to the sensor's point spread function (PSF), the high-resolution PIS data is convolved with a Gaussian kernel of width σ = 50m to correspond to the LST measurement.

Subsequently, pixel values are sampled from both the IMD and LST composite using a regular sampling grid and discarding no-data, as well as water pixels. Using these samples, we fit a robust linear model, in order to avoid undue influence of extreme values, as:

$$LST = \beta_0 + \beta_1 \cdot PIS$$

where finally β_1 defines the SUHII.
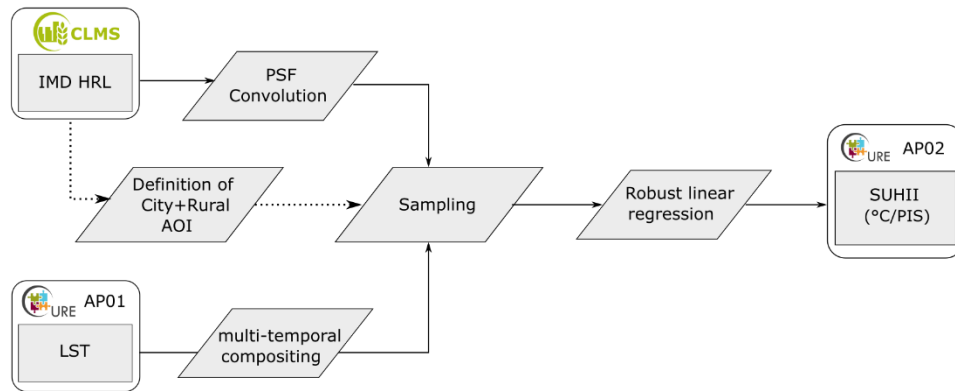
Figure 6. *Simplified flowchart of the AP02 SUHII processor.*

Initial results have been produced for all four CURE front-runner cities with the CLMS IMD HRL 2018 and Landsat 8 LST data, which were calibrated using an emissivity based on Landsat NDVI as well as atmospheric water vapour content derived from the NCEP/NCAR Reanalysis Project as described in Parastatidis (2017).

Figure 7 displays the resulting SUHII index values with their corresponding confidence intervals over variably sized buffers around the city centres. This clearly highlights the sensitivity of the SUHII to the definition of the urban extent, yet also provides an opportunity to define the cut-off in a data-driven manner, for example as the point of initial saturation.
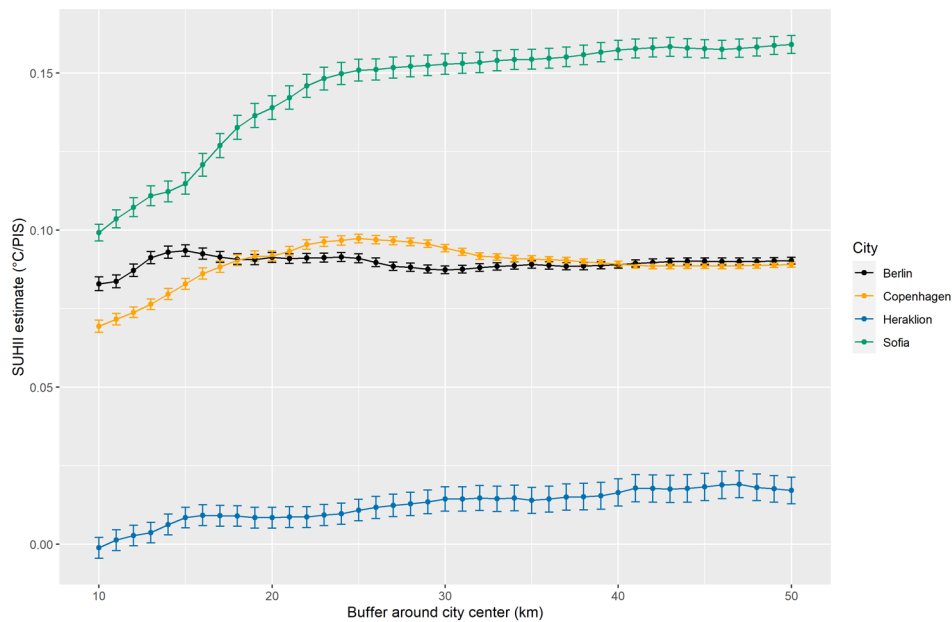
Figure 7. *Estimates of SUHII vary depending on the definition of the city and encompassing rural extent. It is yet to be determined how to delineate the city body.*

3.2 Sample results for the front-runner and follower cities

SUHII temporal profiles were calculated for all frontrunner cities. They clearly distinguish between different thermal properties, as well as their annual dynamics. Results presented below were derived for bi-monthly LST data of the years 2018 and 2019 calculated via CURE AP01. High SUHII values indicate a pronounced heating effect of the city core as opposed to its rural surroundings. Values around zero indicate no effect and negative values indicate an opposite with a cooler city body than the surroundings. Noteworthy in addition to the annual profiles are the diurnal variations, which are complementary in understanding urban thermal properties.
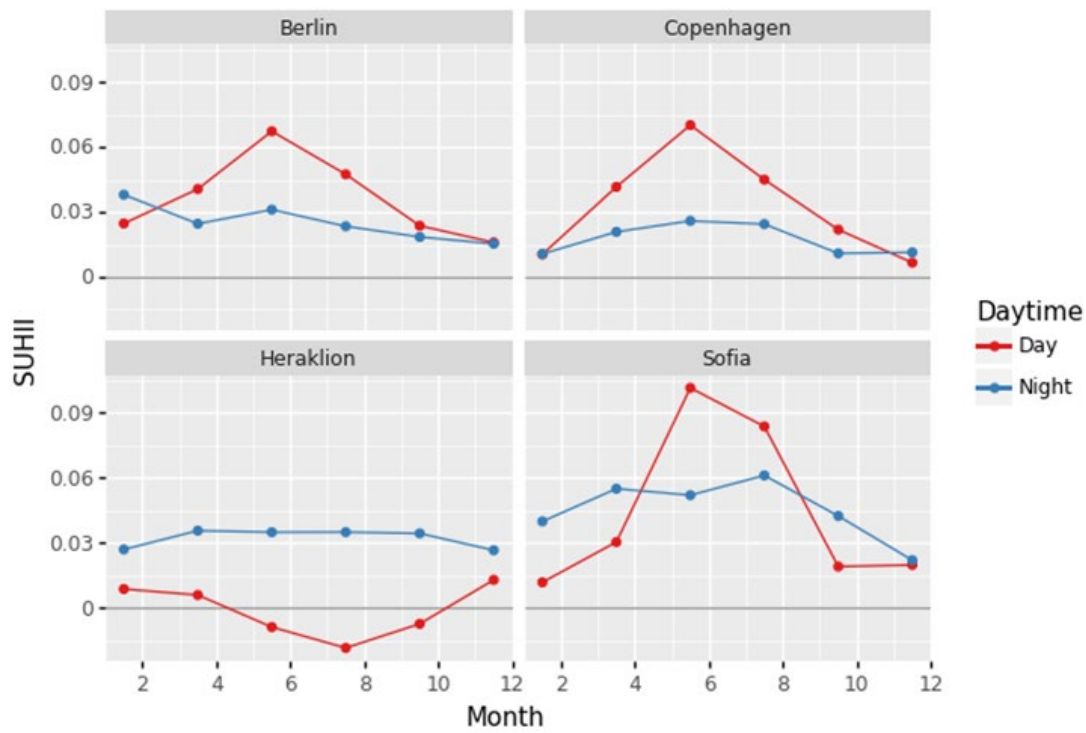
Figure 8. SUHII profiles for all frontrunner cities.

4 AP03 URBAN HEAT EMISSIONS MONITORING

4.1 Final Input Data & Methodology

CURE AP03 is based on the Aerodynamic Resistance Method (ARM) for the estimation of sensible heat flux Q_H at local scale (Voogt and Grimmond, 2000). The ARM was successfully applied in the former URBANFLUXES project (Chrysoulakis et al., 2018) for the calculation of citywide sensible and latent heat flux in a spatial resolution of 100 m x 100 m. In CURE, the ARM implementation described in Feigenwinter et al. (2018) is further developed and adapted to suit the requirements of CURE end users, i.e. city planners and stakeholders. The model results are evaluated with in-situ turbulent sensible heat fluxes measured by the Eddy Covariance (EC) method at urban flux towers (Feigenwinter et al., 2012).

4.1.1 Input data

In a first step, AP03 will rely mainly on local (non-Copernicus) data to produce a first implementation of the application. In a second step, the local input data is replaced by Copernicus data, where possible.

- Digital Object Model (DOM): A high resolution (1 m x 1 m) model of buildings and trees is the essential base for calculation of roughness parameters and aerodynamic resistances (see Section 4.2.2).
- Land Surface Temperature (LST): For the LST layer, AP03 relies on land surface temperature data developed and processed in AP01
- Meteorological data: Air temperature, humidity, wind velocity, wind direction, radiation from in-situ measurements
- Turbulent fluxes for evaluation: in-situ measurements from urban flux towers equipped with Eddy Covariance systems

Table 3 provides an overview of the datasets used in AP03.

Table 3. Input data for AP03 (local and Copernicus).

Data	Local	Copernicus service
DOM	Available in high resolution for front-runner city Heraklion and follower-city Basel (buildings and trees)	CLMS building heights CLMS street tree layer
LST	LST derived from upwelling longwave radiation measurements for evaluation of AP01 LST product	AP01 LST product
Meteorological data	In-situ measurement network	C3S ERA5 Reanalysis data
Turbulent sensible heat flux Q_H	In-situ EC flux tower	

4.1.2 Methodology

The estimation of sensible heat flux with remote sensing data is based on the bulk transfer approach (Yang et al., 2019), where the surface temperature is derived from satellite data. An implementation of the bulk transfer method is ARM (Voogt and Grimmond, 2000), which is used in several microscale urban climate models.

ARM uses the Monin-Obukhov similarity theory (MOST) (e.g. Foken, 2006) as the theoretical basis to estimate momentum and scalar fluxes in the atmospheric surface layer. MOST is commonly used in meteorological numerical modeling systems. In the MOST framework, roughness lengths for momentum and heat (z_{0m} and z_{0h}, respectively) are the key parameters identifying the aerodynamic features of underlying surfaces (Kanda et al., 2007).

The ARM is a common approach for modelling surface fluxes. Q_H is basically calculated as

$$Q_H = c_p \rho \frac{T_0 - T_A}{r_H} \qquad (4.1)$$

where c_p is the heat capacity of the air (J kg^{-1} K^{-1}), ρ is the air density (kg m^{-3}), T_0 is the surface temperature (K), T_{air} is the air temperature (K) and r_H is the bulk aerodynamic resistance for heat (s m^{-1}) of the complete 3D urban surface (Crawford et al., 2018). T_0 is replaced with the satellite-derived LST product from AP01. Using the radiative surface temperature instead of T_0 requires the completion of r_H with a radiometric excess resistance (Voogt and Grimmond, 2000).

In detail, the aerodynamic resistance for heat r_H will be calculated with

$$r_H = \frac{1}{u_* k} \left[ln\left(\frac{z - z_d}{z_{0m}}\right) - \psi_h\left(\frac{z - z_d}{L}\right) + ln\left(\frac{z_{0m}}{z_{0h}}\right) \right] \quad (4.2)$$

$$u_* = U k \left[ln\left(\frac{z - z_d}{z_{0m}}\right) - \psi_m\left(\frac{z - z_d}{L}\right) - \psi_m\left(\frac{z_{0m}}{L}\right) \right]^{-1} \quad (4.3)$$

where u_* is the friction velocity, k is the von Karman constant (0.4), z refers to a reference height (usually the height of wind measurements), z_d is the zero-plane displacement height, L is the Monin-Obukhov length, z_{0m} and z_{0h} are the roughness lengths and $\psi_{m,h}$ are the stability functions for momentum and heat, respectively. Equation (4.3) can be used to estimate u_* from wind velocity U, if no direct measurements of the friction velocity is available. z_{0h} values are usually reported as the dimensionless number $k\beta^{-1}$, defined as

$$k\beta^{-1} = ln\left(\frac{z_{0m}}{z_{0h}}\right) \qquad (4.4)$$

$k\beta^{-1}$ is a key parameter in the ARM. In literature, reported values for $k\beta^{-1}$ show a large variability, even for similar types of surfaces. Lowest values of around 2 correspond to homogeneous vegetative surfaces (Brutsaert 1982), but also to flat semi-arid areas (Koshiek et al. 1993). Higher values are reported for heterogeneous surfaces and urban land use classes, e.g. with values around 20-27 for a light industrial site as reported by Voogt and Grimmond (2000). Kato and Yamaguchi (2007) list values for $k\beta^{-1}$ of 7 (industrial, urban, forest), 4.6

(grassland) and 3.9 (lawn, bare soil). Several studies used Eddy Covariance (EC) and/or scintillometry measurements to determine $k\beta^{-1}$ in the footprint of their measured fluxes. z_{0h} may also be calculated from the roughness Reynold's number (e.g. Kanda et al., 2007)

$$z_{0h} = z_{0m}[7.4\,exp(-\alpha Re_*^{0.25})] \qquad (4.5)$$

where α = 1.29 and $Re_* = z_{0m}u_*/\nu$ is the roughness Reynolds number with a kinematic molecular viscosity ν of 1.461×10^{-5} ms^{-1}. This z_{0h} value is used in Equation (4.4) for the calculation of aerodynamic resistance r_H.

The Urban Multi-scale Environmental Predictor (UMEP, Lindberg et al., 2018) provides the framework for calculation of the spatial distribution of roughness parameters and derived aerodynamical resistances needed for the calculation of Q_H in Equation (4.1) with the input data listed in Table 3. The zero-plane displacement height z_d is calculated after Kanda et al. (2013), using additional morphological parameters like the plan area index λ_p and the frontal area index λ_f.
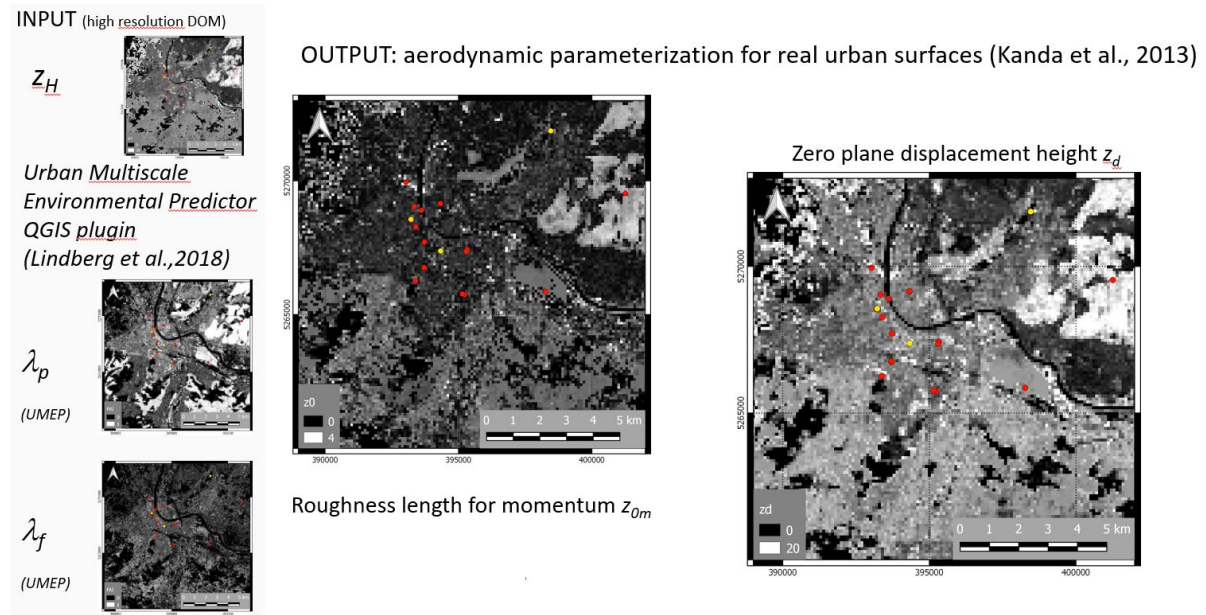
Figure 9. UMEP input (left) and output of roughness parameters for calculation of aerodynamic resistance.

INPUT

r_H

T_{air}

LST

OUTPUT: sensible heat flux Q_H

$$Q_H = \rho c_p \frac{LST - T_{air}}{r_H}$$

BASEL Q_H for 30 AUG 2015
11:00 UTC + 1
Landsat 8 overpass
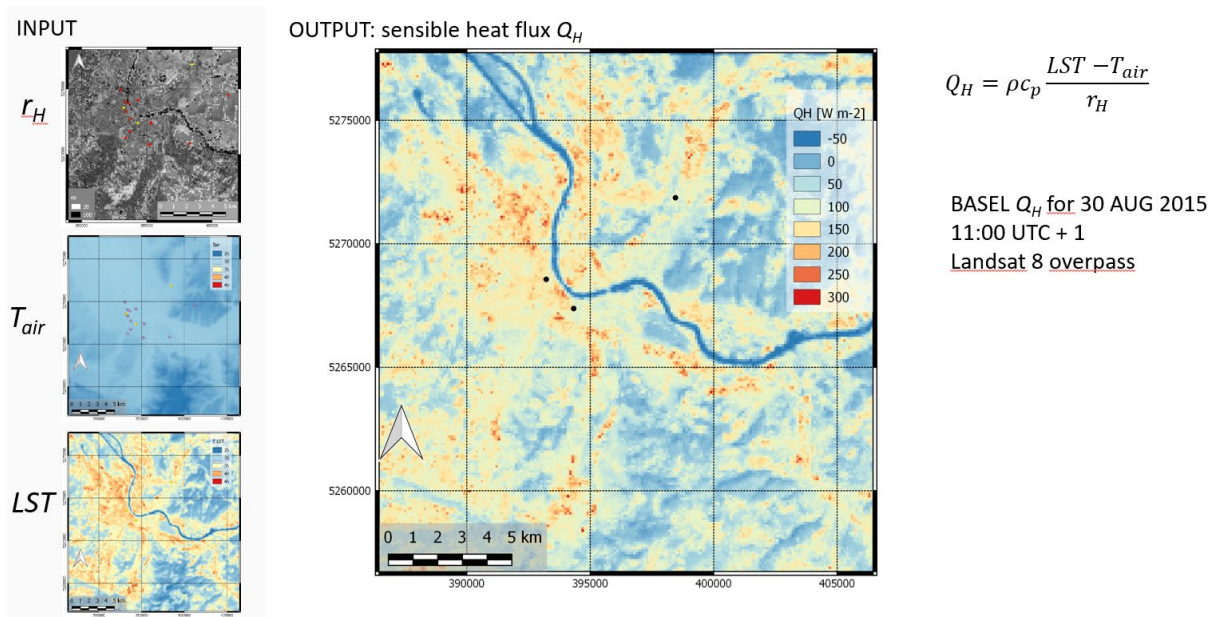
Figure 10. *Final calculation of spatial distribution of Q_H. Example from URBANFLUXES presented at JURSE, 6-8 MAR 2017, Dubai.*

4.1.3   Uncertainty, limitations and validation

A comparison of measured sensible heat fluxes with weighted modelled fluxes in the footprint of the flux towers in the frame of the URBANFLUXES project showed that measured Q_H were generally higher for all case study cities. Several reasons may lead to these differences, as discussed in Feigenwinter et al. (2018): The uncertainty inherent to EC measurements for Q_H is in the range of 10% (25% for other trace gases), the representativeness of flux tower measurements in urban environments is reduced compared to rural areas due to the heterogeneity of urban neighbourhoods and there are large (inherent) variations in EC measurements between the averaging intervals which additionally increase the uncertainty for the time of the satellite overpass. There are also known drawbacks of the ARM method: input parameters (T_{air}, friction/wind velocity) have to be spatially derived from in-situ measurements (flux towers and/or sensor networks) and may differ from "true" values in certain areas during satellite overpass; further large uncertainties exist in the calculation of the aerodynamic resistance including $k\beta^{-1}$. Figure 11 shows the deviations between measured and modelled values of QH for two flux tower sites (adapted from the URBANFLUXES project).
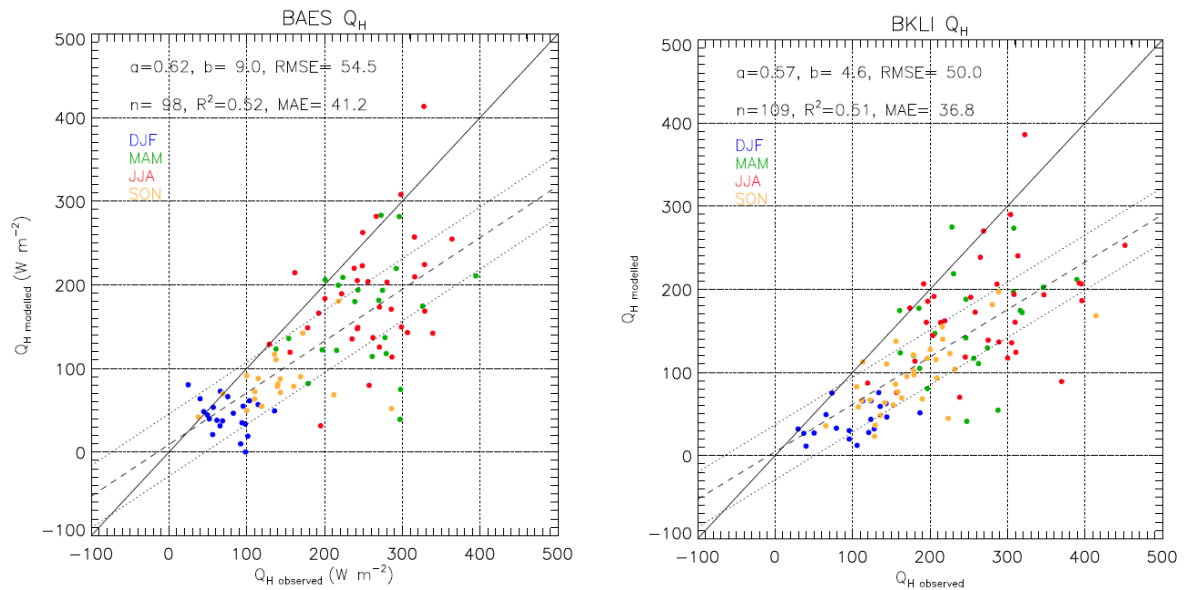
Figure 11. *Differences between measured and modelled Q_H for two flux tower sites in Basel, Switzerland.*

Since the deviations are systematic, we hypothesize that the differences are related to the anthropogenic heat flux, which may not be considered in the ARM method but is measured by the EC system.

4.2   Sample results for the front-runner and follower cities

Figure 12 shows a sample result of AP03 for front-runner city Heraklion. A daytime and a nighttime map of sensible heat flux Q_H in W m^{-2} are displayed.
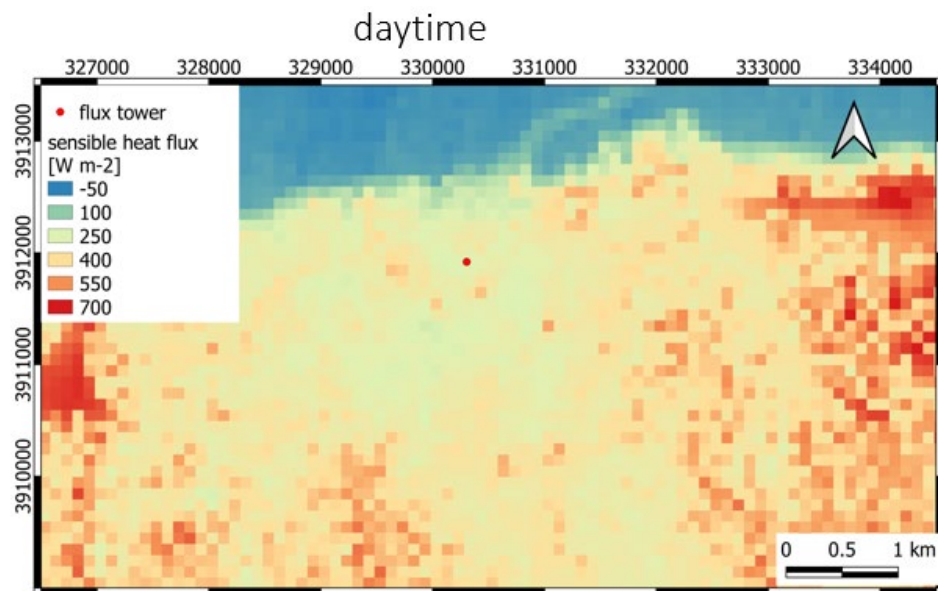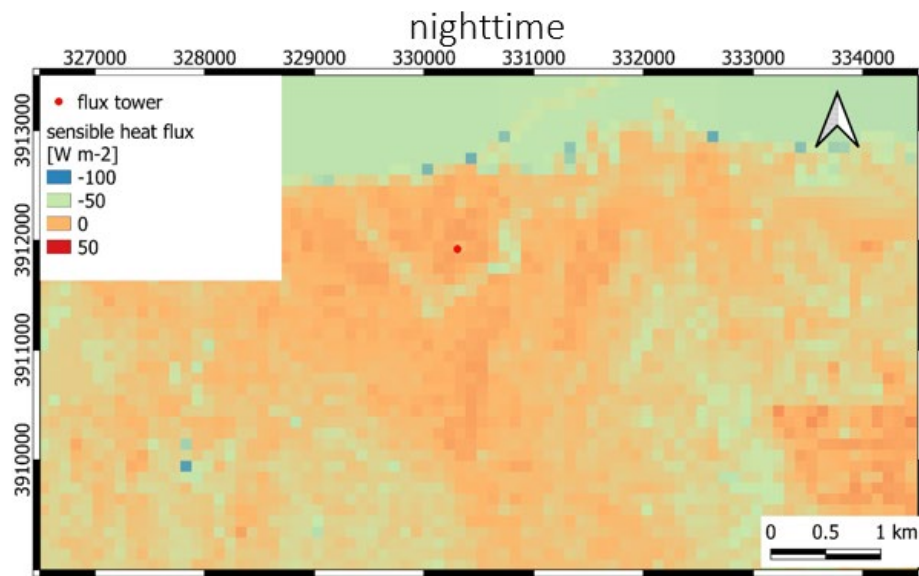
Figure 12. *Example for AP03 product for front-runner city HERAKLION: Spatial distribution of sensible heat flux Q_H for daytime (top) and nighttime (bottom).*

5 AP04 URBAN CO$_2$ EMISSIONS MONITORING

5.1 Final Input Data & Methodology

CURE AP04 will be developed for retrieving CO$_2$ emissions within city boundaries in neighborhood scale, combining local scale CO$_2$ flux measurements by Eddy Covariance (Stagakis et al., 2019) with surface parameterization based on source strenghts proxies derived from local data, Sentinel-2, VHR satellite data and CLMS products through the most up-to-date turbulent flux source area model (Kljun et al. 2015). The individual processes contributing to the total CO$_2$ emissions will be statistically modelled and scaled up according to the associated source strength proxies.

5.1.1 Input data

AP04 is based on a mix of local data, products from ESA- and Copernicus data sources and pure Copernicus services. Key data sets are:

- Road network and traffic data
- High resolution digital object model (DOM) of buildings
- Population density
- Seasonal NDVI
- Turbulent fluxes of CO$_2$: in-situ measurements from urban flux towers equipped with Eddy Covariance systems. The core data set of AP04 to be used for assigning the contributions from the four basic sectors to the total flux.
- Meteorological data: Air temperature, humidity, wind velocity, wind direction, radiation from in-situ measurements. Needed for flux footprint calculation.
- Digital Object Model (DOM): A high resolution (1 m x 1 m) model of buildings and trees is the essential base for calculation of sectorial roughness parameters as input for the flux footprint model.

Table 4 provides an overview of the datasets used in AP04.

Table 4. Input data for AP04 (local and Copernicus).

Data	Local	Copernicus service
Land Use/Land Cover map	Available in high resolution for front-runner city Heraklion and follower-city Basel based on VHR satellite data	CLMS urban atlas
DOM	Available in high resolution for front-runner city Heraklion and follower-city Basel (buildings and trees)	CLMS building heights CLMS street tree layer
Road network and traffic data	TomTom traffic statistics product, traffic counts and road network	
Population density Seasonal NDVI		URBAN ATLAS 2012 Sentinel-2
Meteorological data	In-situ measurement network	C3S ERA5 Reanalysis data
Turbulent CO_2 flux F_C	In-situ EC flux tower	
CO_2 concentration and fluxes		CAMS Flux inversion reanalysis of global CO_2
Energy/Fossil fuel consumption	From city authorities, where available	

5.1.1.1   LULC and road network

The concept of LULC map from the former H2020 URBANFLUXES project (Chrysoulakis et al., 2018) is the base for LULC classification used in AP04. This classification is extended with the road network from OSM, because traffic is one of the main sources of CO_2 emissions in general and in the front-runner city Heraklion in detail. Figure 13 shows the LULC classification with road network.

Figure 13. *LULC map of the HERAKLION city center extended with OSM network.*

Because there are no traffic data available for the front-runner city Heraklion a trial set of the traffic statistics from the TomTom Historical Traffic Services (https://support.move.tomtom.com/ts-introduction/) is used. Figure 13 shows an example of the capabilities of this data set. For each street node, "hits", i.e. the number of vehicles, are available in hourly resolution. Since the road is in the area of the main contribution to the total flux (red and yellow colors of the flux footprint), this dataset is considered as an adequate substitute for automatic permanent traffic count locations.

5.1.1.2 Eddy Covariance flux tower data

CO_2 fluxes from the Heraklion flux tower measured by the Eddy Covariance (EC) method are available from November 2016 to date, with a large gap due to technical problems from November 2018 to July 2019. A detailed description of the EC method in general can be found in Aubinet et al. (2012), while Feigenwinter et al. (2012) refers to the specific issues of EC measurements in urban environments. EC raw data (20 Hz) were processed with the EddyPro® Software version 7 from LI-COR Biosciences resulting in half hourly CO_2 fluxes and numerous diagnostic parameters. A very useful diagnostic parameter is the quality flag calculated after the method of Foken et al. (2004) which provides the flag "0" for high quality fluxes, "1" for intermediate quality fluxes and "2" for poor quality fluxes. This system is suitable for selecting flux results complying with international practices.
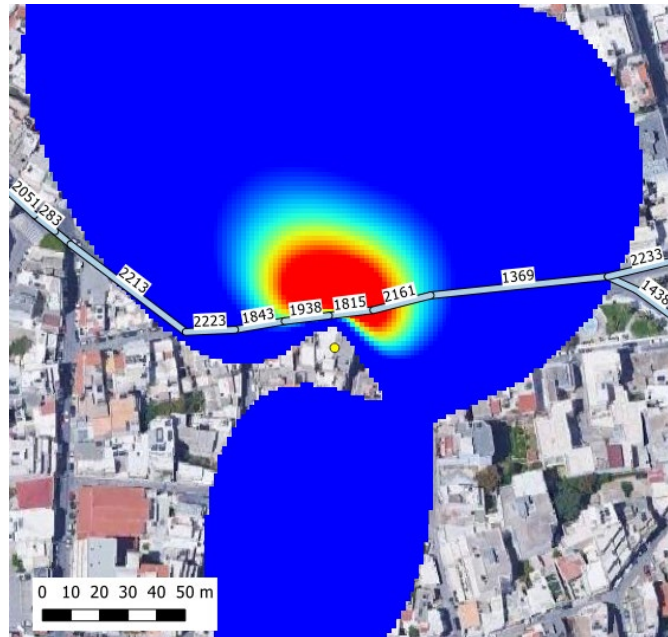
Figure 14. TomTom road nodes (numbers) with hourly vehicle counts in the footprint of the HERAKLION flux tower (yellow dot). Colors refer to relative contributions to the total flux from high (yellow) to low (blue).

Figure 15 exemplarily shows the data availability and the data quality of half hourly Heraklion CO_2 fluxes for the months JUL/AUG/SEP 2018. For all further processing only fluxes with flags 0 and 1 are used.
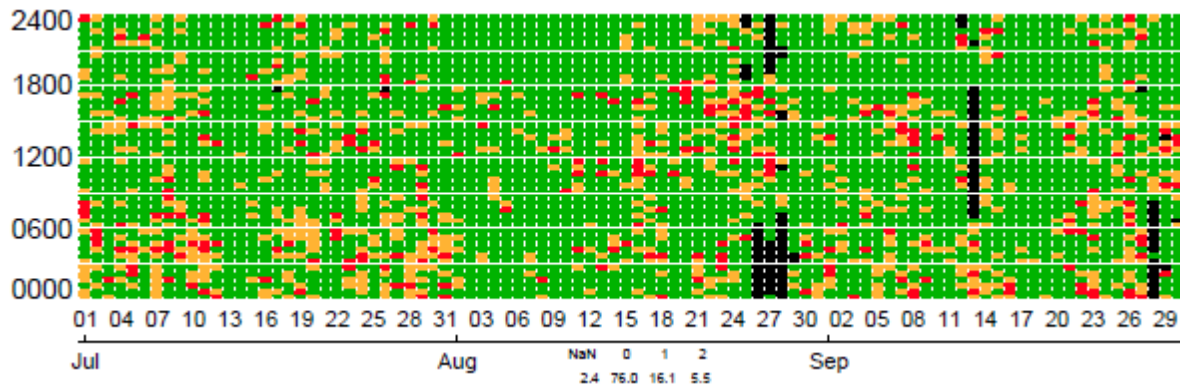
Figure 15. Data availability for and data quality of HERAKLION CO_2 fluxes for JUL/AUG/SEP. Green, orange and red colors refer to quality flags 0,1,2 (high, intermediate, poor), respectively. Black colors refer to "no data".

5.1.2 Methodology

The approach for estimating within urban boundaries' CO_2 emissions (excluding industrial processes) is based on statistical modelling of four basic source and sink processes in the urban environment, according to the following equation:

$$CO_2(x,y) = c_{traffic} * SS_{traffic} + c_{build} * SS_{build} + c_{popdense} * SS_{popdense} + c_{veg} * SS_{veg} \quad (4.5)$$

where subscripts $traffic$, $build$, $popdense$ and veg represent the contributions to the total CO_2 emission at point x,y from the transport sector, building sector, human metabolism and vegetation, respectively. SS stands for source strengths. Table 5 provides an overview of the proxy datasets used in eq (4.5).

Table 5. List of proxy data sets for emission sectors

Emission Sector	Data	Source
Transport	Vehicle counts	Local, TomTom statistics
Buildings	Building volume	Local, Copernicus Urban Atlas
Human metabolism	Population density	Copernicus Urban Atlas
Vegetation	Tree volume, NDVI	Local, Copernicus Sentinel

Coefficients c in eq (4.5) are determined in an iterative way by comparing with local scale contributions from the respective emission sector in the source area of the CO_2 flux measurements by Eddy Covariance. The turbulent flux source area model (Kljun et al., 2015) is applied and parameterized based on detailed urban morphology indicators. Air temperature derived heating degree days will be auxiliary parameters for emissions from the building sector where relevant. Emission estimates from human metabolism are based on spatially aggregated population statistics (Christen et al., 2011). Since the vegetation fraction in the footprint of the Heraklion flux tower is very small, the biogenic contribution in the area of interest is modelled by an empirical approach based on seasonal NDVI (Del Grosso et al., 2018). Individual emission sector contributions are scaled up to city-wide maps and synthesized to net CO_2 emission products. Figure 16 shows the general concept of AP04 methodology.
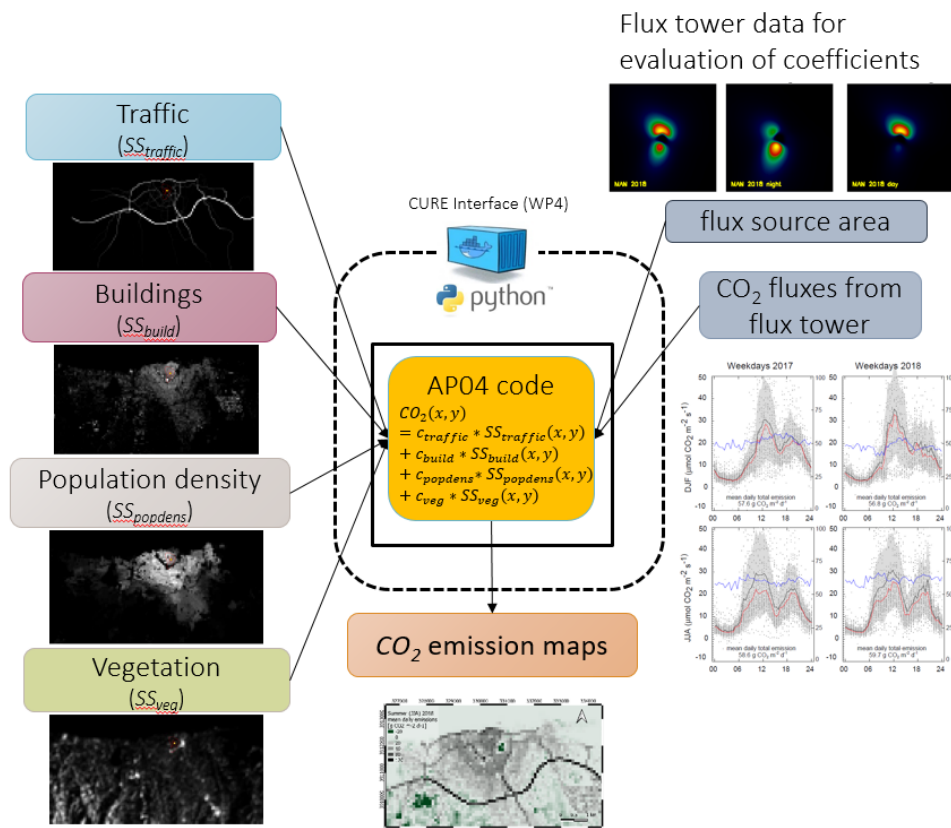
Figure 16. *General concept scheme of AP04 methodology*

5.1.2.1 Mean seasonal diurnal and hourly fluxes and footprint calculation

For the final AP04 product we propose an approach based on seasonal mean diurnal fluxes and the corresponding averaged footprints, i.e. the footprint climatology. Figure 17 shows the mean diurnal course of CO_2 fluxes for the meteorological seasons winter (DJF), spring (MAM), summer (JJA) and autumn (SON) for the years 2017 to 2020. The bi-modal shape indicates that traffic (rush hours) are the main driver of CO_2 emissions in the footprint of the HERAKLION flux tower. It is therefore important to have detailed information about traffic in order to correlate the CO_2 fluxes with traffic frequencies. From Figure 17 it is also obvious, that heating in the winter plays a minor role since no increase of the mean daily total emission is observed. On the other hand, also no significant signal from vegetation is observed, because this would exhibit lower emissions due to photosynthesis in the vegetation period. Mean half hourly footprints are calculated by averaging the available footprints for each half hour in a similar way (not shown). The mean diurnal courses of CO_2 fluxes and the average footprints were used for further processing as described in the previous section.
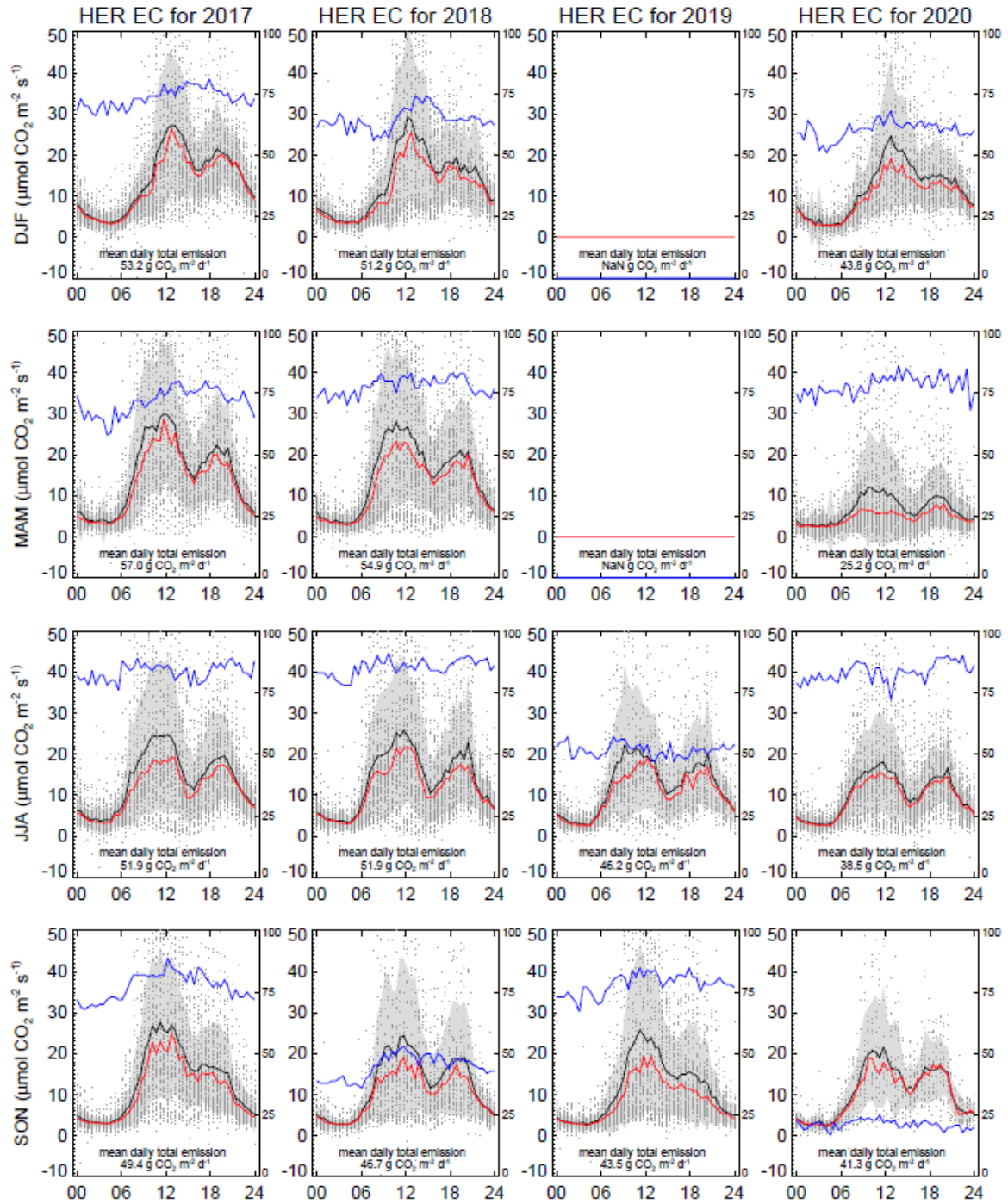
Figure 17. Mean diurnal course of F_C for all seasons (top to bottom) and years 2017 to 2020 (left to right) with mean daily total emissions. Arithmetic mean (black), median (red), standard deviation (gray shaded) and single half hourly values (dots). The blue curve refers to the number of measurements used for averaging and scales with the right y-axis (max. number of measurements is around 90 days for a season).

5.2 Sample results for the front-runner and follower cities

Figure 18 shows a sample result of AP04 for front-runner city Heraklion. Mean daily CO_2 emissions in g CO_2 m^{-2} d^{-1} are displayed for summer season (JJA) 2018.
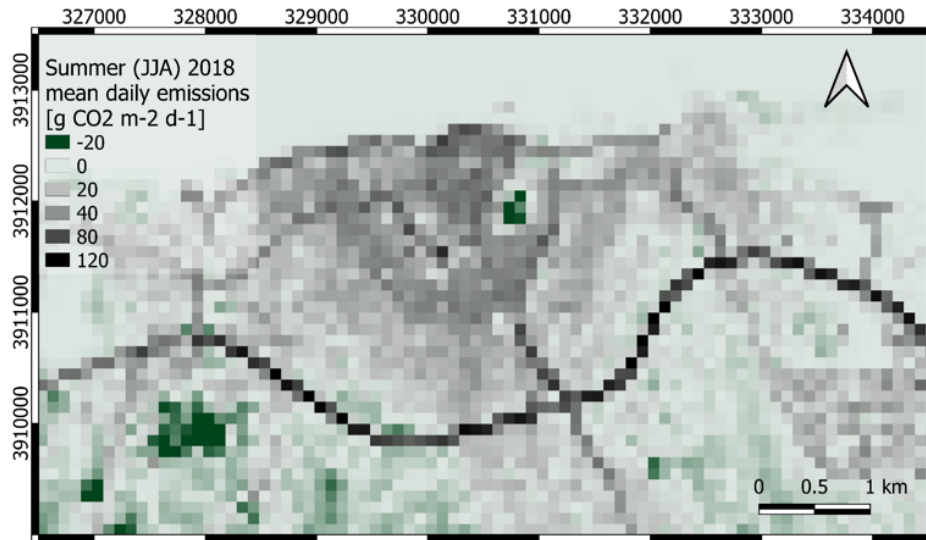
Figure 18. Example for AP04 product for front-runner city HERAKLION: Spatial distribution of mean daily CO_2 emissions during summer season 2018 (months June, July and August). Highest emissions are linked to traffic (road network) and densely built-up areas (buildings, human metabolism). Vegetated areas act as a sink for CO_2 during the vegetation period.

6 AP05 Urban Flood Risk

6.1 Final Input Data & Methodology

The method is based on **combination of information about flood risk** depending on local terrain and hydrological characteristics and information about **spatial pattern**, **internal structure and temporal evolution of urban areas** and also about **distribution of population** in those areas.

The app adopts a **"scenario modelling" approach** – i.e. scenarios representing different intensities of flood events are modelled and compared as well as (potential) damage on urban assets and people in the cities caused by these events. This is done based on reference information about flood events in the past and simulations of estimated intensities of expected floods in the future also in relation with different potential climate change scenarios.

6.1.1 Data inputs

The main type of input data for this app is represented by Copernicus Core Services datasets. This secures high replicability (scalability) potential of the service. The modelling method is using the EU-DEM and EU-Hydro River Network database as main data inputs. Additionally, other Copernicus datasets can be used to improve the estimation of flood event intensity as well as of expected frequency of such events in the future.

Table 6. Input data for AP05 Urban Flood Risk

CCS	Dataset	Information on
CLMS	EU-DEM	Terrain characteristics/geomorphology
CLMS	European Image Mosaic - High Resolution	Reference information about land surface characteristics in very high resolution
CLMS	Urban Atlas	Distribution, typology and change of the urban land use units
CLMS	EU-Hydro - River Network Database	River network
C3S	E-OBS daily gridded meteorological data for Europe from 1950 to present derived from in-situ observations	Reference information about extreme rainfall events in the past
EMS	Flash flood indicators	Hydrological predictions/scenarios
EMS	Real-time river discharge forecasts	Hydrological predictions/scenarios
EMS	River discharge thresholds	Hydrological predictions/scenarios
EMS	Flood forecasts	Hydrological predictions/scenarios
EMS	River discharge reforecasts	Hydrological predictions/scenarios

These datasets are supplemented by the Copernicus Urban Atlas layer and the World Surface Footprint Evolution (WSF-E) layer in order to obtain detailed information about the structure and development of urban land units .

These datasets are integrated with local city information, or replaced by more precise local data where available and requested by the user. This may include following types of local city data/information:

- Detailed river geometry in vector format
- Detailed terrain model (DTM)/ Digital Surface Model (DSM) e.g. 0,4m DSM/DTM
- Local meteo and hydrological data (river network, runoff, discharge data, sea level)
- Reference data (information) on previous flood events – frequency, extent, inundation depth, incl. corresponding intensity of precipitation, damage on buildings, infrastructure, agricultural land etc.
- Geomorphology/Geology/Infiltration properties of local terrain/landscape
- City plans/urban planning maps - location of buildings, infrastructure, flood-vulnerable units etc.

Also, the local city dataset about the flood events in the past are used as reference information to evaluate the quality of modelling results or to calibrate these results.

6.1.2   Methodology

6.1.2.1   Information about flood hazard

First part of the method is dedicated to obtaining information about flood itself. Information about flood hazard is achieved by combination of various means:

- reference information about flood inundation extent and frequency from historical EO data or other local sources
- geomorphic analysis using DEM/DSM for estimation of flood susceptibility and modelling inundation extent and depth using runoff and discharge patterns, morphology and land cover.

For the first type of analysis, the historical Earth Observation (EO) data serve as the input, in particular dataset from Copernicus programme (DWH). This not only allows for evaluation of the extent and impact of past flood events, but also the Near Real Time (NRT) imageries from Copernicus service will help to include a service with a "rapid response" character, serving for monitoring and evaluation of potential ongoing flood events.

Second, the geomorphic analysis approach (the HAND - high-above-nearest-drainage approach was applied) leading to quantification of flood susceptibility using in particular the digital surface model in combination with the river network data, and information about basic

hydrological characteristics of that area – in particular quantification of runoff representing different precipitation intensities.

These can be supplemented by more advanced types of analysis will be based on sophisticated hydrologic and hydro-dynamic modelling approaches leading not only to modelling inundation extent and depth using runoff and discharge patterns, morphology and land cover, but also other advanced hydro-dynamic analysis, e.g. to compute water surface profiles for steady and unsteady flow models. For this type of analysis, the already existing hydro-dynamic modelling SWs can be exploited. At this moment, HEC-RAS[1]/GeoHECRAS[2], Telemac 2D[3] and Flo-2D[4] can be used for this purpose.

As a result of this first part of the analysis, raster maps representing flood susceptibility, frequency or flood extent and inundation depth for different flooding scenarios are generated, which can either be used on their own or combined with datasets describing urban areas in the next step, to obtain meaningful information about flood risk exposure of urban units.

The app is able to generate results for different flooding scenarios, corresponding with different intensities of rainfall, which can then be compared by the user. The user can modify this parameter to generate flood masks for his own scenarios.

6.1.2.2   Urban flood risk exposure evaluation and modelling

In this second step, the information about (potential) flood intensity is combined with information about the land use, in particular about distribution, typology and changes of urban areas. Maps of flood susceptibility or frequency and estimations of inundation extent and depth for different flood intensities in the future are integrated with the Copernicus Urban Atlas layer (can be supplemented or replaced by local land use maps if requested by the user) to get information about flood hazard to urban assets. Zonal statistics are applied to evaluate flood risk level for each particular land use block from the Urban Atlas. This is combined with the classification of the Urban Atlas block, to derive information about typology of the endangered urban units (residential, commercial, transportation etc. units). Moreover, data on temporal evolution of urban areas (from Urban Atlas or WSF-Evolution layer) are combined with those about flood risk in order to gather (early-warning) information about new constructions in flood-prone areas.

6.1.2.3   Universal character of the application

The app is implemented in maximally universal and automated manner, maximally exploiting the Copernicus data which are harmonized for all (larger) European cities. Thanks to this, the application is easily replicable for most of the European cities (there could be some specificities

---

[1] https://www.hec.usace.army.mil/software/hec-ras/

[2] https://www.civilgeo.com/products/geo-hec-ras/

[3] http://www.opentelemac.org/index.php/presentation?id=17

[4] https://flo-2d.com/

which may limit replicability potential for some of the European cities, like specific terrain characteristics etc.) Second, the main added value of the application consists of combination of the hydrological modelling (dealing with terrain morphology, river network characteristics, intensity of precipitation) with the (harmonized, for all European cities) information about spatial distribution (incl. typology as by distinguished in Copernicus Urban Atlas) and temporal evolution (UA and WSF-Evolution) of urban units.

General statistics (e.g. area of residential/commercial units endangered by flood risk per city) can be calculated and compared for different cities. However, taking into consideration sensitive character of such information, it should be carefully assessed which information will be presented and how it will be published (the access to such information may be restricted to several users, recruited either from administrations of particular cities for which the modelling is performed, or from European institutions). Same is fact is valid for the AP06 dedicated to urban land movements monitoring.

6.1.2.4   Link between flood risk (AP05) and land subsidence (AP06)
For effective urban planning, the integrated approach is crucial. Therefore, also for the CURE project, it is important to combine information acquired by means of different applications in a meaningful way. Moreover, in case of two applications to be developed by GISAT (AP05 and 06), there can be direct link between these two types of natural hazards. The urban (or sub-urban) land subsidence can occur or intensify as a consequence of previous urban flood. On the other hand, the flood risk to particular areas in the city can increase in time, in case a land subsidence process is present at that spot.

Therefore, we are combining information acquired from the AP05 and 06, to enable the end-users to follow potential link (consequences) between floods and terrain subsidence. This integration can be done in following ways:

- First, for each land use block of Copernicus Urban Atlas layer, information about both subsidence and flood risk exposure is evaluated and presented.
- Second, we plan is still to visualise the results of these two apps in the same interactive web-based map application, so the user can easily follow and evaluate potential links between these two types of hazards.

6.2   Sample results for the front-runner and follower cities
The first result generated by AP05 is a raster map showing a distribution and levels of flood hazard over the AOI. The hazard is estimated using the HAND-index based approach (high above nearest drainage), where the level of hazard depends mostly on distance to nearest drainage and local terrain properties. Example of results for the front runner city of Heraklion is presented in Figure 19 below. The approach is parameterizable so the result can be adjusted depending on expected intensity of rainfall event and resulting flood as well as on specific conditions in local area.
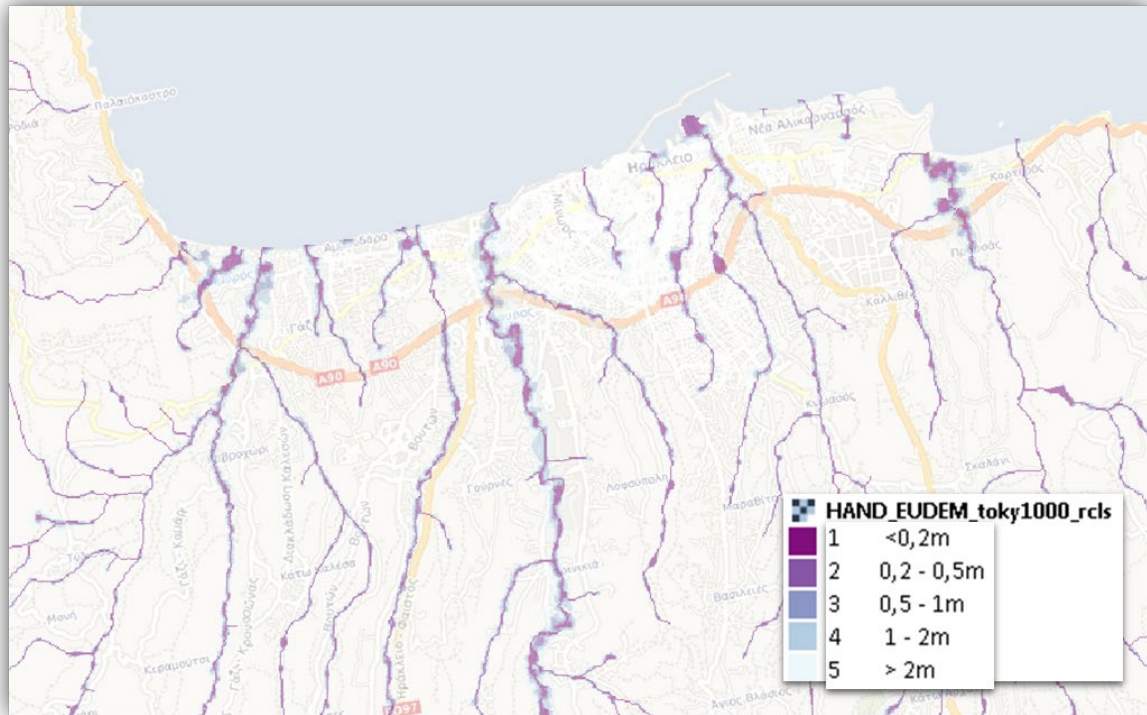
Figure 19. *Example for AP05 basic product for front-runner city Heraklion. Distribution of areas endangered by flood hazard, classified based on level of this hazard from highest to lowest (but still present).*

Based on the above presented basic product of the AP05, the flood hazard is than estimated for urban assets. These may be represented by building blocks or even particular buildings, which are the use cases prepared in the frame of this project, however, they may be represented by any type of object in general, which may be endangered by flood hazard. This hazard to urban assets is evaluated simply by overlaying the above presented raster layer of flood hazard distribution with delineation of the urban assets of interest. Then, the level of flood hazard is quantified for each analytical unit (urban block from Urban Atlas or single building). Examples of such analysis for front-runner city of Heraklion are provided in the figures below.

Legend (top map): Very High, High, Medium, Medium-Low, Low

11100: Continuous Urban fabric (S.L. > 80%)
11210: Discontinuous Dense Urban Fabric (S.L.: 50% - 80%)
11220: Discontinuous Medium Density Urban Fabric (S.L.: 30% - 50.)
11230: Discontinuous Low Density Urban Fabric (S.L.: 10% - 30%)
11240: Discontinuous very low density urban fabric (S.L. < 10%)
11300: Isolated Structures
12100: Industrial, commercial, public, military and private units
12210: Fast transit roads and associated land
12220: Other roads and associated land
12230: Railways and associated land
12300: Port areas
12400: Airports
13100: Mineral extraction and dump sites
13300: Construction sites
13400: Land without current use
14100: Green urban areas
14200: Sports and leisure facilities

☐ Urban Atlas blocks exposed to flood hazard

Figure 20. Evaluation of flood hazard for Urban Atlas functional blocks – example Heraklion city.
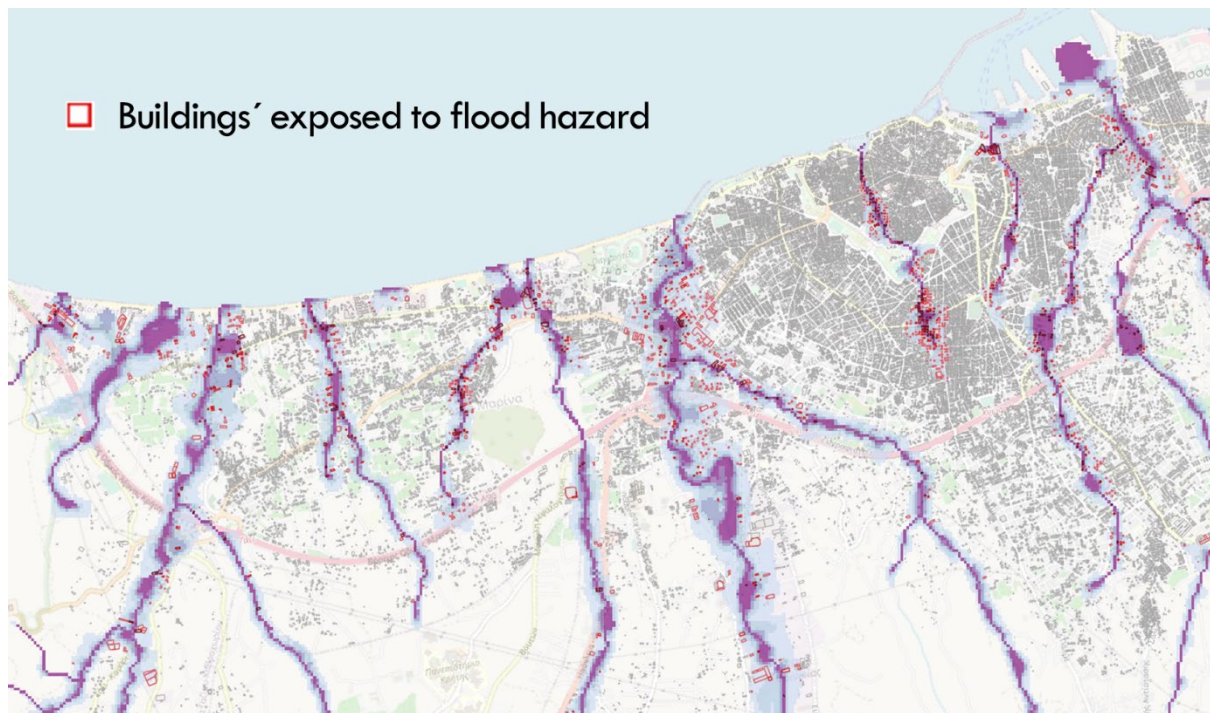
Figure 21. *Evaluation of flood hazard for buildings – example Heraklion city.*

In the next step, we focused on assessment of vulnerability of buildings exposed to flood hazard. There could be many additional criteria helping to evaluate vulnerability of each building exposed to flood hazard, as the age of building, high of building, construction material, type of building use etc. Consideration of all these aspects can help to evaluate the vulnerability of the building exposed to flood hazard. Moreover, an estimation of maximum cost in case of flood event can be made at the city level or in any given sub-city area. Example of such analysis, calculating the numbers, area and volume of buildings endangered by flood hazard in the city in total and by land use type of those buildings (information gathered from Urban Atlas) is illustrated in Figure 22 below. To make more accurate analysis, more detailed and precise local data about buildings´ characteristics would be needed.

Vulnerability analysis – buildings exposed to flood hazard by land use type

- Land use type (from Urban Atlas)
- Height (from local DSM)

Buildings in flood risk	
Total number of buildings	1439
Total area of buildings (m2)	408026
Total volume of buildings (m3)	2854839
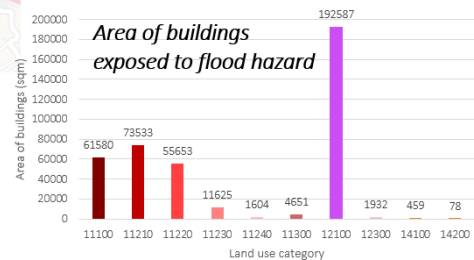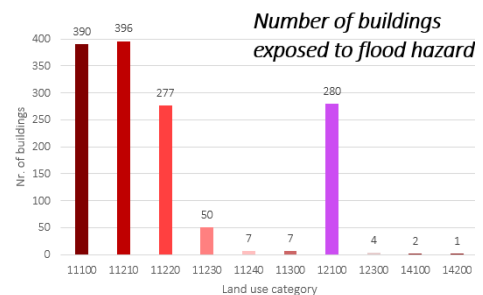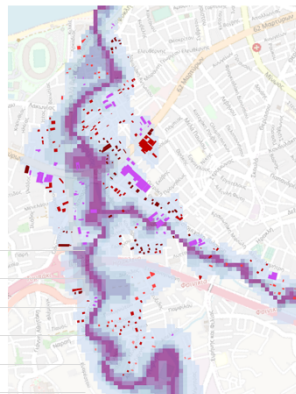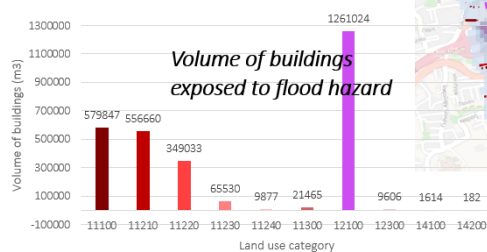
- Estimation of maximum cost in case of damage by flood
- Comparison of different cities (city-level)

Figure 22. *Simple vulnerability analysis – exposure of buildings to flood hazard, by land use type of the building block – example Heraklion city.*

For the Ostrava city-region, representing the follower user of the AP05 Flood risk monitoring service, the same type of analysis has been prepared, including statistical evaluation. Again, the results of this flood hazard assessment were combined with the results of AP06 Subsidence monitoring service for the same area. Figure 23 shows an example of such advanced analysis assessing both types of natural hazards.
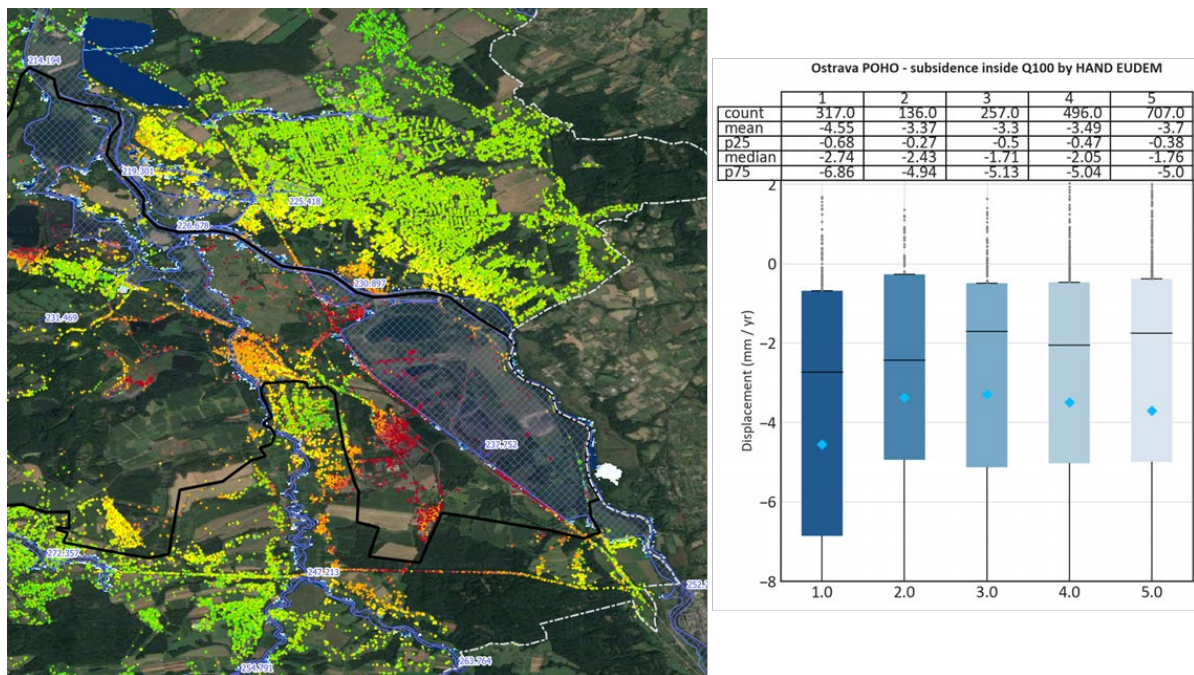
Figure 23. *Example of flood hazard assessment in Ostrava city region combined with information about subsidence hazard (AP06). In this case, the statistical evaluation shows highest level of subsidence in zones which are most endangered by flood hazard.*

In addition to this type of the analysis, dealing with flood hazard estimation by modelling based on Copernicus data (DEM, river network, Urban Atlas etc.), we also made an assessment of potentially visible consequences of a flash flood event which occurred in Heraklion area in October 2020. This assessment was based on visual interpretation and comparison of pre- and post-flood VHR imageries (obtained from DWH). This analysis and its results are described in detail in the D3.8.

Figure 24. *Assessment of consequences of a flash flood event in Heraklion area, based on comparison of pre-post- flood VHR imageries from DWH.*

7 AP06 URBAN SUBSIDENCE, MOVEMENT AND DEFORMATION RISK

7.1 Final Input Data & Methodology

Analysis of spatial patterns of subsidence phenomena brings insights into hazard distribution and its magnitude. Essential is identification of clusters of subsiding measurement points attributed to similar behaviour and outlying points or clusters dissimilar to behaviour of points in surroundings. Furthermore, given complex nature of potential drivers and size of observable objects in the urban environment multi-scale approach will be adopted.

To understand drivers and impacts of land subsidence at city and sub-city level the intensity of terrain deformation hazard derived by means of MT InSAR technology needs to be integrated with additional supportive information. Distribution and chronology of urban evolution (expansion, densification) may affect (among other factors) both spatial and temporal patterns of land subsidence and should be assessed in relation to observed deformation rate. The module consists of series of Python scripts responsible for spatial-temporal analytics and data fusion. Spatial associations are analysed within results from Copernicus EGMS, or from custom MT InSAR processing chain deployed on DIAS infrastructure. Next, the results are integrated with temporal patterns derived from pan-European and global open datasets describing urban structure (Copernicus Urban Atlas) and long-term built-up evolution (DLR's World Settlements Footprint-Evolution). Output from module is represented by standardized analytics providing added value derived from fusion of scalable inputs.

7.1.1 Data inputs

There are two main types of information needed for this app. First, the **information about the subsidence** measured at stable points (permanent scatterers) distributed over the city and city-region needs to be obtained. For this purpose, the **Sentinel-1 SAR imageries** from Copernicus programme are exploited, allowing to identify potential movements at those points and to follow the pattern of their velocity and direction in time. This is allowed by comparison of the situation with a help of dense time-series of Sentinel-1 imageries. This input data source will – in near future – be replaced by the outcomes of the **Copernicus European Ground Motion Service (EMGS)** (https://land.copernicus.eu/pan-european/european-ground-motion-service) , which should become operational next year (2022).

The second type of information needed by the AP06 is the **information about the spatial pattern of urbanized areas and their development in time**. The first – spatial pattern of urbanized areas - is derived in particular from the **Copernicus Urban Atlas**, which brings highly accurate information about internal structure of the cities - distribution of different types of land use in the cities. If not available, this dataset can be replaced by local city planning maps with Urban Atlas-like nomenclature. This could be relevant in particular in case of potential replications of

the service in outside-European cities. The information about the chronology and spatial pattern of the city development is obtained primarily from the **World Settlements Footprint-Evolution** dataset.

7.1.2   Methodology

7.1.2.1   *Measuring terrain movements by means of MT InSAR*

The first step in methodology focuses on **acquisition of information about the subsidence itself.** For this purpose, the **Synthetic Aperture Radar Interferometry (InSAR)** method is exploited. For over than 20 years, this method has been providing ground deformation data at centimeter precision. In the past decade, new ways of processing satellite radar images have been developed using **Persistent Scatterer Interferometry (PSI)** that allow ground movements over wide areas to be detected and monitored with even greater sensitivity. Free and routinely-available SAR data collected by Sentinel-1 sensors' constellation within Copernicus programme represent a unique opportunity for applying these methods on operational level on a global scale (Pepe and Calò 2017). The technique is based on processing of time series of high or very-high resolution satellite SAR imagery which enable detection of up to millimetre displacements. This method has been demonstrated in number of national (Hlavacova et al. 2016; Lazecky et al. 2010) and global EMS related activations and also used for recently awarded state-of-the-art service (TACR Governance Award 2018, CZ) developed by GISAT (Kolomaznik et al. 2016).

By applying multi-temporal InSAR techniques to a series of satellite SAR images over the same region, it is possible to detect movements of the structure systems on the ground in the millimeter/centimeter range and, therefore, to identify abnormal or excessive movement indicating potential problems requiring detailed ground investigation. (Lazecky et al. 2015)

Principles of InSAR measurement techniques and their use for monitoring of deformations in urban areas are illustrated by the two figures below.
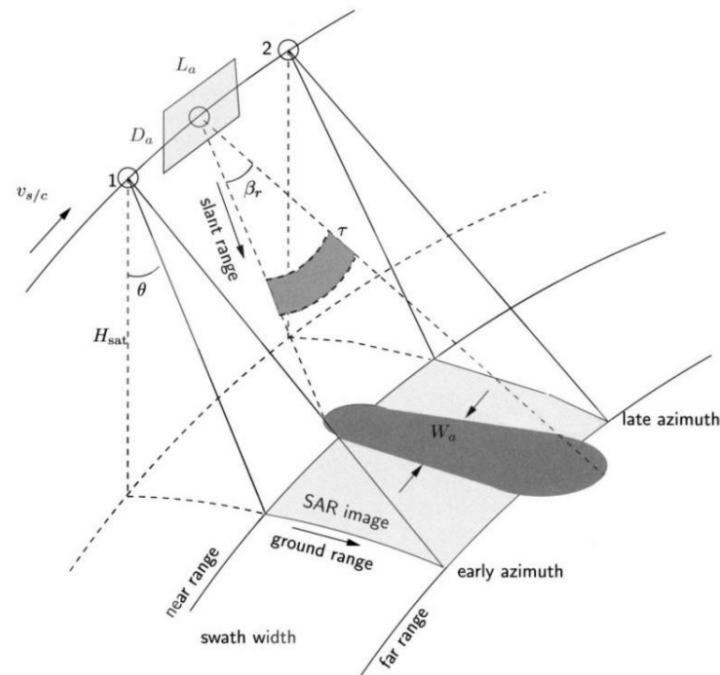
Figure 25*. Side-looking image geometry of a spaceborne SAR acquisition. The satellite velocity v_s is approximately 7 km/s. The dark gray area indicates the footprint of a single pulse. The total coverage of a SAR scene, between early and late azimuth direction, and near and far range, is depicted in light gray source: EGMS specification and Implementation EEA 2020 https://land.copernicus.eu/user-corner/technical-library/egms-specification-and-implementation-plan)*
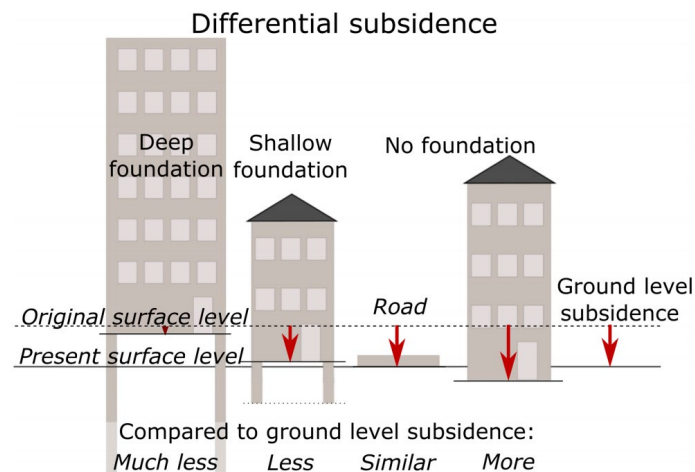
Figure 26*. Differential subsidence of individual objects and their relation between foundation depth and weight. Combining this relation with the PSI-estimated subsidence rates can be used to investigate and quantify depth-dependent subsidence rates. (source: Minderhoud et al. 2020)*

The subsidence processes are identified and monitored in a multi-temporal manner. The dense time-serie of SAR images (Sentinel-1) allows to follow displacements of selected coherent targets - permanent scatterers points by measuring phase differences between time-series of acquisitions and to estimate average displacement rate.

Figure 27. *Stable points with terrain/surface movements subsidence measurements, classified by velocity of movements in urban area.*

For each of measurement points the temporal profile is generated, showing the trend of displacements over the observation period as detected in satellite's line-of-sight direction, or as converted into vertical or horizantal (East-West) planes.
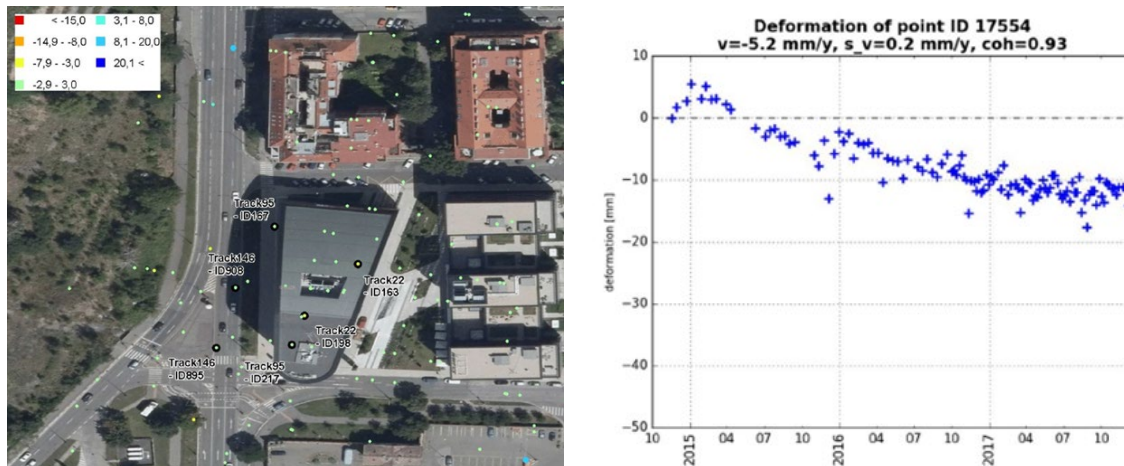
Figure 28. *Subsidence measurements for selected stable points in the city area classified by velocity of movements (left), temporal profile of subsidence for selected point.*

With a help of these techniques, the displacement rate (average annual velocity) is estimated for each point. Using this method, the points with ongoing subsidence (or other types of surface movements) can be detected. The points are categorized based on velocity of ongoing subsidence to be able to identify the most intensive subsidence processes in the city.

7.1.2.2 Integration with information on urban land structure and evolution

The second step of the methodology consists of **integration of the information about the subsidence with relevant additional data and information** in order to derive meaningful intelligence and understanding about the ongoing subsidence-related processes in the city and surrounding areas. This includes clustering of stable points with subsidence information and spatial overlay analysis (in particular zonal statistics) with the layers representing the structure and development of the city structure.

First, the information about the subsidence is converted to the level of meaningful (functional) urban units using primarily the geometry of the Urban Atlas layer (or building footprints), applying the zonal statistics, in order to obtain information about potential subsidence per each particular land use block. In this step, the Urban Atlas layer can be complemented by custom layers, representing different types of functional urban units, for which the information about subsidence should be derived (e.g. in the Moravian-Silesian region, this analysis can be done for brownfields or undermined areas). Also, similar type of analysis can be done with linear data representing street segments or underground infrastructure like pipelines.

Next, the information about terrain movements is combined with the WSF-Evolution dataset representing chronology of urban expansion of the cities (example in Figure 29). Based on this, temporal profiles of subsidence processes showing their timing (after the building block construction) can be prepared for each of the newly constructed units in the city area.
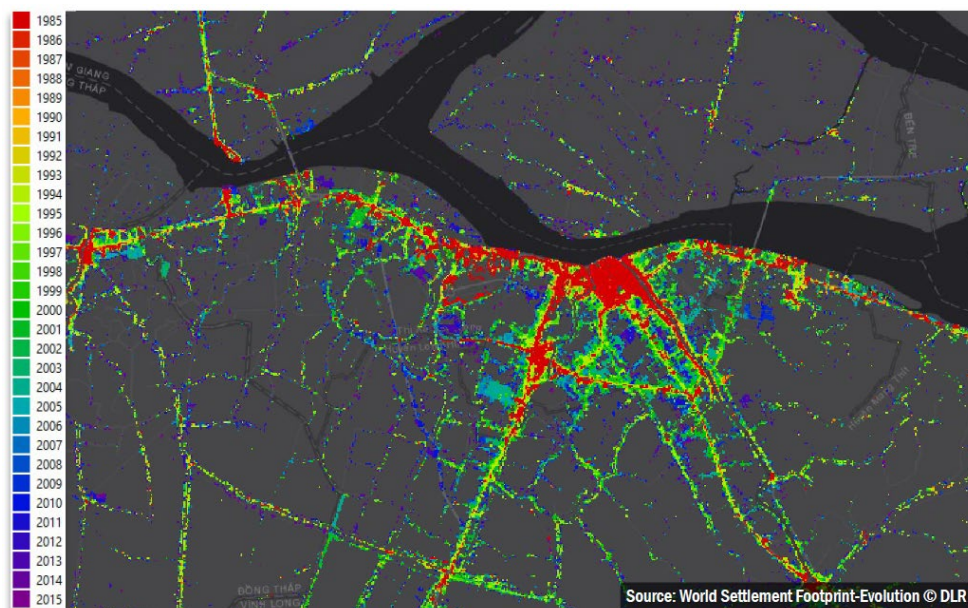
Figure 29. Spatial-temporal pattern of built-up expansion for selected city as depicted by World Settlement Footprint-Evolution (Marconcini et al. 2018). Colors represent year when built-up was detected for the first time in time series of satellite data. ((Source: EO4SD report, 2020)

Last, the presentation of the results of these analysis to the end-users will be secured by integration of the data-results into an interactive web-based analytical platform and visualised in an attractive and easy-to-understand manner. The app is based on open-source components and programming languages. Custom GIS layers can be integrated into this application as WMS or WFS, in order to combine these analytical results of the AP06 with the local-city data and information also in sense of visualisation.

7.2   Sample results for the front-runner and follower cities

The approach for generation of results of this service AP06 is similar to the one applied in case of the previous flood risk service (AP05). First, the initial estimation of subsidence-related hazard is prepared, using the above described multi-temporal InSAR method, to generate a layer quantifying annual subsidence velocity of on each of permanent scatterer points inside the AOI. Second, this layer is overlayed with Urban Atlas geometry, in order to obtain information about subsidence hazard for urban assets, here represented by functional urban blocks. This is physically the same dataset for which the flood hazard is evaluated, so as a result it combines information about both types of natural hazards - subsidence and flood - at the level of each Urban Atlas block (or Urban Atlas change layer block which contains all areas of change in land use between 2012 and 2018). Moreover, this natural hazard related information is combined with the information about the land use or about the character of local change, coming either directly from Urban Atlas (land use classification, in case of change layer for both 2012 and 2018, which allows for identification of the type of change) or from World Settlement Footprint layer, produced by DLR, which gives temporal information about the year of built-up. Again, as in case of AP05, information about subsidence hazard was collected also at the level of single buildings, distributed over the Heraklion city area (local third-party dataset).

These types of resulting layers (as well as various types of analysis based on these layers) are illustrated by the figures below.
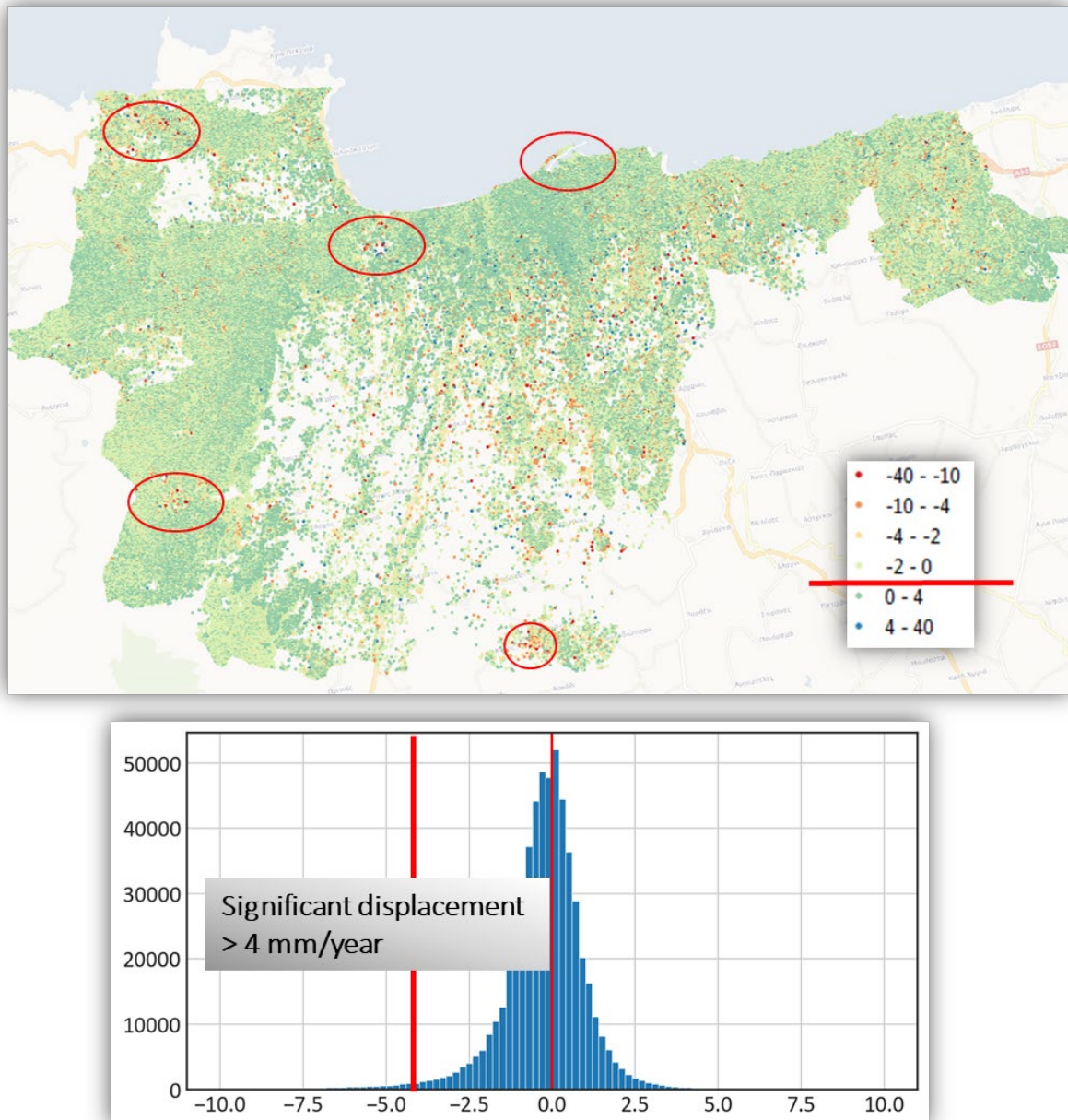
Figure 30. *Annual displacement rate (subsidence) on permanent scatterer points distributed over Heraklion city and surrounding area. The red lines/circles indicate locations with significant level of subsidence, with annual displacement rate higher than 4mm.*
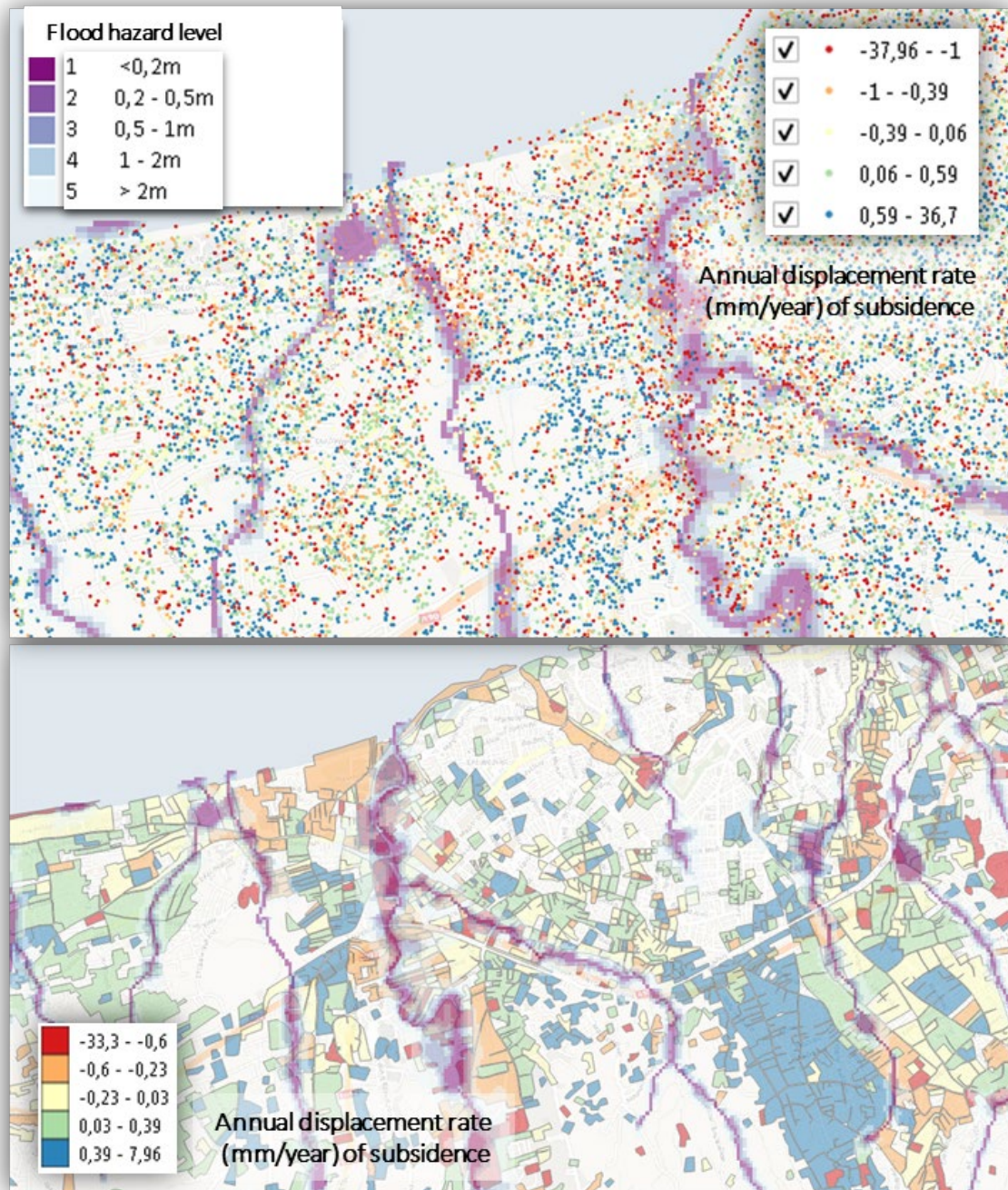
Figure 31. *Annual displacement rates (subsidence) on permanent scatterer points and per Urban Atlas blocks, distributed over Heraklion city and surrounding area, combined with information about flood hazard zones.*
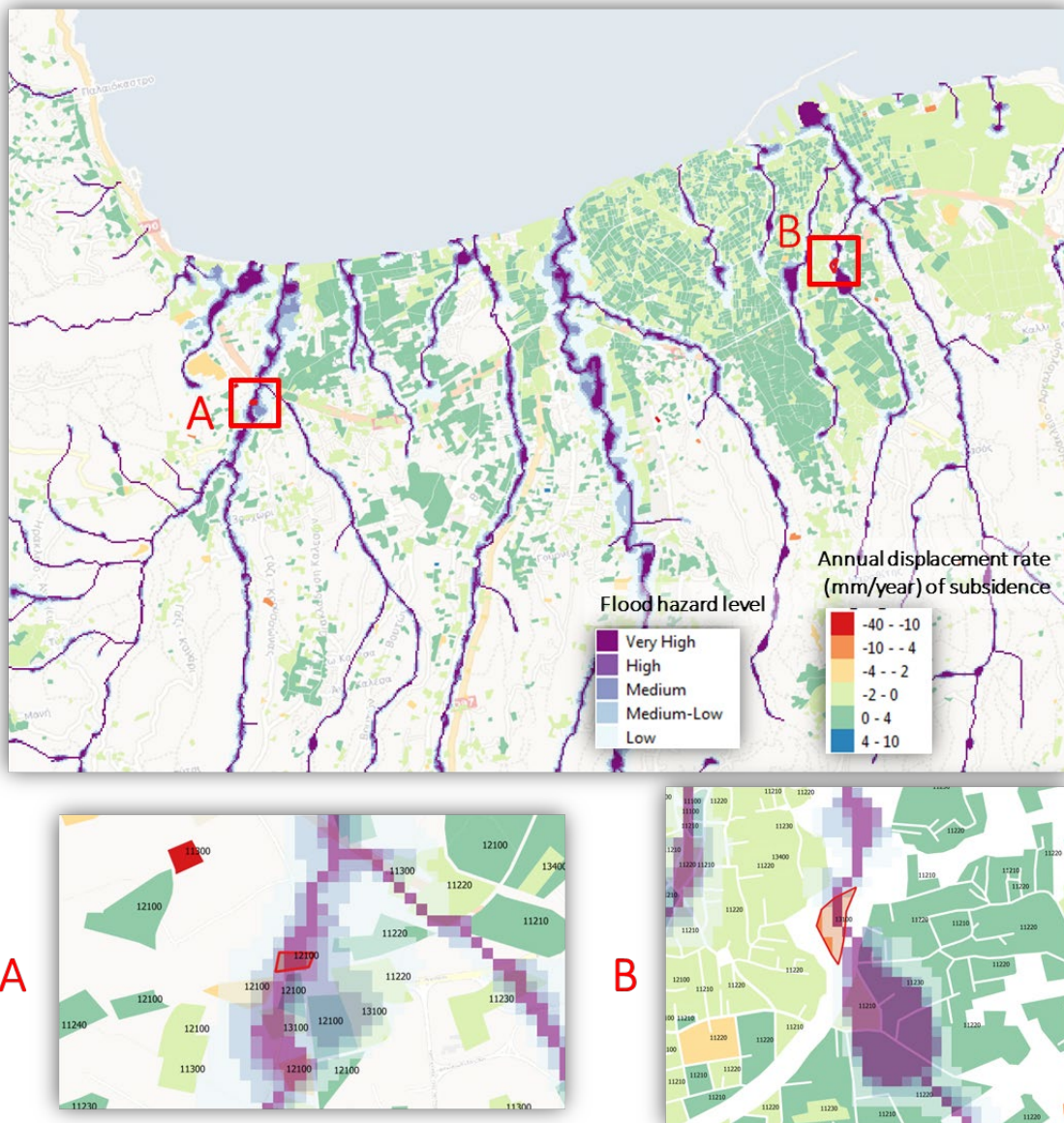
Figure 32. *Example of analysis based on combined AP05 and AP06 product – identification of urban blocks endangered by both flood and subsidence in the Heraklion city area.*

The application not only focused on geographical distribution of the hazard, but also on statistical evaluation of the hazard in context with other characteristics of the AOI. Following figure shows examples of such statistical evaluation. These statistics are generated automatically by the application so it can be prepared for any area of interest. Such statistics may be helpful to identify some interesting subsidence-related trends in the AOI.
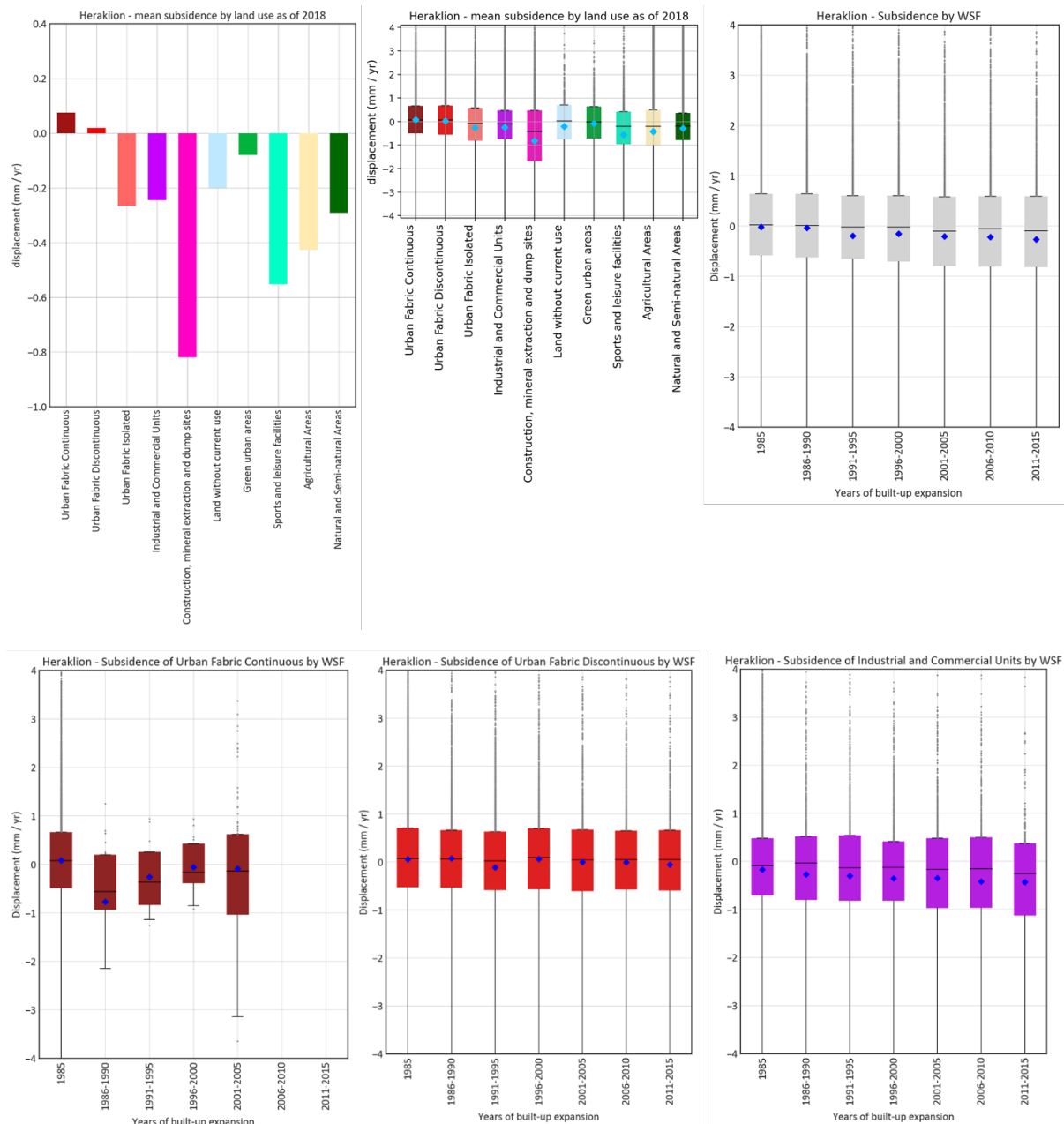
Figure 33. *Example of statistical evaluation of the subsidence hazard – for Urban Atlas blocks of different land use types and built-up in different years (according to WSF-based information).*

In case of follower city, we focused on particular on an undermined area (as a residual of coal mining activity in the Moravian-Silesian Region). This assessment was done on request of the local service end-user – regional authority. This area is called "POHO" and is intended for significant (re)development in the near future, therefore the assessment of subsidence-related hazard in this area is of crucial importance.
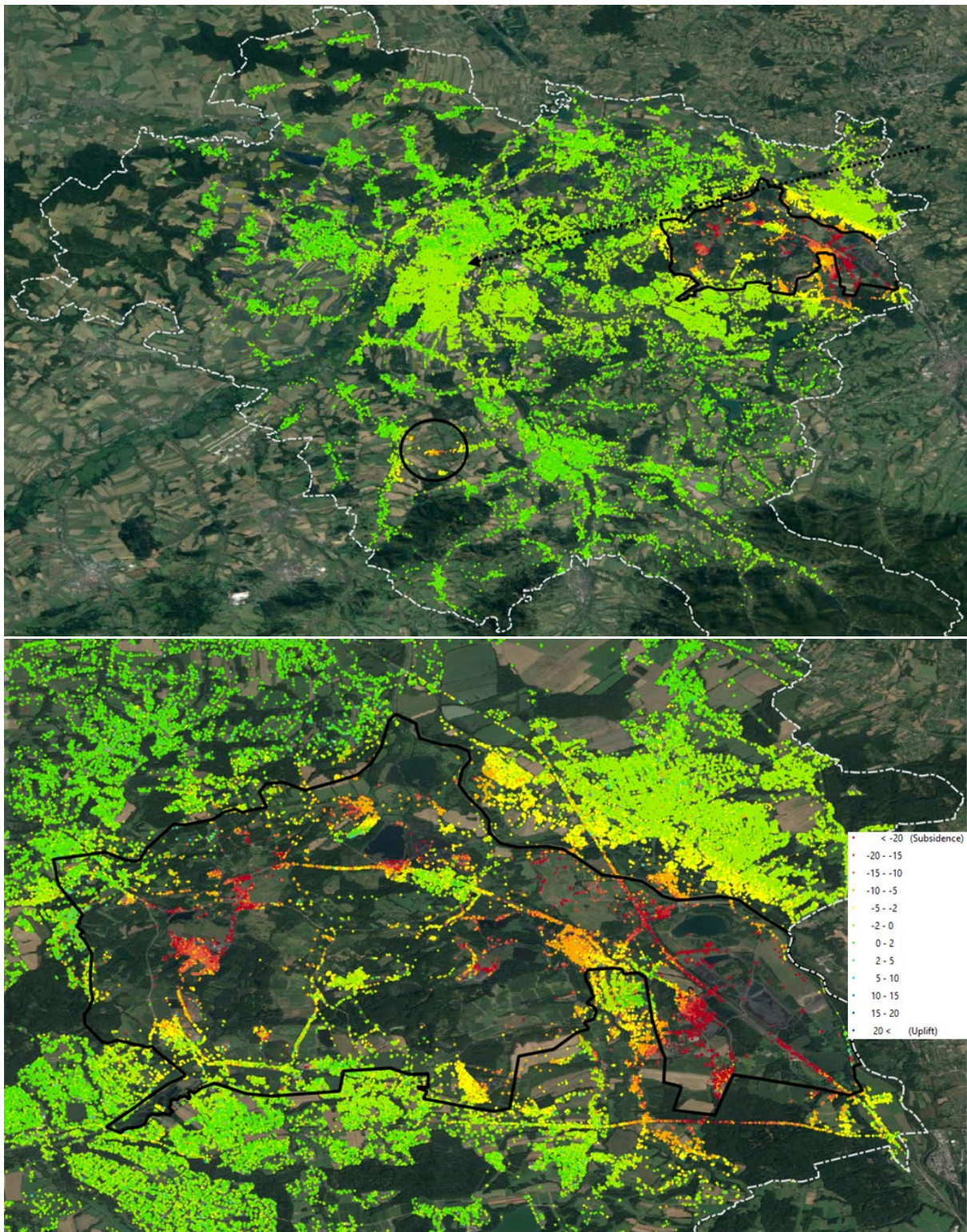
Figure 34. *Results of AP06 (vertical terrain movements) for the follower city-region Ostrava, with particular focus on POHO mining area with significant subsidence processes.*

Figure 35. *Results of AP06 (horizontal terrain movements) for POHO mining area in Ostrava follower city region.*

Moreover, we also prepared an assessment of the surface faulting hazard in the same area. Such analysis helps to identify not only subsidence on permanent scatterer points or their clusters, but more importantly also linear surface faulting, the which represents the biggest hazard related to subsidence processes, leading to high probability of real damage to building or infrastructure in the near future.
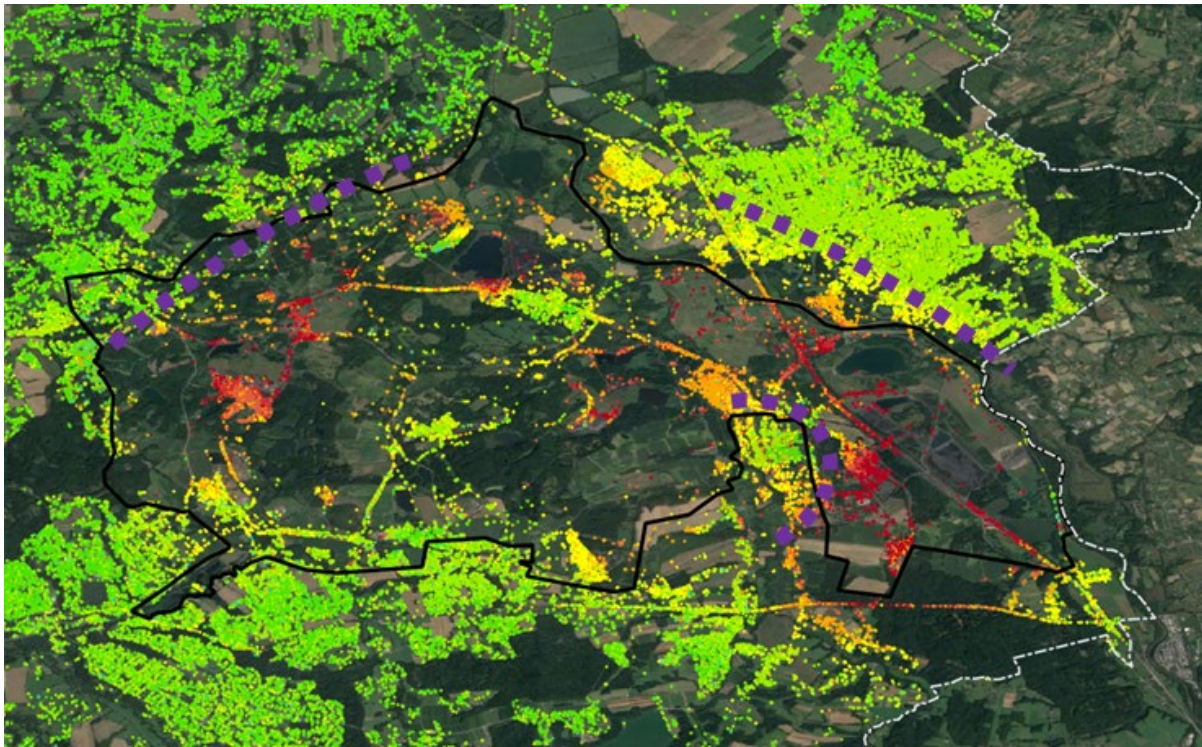
Figure 36. *Identification of linear surface faulting hazards caused by subsidence processes in the POHO area in Ostrava follower city-region.*

Again, based on overlay with Urban Atlas layer, statistical assessment has been prepared for the POHO region to identify differences in intensity of subsidence processes for different types of land use and for areas built-up in different years (according to WSF).

Figure 37. *Example of statistical evaluation of the subsidence hazard – for Urban Atlas blocks of different land use types and built-up in different years (according to WSF-based information). POHO region in Ostrava – highest level of subsidence detected for under-mined areas, with an increasing intensity trend.*
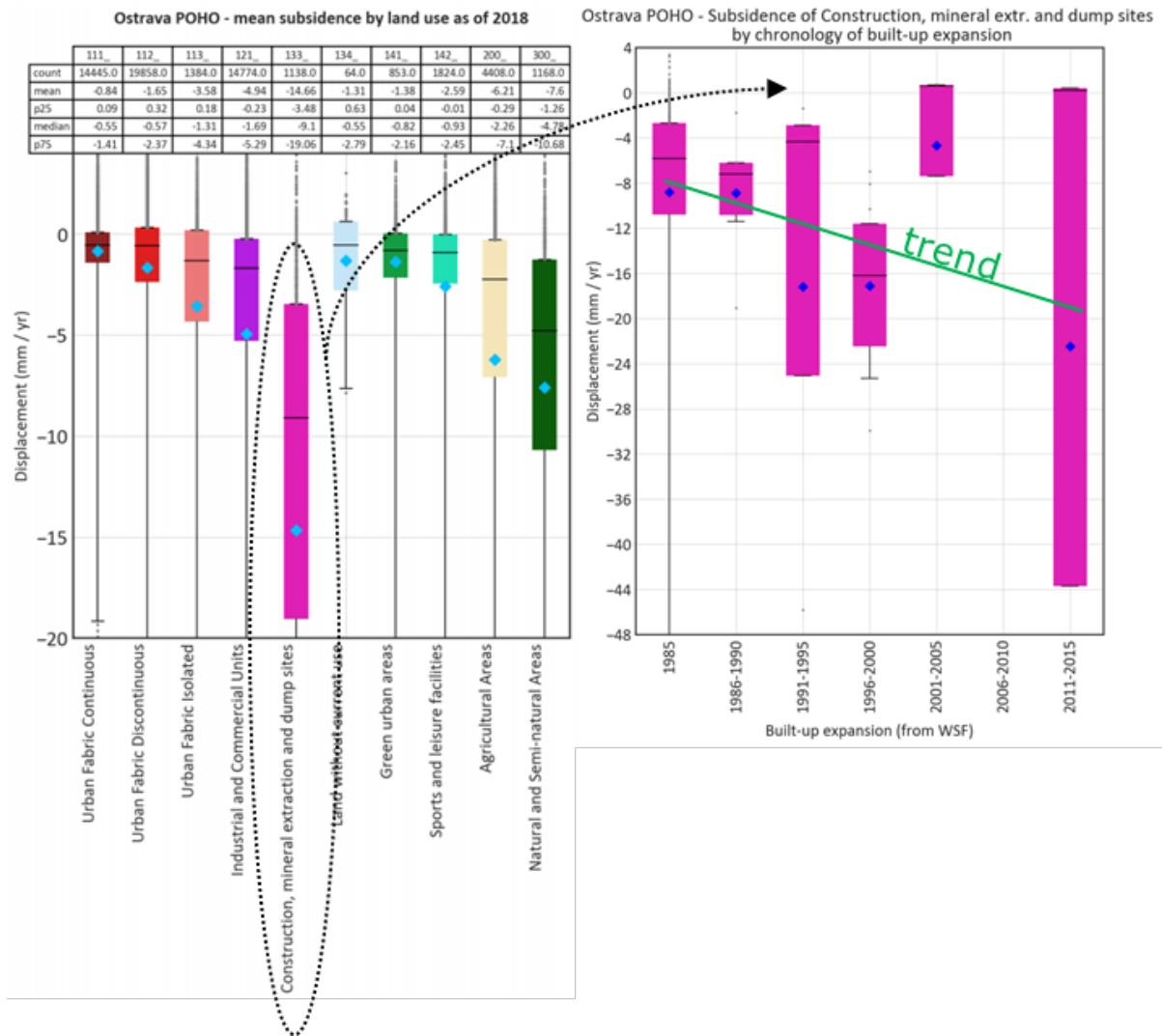
8 AP07 URBAN AIR QUALITY

8.1 Final Input Data & Methodology

8.1.1 Urban air quality

Urban air quality is a multi-scale problem. Pollutant concentrations on a street-level scale are influenced by regional background concentrations, urban increments due to local industrial, traffic and residential heating sources, and an additional contribution coming from recirculation in narrow streets with high rise buildings adjacent to it (the so-called street-canyons). Only when the contribution of all three scales is taken into account, the urban air quality exposure can be correctly determined. As illustrated in Figure 38, monitoring the compliancy of limit values also requires the combination of the three scales, as otherwise local exceedances could be overlooked.
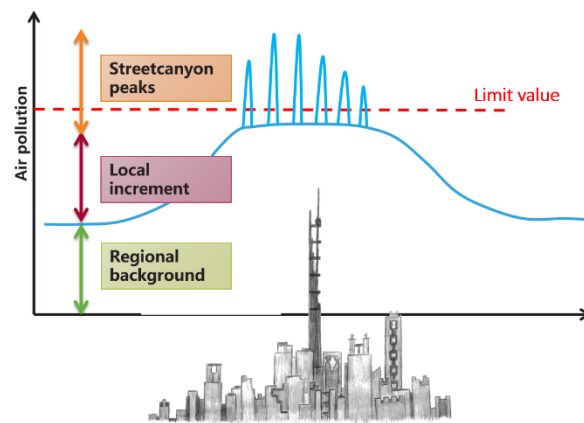
Figure 38. Illustration of the different scales involved in urban air quality assessment.

8.1.2 ATMO-Street model chain

CURE Application 07 assesses the urban air quality using the ATMO-Street application. ATMO-Street is an integrated air quality model chain (Lefebvre et al. 2013a), designed to correctly assess and combine the different scales of urban air quality. The model chain relies on several underlying models and input datasets to compute the air pollution at street-level scale (10m) for an urban area. The flowchart of the model chain is provided in Figure 39. In the next paragraph, we provide a general description of the model chain. Section 8.1.3 describes the model components and their interlinkage more in detail.

The ATMO-Street model chain starts from datasets describing the most important local emissions in the domain under consideration. For urban areas in Europe, road traffic, industrial and residential heating emissions are generally considered. Preferably, all three emission datasets are provided at a high resolution: residential and industrial sources are typically represented by a point source for each company / house with stove, while line sources (i.e.

one value per road segment) are used for road traffic emissions. If industrial and residential sources are not available at this high resolution, surface sources with a somewhat lower resolution (e.g. 5 by 5 km) can be used as an alternative. Based on the high-resolution emissions data, two core models compute the local contribution to the air pollution at a resolution of 10m: the bi-gaussian plume dispersion model IFDM accounts for the impact of local emissions from traffic and industry (Lefebvre et al. 2013b), while the street-canyon module OSPM calculates the in-street increment resulting from street-canyon effects (Berkowicz et al. 1997). To correctly assess the local contribution, these models require two additional datasets. Meteorological data (vectorial wind speed and temperature) is required to correctly assess the dispersion, while a detailed 3D building dataset (relying on building layouts using polygons) is required to correctly assess the recirculation in street canyons. In a final step, the total air pollution is computed by combining the local contribution with the regional background concentrations. These background concentrations contain the pollution caused by all the sources outside the model domain, and the sources that are not explicitly considered in the emission data (e.g. emissions for other sectors, such as shipping and non-road transport). This data is either based on results of regional background models or measurements (possibly combined with spatial interpolation using e.g. land use regression models).

The ATMO-Street model chain is the official air quality model chain in Flanders. It is used by the Flemish Environmental Agency for the assessment of current and future air quality, and its output is reported to the European Commission. The model chain has recently also been used in many other countries, including Poland, Slovakia, Hungary, Croatia and China. The model chain has been validated using several measurement campaigns, focusing on spatial patterns and time series alike (Lefebvre et al. 2011, Lefebvre et al. 2013a). Most of these validation campaigns focused on a relatively small number of sampling locations, with at most a few dozens of locations distributed among a single urban region. Recently, however, the Curieuzeneuzen Citizen Science air quality measurements have been used to validate the model using measurements for 20.000 sampling locations in Flanders (Hooyberghs et al. 2020). The validation highlights the capability of the model chain to correctly assess the spatial variation of the air pollution in Flanders.
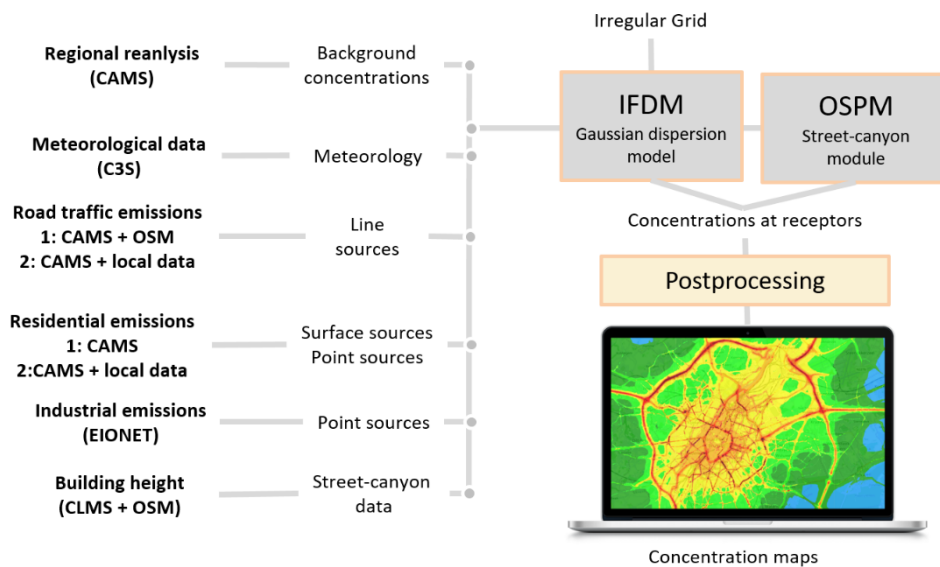
Figure 39. *Flowchart of the ATMO-Street model. The numbers refer to the two options for downscaling used in the current project (fully Copernicus or Copernicus combined with local data for downscaling). More details: see text.*

In CURE, the (raw) input data for the ATMO-Streets model chain stems as much as possible from Copernicus datasets. Emissions are retrieved from the Copernicus Atmosphere Monitoring Services (CAMS), meteorological data from the Copernicus Climate Change Service (C3S), and building information from the Copernicus Land Monitoring Service (CLMS). Additionally, industrial emissions of the European Environment Information and Observation Network (EIONET) have been used.

Although the resolution of the CAMS emission inventories for Europe has increased in recent years, there is still a significant gap between the resolution of the inventories and the resolution required in street-level scale urban air quality modelling. The emission data has therefore been combined with higher resolution proxy data to downscale the CAMS emissions to the requested resolutions (point sources / surface sources for residential emissions, and line sources for traffic emissions). For the frontrunner city Sofia, two options for the downscaling are considered. In the first set-up, we have relied on the global open-source roadmap OpenStreetMaps (www.openstreetmaps.org) to downscale the emissions to line sources, and used the residential emissions of CAMS at their native resolution (0.05 by 0.1 degrees). This first option is therefore transferable to any location in the European Union. In the second setup, a local bottom-up roadmap (with information on the road capacity) and a local dataset describing the location of heaters are as well considered. We expect that the final downscaled emissions of this second method are more in line with the real-life situation, but the method is no longer transferable to other cities.

To highlight the transferability of the former, open-source based methodology, this downscaling procedure is also applied for two follower cities, Bristol and Ostrava. For both cities, only this method solely based on open-source datasets is applied.

Table 7 provides an overview of the datasets used in the urban air application. Section 8.1.4 describes the input datasets and the downscaling of the emissions for both set-ups in more detail.

Table 7. Overview of the input datasets.

Copernicus service	Dataset	Type	Usage	Cities
CAMS	Regional air quality reanalyis	Air quality data	Background concentrations	Sofia, Ostrava and Bristol
CAMS	Regional Emissions for Air Pollutants (REG-AP), v3.1	Emissions	Road traffic and residential emissions	Sofia, Ostrava and Bristol
C3S	ERA5	Meteorological data	Meteorological data	Sofia, Ostrava and Bristol
CLMS	Urban Atlas	Building Height	Building height	Sofia
-	OpenStreetMaps	Building layout	Building layout	Sofia, Ostrava and Bristol
-	OpenStreetMaps	Road map	Downscaling traffic emissions	Sofia, Ostrava and Bristol
-	Road map Sofia	Road map	Downscaling traffic Emissions	Sofia
-	EIONET Large Point Source data	Point source data	Industrial emissions	Sofia, Ostrava and Bristol
-	Inventory of wood and coal burning heaters in Sofia	Location of heaters	Downscaling residential emissions	Sofia

8.1.3   Building blocks of the ATMO-Street model chain

Local open-street concentrations due to traffic emissions and point sources are modelled by the bi-Gaussian plume model IFDM (Immission Frequency Distribution Model) (Lefebvre et al. 2013b). IFDM is a receptor grid model: air pollutant concentrations are computed for an abundance of receptor locations. Instead of a regular grid, we use a pointsource- and road-following grid. This approach ensures that more receptor points are available where the largest concentration gradients are expected (Lefebvre et al. 2011). The chemical equilibrium in the

NOx-O3 reaction is determined on the basis of temperature and solar height and is based on the fast-ozone-chemistry scheme (Berkowicz et al. 2008).

To take the effect of buildings on the street level concentrations into account, the IFDM model is coupled to the Operational Street Pollution Model (OSPM) (Jensen et al. 2017). OSPM models street level concentrations due to traffic emissions using a combination of a plume model for the direct contribution and a box model for the recirculating part of the pollutants in the street. In the current set-up for OSPM, a receptor location is placed every 20m on each road with a row of buildings adjacent to the road (i.e. at a maximum distance of 50m to the middle of the road).

The concentrations at the receptor locations of the IFDM and OSPM model are combined and gridded in a three-step postprocessing module. At first, IFDM results are gridded using Delaunay triangulation to obtain gridded open street concentrations. Secondly, we grid the OSPM results using nearest-neighbour interpolation. In the last step, both gridded maps are combined into a map with a 10m resolution, by using the OSPM results at locations where buildings are adjacent to the road, and the IFDM results at all other locations.

8.1.4 Input data for the core city Sofia

Table 7 provides an overview of the datasets used in the urban air quality application. In the following paragraph the datasets and the required processing are described in more detail. In this paragraph, we describe the model input for the frontrunner city Sofia, while the next paragraph focuses on the modifications applied for the follower cities Bristol and Ostrava.

8.1.4.1 *Meteorological data*

ATMO-Street requires hourly (vectorial) wind speed and temperature data. Both parameters are taken from the ERA5 reanalysis dataset of the Copernicus Climate Change Service (C3S). ERA5 provides surface temperature and wind speed with a resolution of 30 kilometre. We interpolate the data to the centre of the domain using bilinear interpolation.

8.1.4.2 *3D building model*

To correctly assess the street-canyon contributions, ATMO-Street requires a 3D model of the city under consideration. The 3D model requires at least the following two parameters:

- Building height
- Ground plan of the building, preferably described using a polygon (sub-meter resolution is required).

Building heights are available in the CLMS Urban Atlas for all European capitals. Although the dataset is already a few years old (dating from 2012), we assume that the urban fabric has not changed too much in the European capitals.

The Urban Atlas provides building heights at a resolution of 10m, but it does not provide a building layout. Since the façade-to-façade distance is one of the most important parameters

in street-canyon models, an additional dataset is required to build a full 3D model of a city. We make use of the open-source OpenStreetMaps dataset, which includes a polygon layer with the exact location of the buildings. Figure 40 further visualizes the gridded CLMS data and the polygon of OpenStreetMaps.
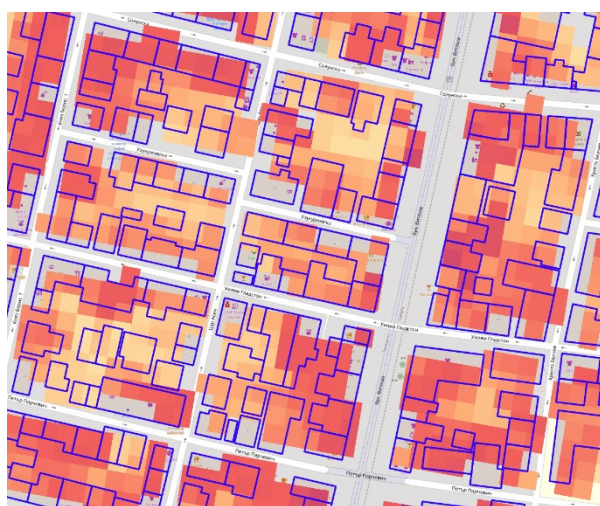
Figure 40. Illustrations of the two datasets used for the 3d building model. The blue lines indicate the ground plan of the buildings according to OpenStreetMaps data, while the yellow-to-red colors indicate the building height according to the 10m resolution UrbanAtlas dataset. Background image: OpenStreetMaps.org.

As OpenStreetMaps is a crowd-sourced project, the quality and completeness of the data varies greatly between different areas. We have controlled the completeness for Sofia using a visual comparison with satellite data, and with the (lower resolution) building height of Urban Atlas. Most buildings in the inner-city are correctly represented, and only some residential neighbourhoods in the outskirts are missing a considerable number of buildings. These locations are however not important for the air quality applications, as the highest concentrations are expected in the inner-city.

The CLMS and OpenStreetMaps data are combined using geospatial tools. For each building polygon in OpenStreetMaps, we determine the mean height of the overlapping grid cells from the CLMS Building Height layer.

8.1.4.3 Background concentrations

ATMO-Street's components IFDM and OSPM only explicitly take the concentrations due to traffic, residential and industrial emissions in the city into account. Concentrations due to other emissions in the city (e.g. rail transport, trade and services etc) and emissions outside the city are not taken into account. These 'background' concentrations vary over a longer spatial scale (order of kilometres rather than order of metres), and are therefore not explicitly modelled in the urban air quality applications. They are, however, added to the final concentrations field using a regional background concentration from CAMS.

CAMS provides hourly regional background concentrations for Europe in the 'Regional reanalysis datasets.' This dataset assimilates the output of regional air quality models (so-called chemical transport models, CTMs) with measurements of the official measurement networks of the EU-countries. The resulting dataset comprises gridded hourly concentrations for Europe with a resolution of 0.1 degree, for nitrogen dioxide, ozone, and particulate matter. The most recent dataset contains concentrations for 2018.

Directly coupling the background concentrations to the local concentrations field would give rise to sharp gradients at the edges of the CAMS grid cells. Therefore, the CAMS data are resampled to a concentration field with a 2000m resolution using bilinear interpolation.

8.1.4.4 Emissions

ATMO-Street requires high resolution emission data for road traffic, industry (including powerplants), and residential heating. In the following paragraphs, these three sectors are discussed in detail.

Industrial emissions

For industrial emissions, we rely on the figures reported by the member states of the European Union to the Central Data Repository (CDR) of the European Environment Information and Observation Network (EIONET). According to directive 2016/2284/EU the member states must every four years report the air pollutant emissions of large point sources (LPS), which the EU subsequently reports to the United Nations Economic Commission for Europe (UNECE) Environment and Human Settlements Division under the Convention on Long-range Transboundary Air Pollution (CLRTAP).

The data for Bulgaria is publicly available on http://cdr.eionet.europa.eu/bg/un/clrtap/lps/envwqsyda/. We use the data reported in 2017 (which refers to the situation in 2015). For Sofia, the dataset contains emissions for four powerplants and one industrial plant. In all five cases, a high stack is present (ranging from 70 to over 130m high), and it is therefore expected that the influence of these industrial emissions on the ground concentrations is rather limited.

Road traffic emissions

Several global and regional emissions datasets have recently been developed under the CAMS umbrella (CAMS 2019). In the current set-up, we use the CAMS regional anthropogenic emissions for Europe, using the CAMS–REG-v3.1 dataset developed by TNO. This dataset provides gridded emissions on a 0.1 by 0.05 degree resolution for several sectors (including road traffic and residential combustion) and several air pollutants (including NO2 and PM10). Version 3.1 of the dataset provides total annual emissions for 2016. Monthly profiles are provided by the CAMS-TEMPO dataset.

ATMO-Street requires emission data for all the line segments in the domain. The total CAMS emissions in Sofia have therefore been combined with higher resolution proxy data to

downscale the CAMS emissions to the requested resolutions. As mentioned above, two options have been considered: a first option relying on pan-European datasets, and a second option relying on local datasets. More in detail, the downscaling uses the following proxy data:

1. In the pan-European methodology, the road map of OpenStreetMaps is used. The emissions are spread over all the roads in the domain according to the number of lanes for each road (thus assuming that more vehicles are using roads with a larger number of lanes). Moreover, we assume that the emissions on a highway segment (roadtype trunk or motorway in OSM) are twice as large as the emissions on other types of roads, because vehicle speeds and vehicle numbers are in general larger on highways. Note that is method is rather crude, and does not use any local knowledge.

2. The local method uses a bottom-up dataset of the Sofia municipality. The dataset indicates for each road the maximal capacity of the road. We assume that the emissions can be spread over all the roads according to their maximal hourly capacity. Note that this method is less crude than the pan-European methodology, but it is still far from perfect. In an ideal situation, the CAMS emissions are either spread over the domain according to realistic traffic flows, which consider the morphology of the city (e.g. some roads link residential and office areas, and are therefore much more used during rush hours etc). Alternatively, the road traffic emissions could by calculated using a traffic emission model, which combines the traffic flows with the traffic fleet and bottom-up emission factors.

Residential emissions

For the residential emissions, we anew start from the CAMS REG-AP-v3.1 dataset, but this time we use the data for the residential combustion sector. The rest of the processing differs for both set-ups:

1. When only using pan-European datasets, there is no decent proxy data to further downscale the emissions to individual houses or wood / coal burning devices. We therefore use the emissions on a 0.05 by 0.1 degree resolution. The emissions are therefore spread over the entire urban area, and we will certainly miss some important PM hotspots in neighbourhoods with a large share of wood and coal burning.

2. The Sofia municipality has compiled a large dataset containing the location of all coal and wood burning heaters. In the second method, we spread the total emissions in Sofia uniformly over all these devices. Note that this entails an important assumption, and will cause some uncertainty. After all, in real-life, the emissions of individual heaters strongly depend on the characteristics of the heater (type, age, maintenance...), and the way in which the heaters are used. This type of data is, however, not available at the level of individual heaters in the entire city.

8.1.5   Input data for the follower cities Bristol and Ostrava

The methodology to gather the input data for Bristol and Ostrava mimics the one for the frontrunner city Sofia. However, as some datasets are unavailable for follower cities, we have to modify the roadmap a little. In this section, we provide an overview of the updates to the methodology. Datasets that are not mentioned in the following paragraphs, are composed in exactly the same way as the ones for Sofia.

The only pan-European dataset that is unavailable for Bristol and Ostrava is the Building Heights dataset of CLMS, which is currently only available for the European capitals. For the follower cities, we therefore use a rough estimate for the building heights: we assume a fixed building height of 15m for each building in the domain. This rough estimate will have an influence on the quality of the model results for street-canyon locations.

The local datasets for Sofia (location of coal and wood burners and road capacity) are also unavailable for the follower cities. For these cities, we will hence only use the downscaling method based on the pan-European OpenStreetMaps dataset for the traffic sector, and only use the CAMS residential emissions at their native resolution (0.05 by 0.1 degree).

8.1.6   Limitations and validation

As mentioned in the earlier paragraphs, there are several limitations and uncertainties related to the methodology applied for the urban air quality application. Most of the uncertainties are related to the Copernicus datasets and the downscaling of these data to the required resolution, but there is an additional uncertainty related to the model core (IFDM-OSPM). We for instance observe the following limitations:

- The background concentrations are based on the CAMS regional reanalysis data, which are the result of an air quality model on a regional scale. Although the results have been assimilated with measurements, we have observed underestimations of the background concentrations by CAMS in other cities (e.g. Bratislava).
- Similarly, wind and temperature input data are an assimilation of model data and measurements. Although the quality of these type of reanalysis products has been greatly improved recently (e.g. with the update from ERA-Interim to ERA5), there could be some deviations from the actual local data.
- Downscaling the emissions to individual point sources and road segments comes with an important uncertainty. The quality of the downscaling greatly depends on the quality of the proxy data that have been used. We thus expect better results if we rely on a combination of local data and pan-European / global proxy datasets. Note, however, that although the local datasets are the best available proxy data, they are not the ideal proxy data (e.g. capacity instead of traffic volumes / no information on wood / coal burning heaters).
- For the follower cities, only a rough estimate for the building heights is used (fixed buildings height of 15m). This assumption will cause large uncertainties for the street-

canyon concentrations, which are very sensitive to minor changes in the building heights.

- The model has initially been developed to model the air quality in Flanders, and therefore relies on a stability scheme based on measurements in Flanders.

8.2 Sample results for the front-runner and follower cities

8.2.1 Total annual mean concentrations

The primary outcome of the air quality application are air quality maps describing the yearly mean concentrations of nitrogen dioxide (NO_2) and particulate matter (PM_{25}) with a resolution of 10 by 10 meters. We focus on the year 2018, as it is the most recent year for which background concentrations are available.

The figures below show sample results for Sofia, Ostrava and Bristol. For Sofia, we show the results of both set-ups described in the previous paragraph. The maps highlight how the urban air quality varies strongly over short distances. For NO_2, the highest concentrations are observed near the most important roads, with the highest concentrations occurring in busy street canyons in the city centre. The highest concentrations for particulate matter are, on the other hand, observed in the neighbourhoods with an abundance of residential emissions, especially when considering the runs in which the Copernicus data has been supplemented with local data.

The results for the frontrunner city Sofia moreover highlight the major differences between both set-ups. Although the total emissions in the domain are the same for both set-ups, the spatial pattern of the air pollution is markedly different. The contribution of the residential sector is much more homogeneous for the set-up only relying on open-source datasets, which is caused by the emissions being spread over the entire metropolitan area (instead of being focussed on the areas in which most heat burners are located). These differences are due to the large gap in resolution between the input Copernicus data and the high-resolution model chain, and highlight the need for local data to improve the final concentration maps.

The maps allow stakeholders to identify the neighbourhoods and districts with the worst air quality, and to decide in an informed manner for which areas action should be prioritized. Moreover, the maps can be used for compliance checking. The EU Ambient Air Quality Directive sets a threshold of 40 µg/m³ respectively 20 µg/m³ for the yearly mean NO_2- and $PM_{2.5}$-concentrations. We thus observe a breach of the standards for NO2 in the busiest street canyons, while the standards for $PM_{2.5}$ are breached at most locations in the city centre. The more stringent updated WHO guidelines (10 µg/m³ for NO_2, and 5 µg/m³ for $PM_{2.5}$) are exceeded at all locations in the model domain, both for NO_2 and $PM_{2.5}$, indicating that significant negative health impacts are observed everywhere in the metropolitan area.
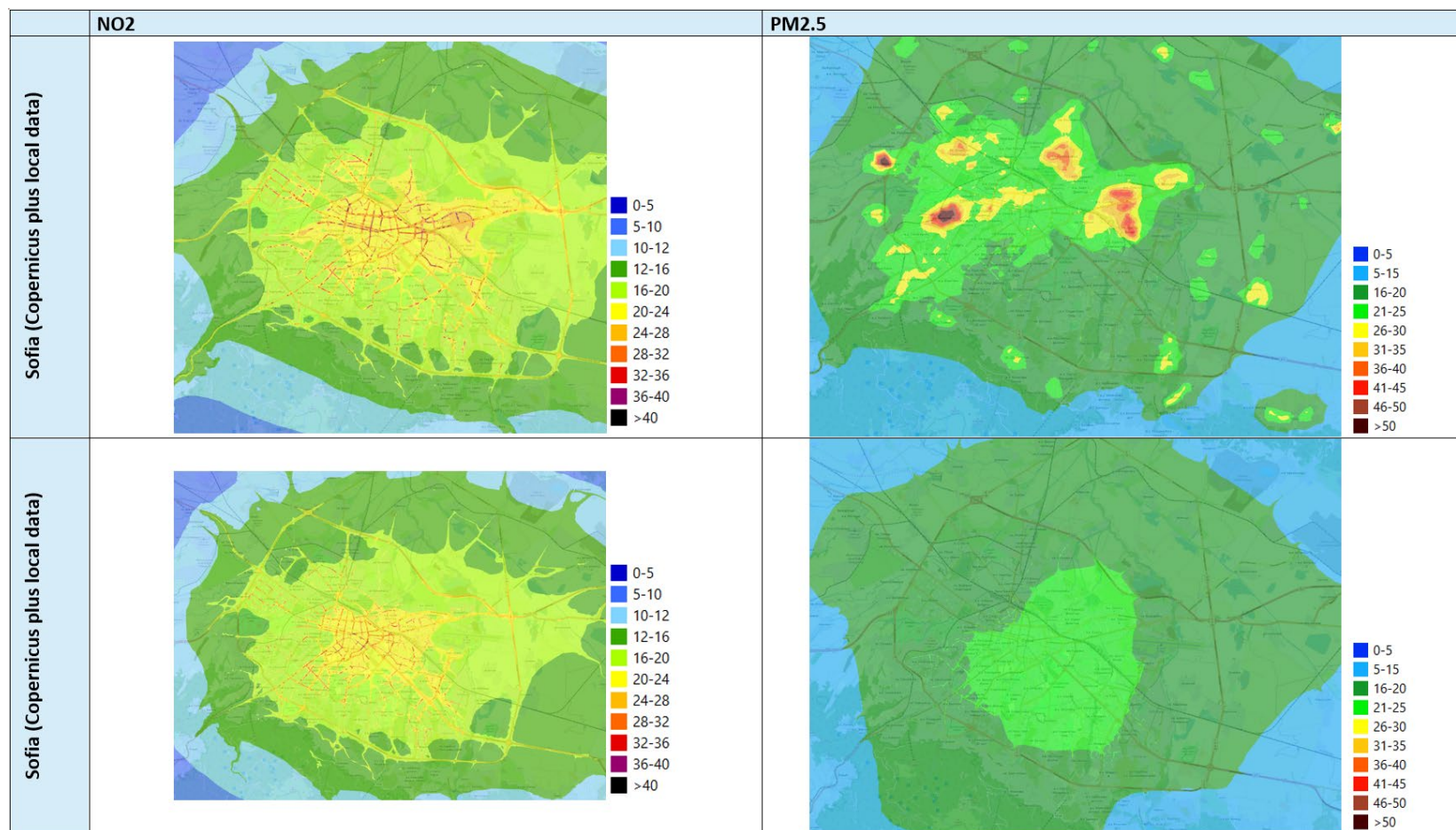
Figure 41. *Total annual mean concentrations in μg/m³ for the core city Sofia. The left figures show the NO₂-pollution, while the right figures provide the results for PM₂.₅. We show both the results for the methodology using only Copernicus data (bottom row), and the methodology in which the downscaling of the emissions is complemented with local data (top row).*
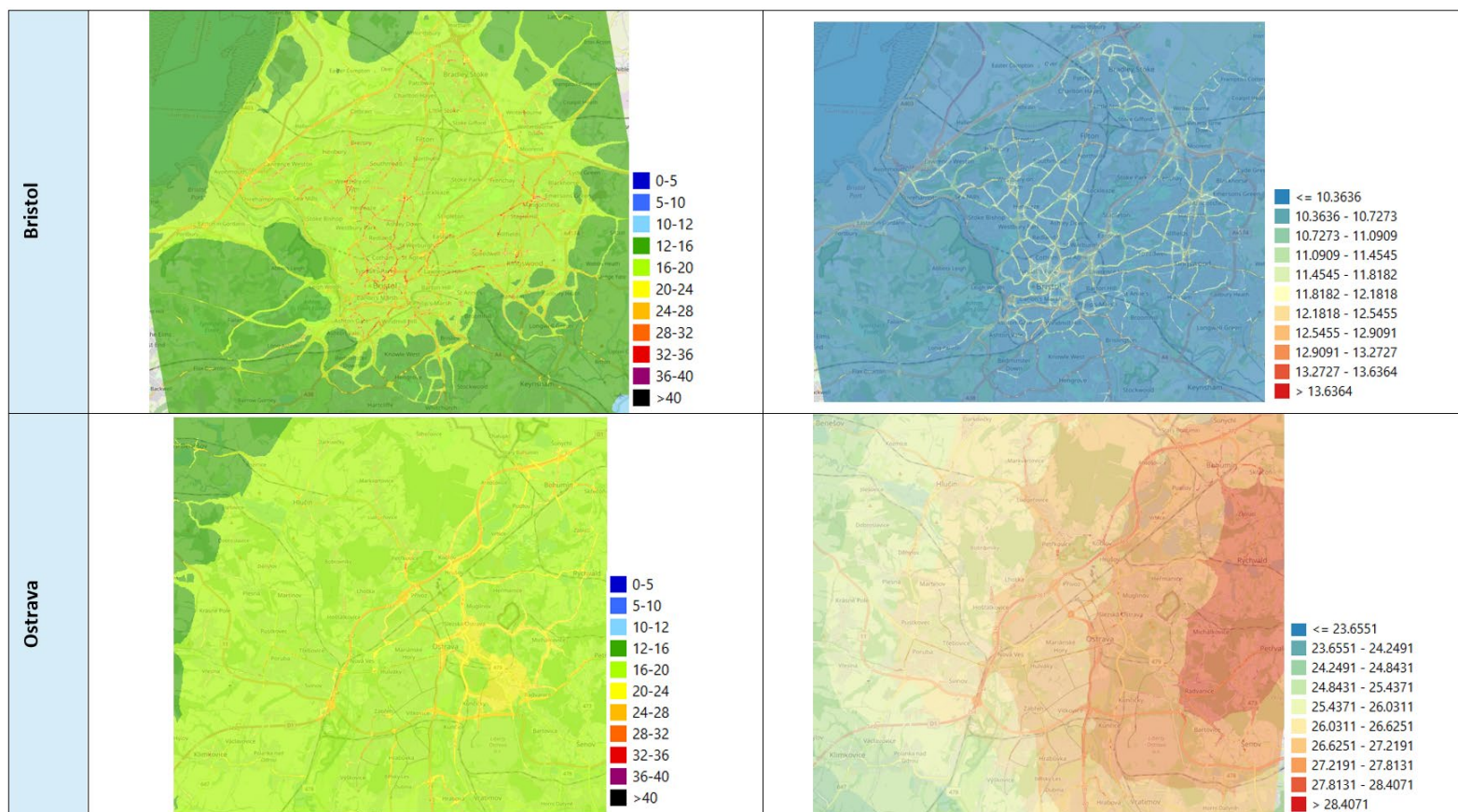
Figure 42. *Total annual mean concentrations in µg/m3 for the follower cities Bristol and Ostrava. The left figures show the NO₂-pollution, while the right figures provide the results for PM₂.₅.*

8.2.2   Sector contribution

A second output of the urban air application concerns the sector contribution. For each of the sectors that are explicitly considered in the local modelling (road traffic, industry, power plants and residential heating), also the approximate contribution of the individual sector to the total concentration is provided[5]. Using these results, stakeholders can identify key sectors for which measures are prioritized. The sector contribution also provides a rough estimate for the (theoretical) maximal pollution reduction due to local measures for the sector under consideration. Sample results for Sofia (based on the air quality modelling relying on Copernicus data supplemented with local datasets for the emission downscaling) are shown in the figure below, both for NO_2 and $PM_{2.5}$. The sample results for particulate matter for instance highlight the importance of the urban residential emissions at this specific location. Also, the urban traffic emissions contribute a significant fraction to the total concentrations, whereas the urban power plant and industrial emissions are responsible for only a negligible fraction of the total pollution. Approximately a third of the pollution at this specific location is emitted outside the domain, or by sectors that are not explicitly considered in the modelling. The results for NO_2 can be interpreted in a similar way, indicating the importance of the traffic emissions at this specific location.

---

[5] For particulate matter, the sector contribution is the exact contribution. For nitrogen dioxide, providing an exact contribution is impossible because of the chemical interaction with ozone.
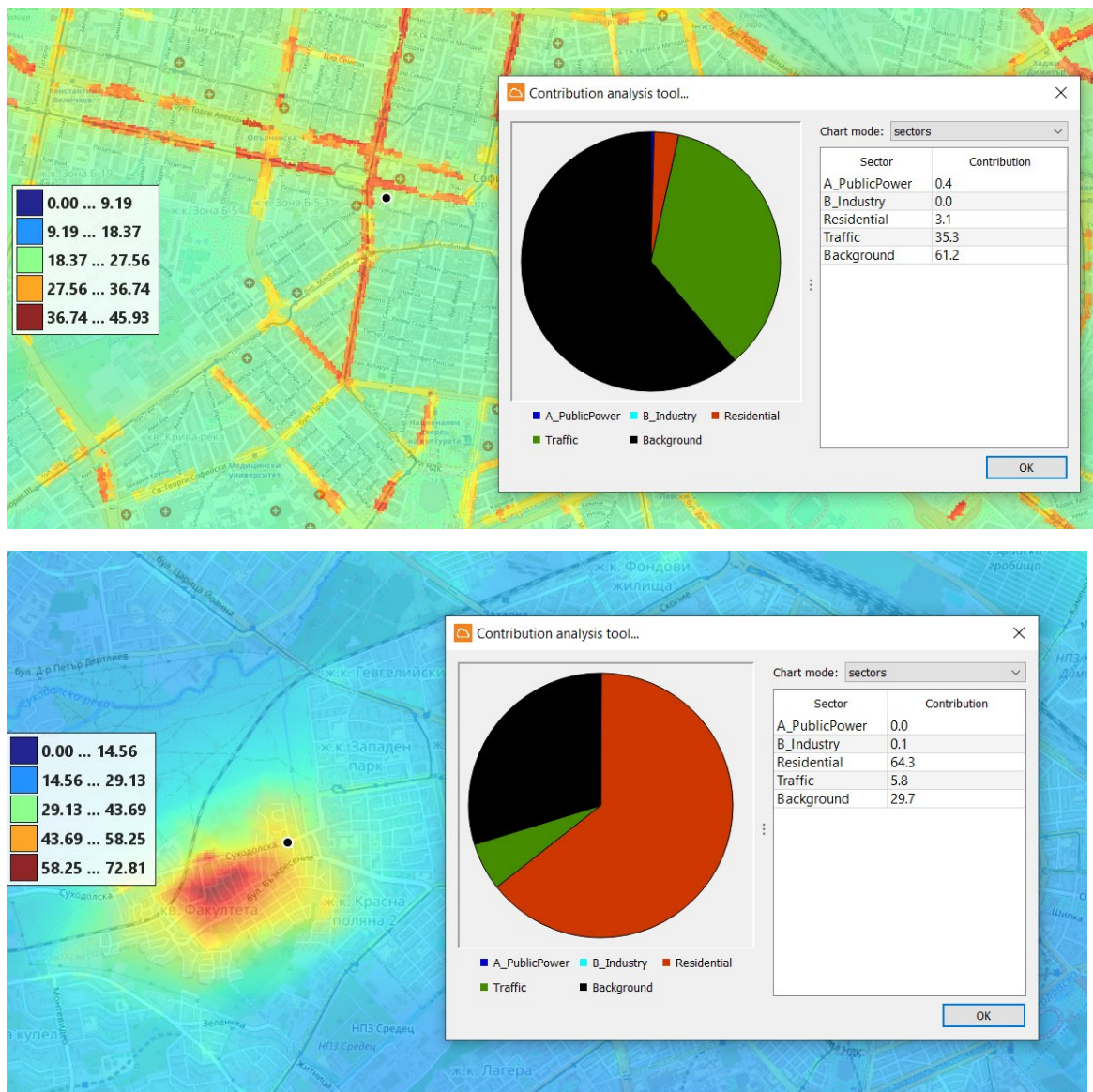
Figure 43: *Sector contribution in Sofia (based on the air pollution model chain relying on the Copernicus data, supplemented with local data for the downscaling of the emissions). The figures show the relative contribution of the different emission sectors to the total concentration at the location of the black dot on the map, for NO₂ (top figure) and PM₂.₅ (bottom figure). The following sectors are considered: traffic (green), public power (blue), industry (light blue, no contribution at the locations shown), residential (red) and the background concentration (black).*

9   AP08 Urban Thermal Comfort

9.1   Final Input Data & Methodology

To study the urban microclimate, VITO has developed the urban boundary layer climate model "UrbClim", designed to cover individual cities and their nearby surroundings at a very high spatial resolution (De Ridder et al., 2015). UrbClim consists of a land surface scheme, coupled to a 3-D atmospheric boundary layer module. The land surface scheme is based on the soil–vegetation–atmosphere transfer scheme of De Ridder and Schayes (1997), but is extended to account for urban surface physics. The model has been applied to and validated for over 10 cities worldwide (De Ridder et al., 2015 ; Garcia-Diez et al., 2016 ; Lauwaet et al., 2015 ; Lauwaet et al., 2016 ; Zhou et al., 2016). The model operates at a typical horizontal resolution of 100m, and provides the local meteorological input variables for the high resolution thermal comfort module.

To set up the 100m resolution model simulations, several Copernicus input datasets are needed (Table 8). The spatial distribution of land cover types, needed for the specification of required land surface parameters, is taken from Urban Atlas (2018), and converted to relevant classes for the UrbClim model. Terrain height is specified by the EU-DEM map. The UrbClim model needs also information on the soil sealing and vegetation cover fraction in each grid cell. The percentage urban land cover is specified using the Imperviousness data from CLMS, and the vegetation cover fraction from the NDVI data set. More details about these data sets can be found in D2.1 of the CURE project. The model is driven by large-scale meteorological data from the C3S ERA5-reanalysis. The model output consists of hourly 2m air temperature, humidity and wind speed fields, as well as land surface temperatures.

Table 8. *Overview of the input datasets for the 100m resolution background UrbClim simulations.*

Copernicus service	Dataset	Usage
CLMS	Urban Atlas	Specification of land use classes
CLMS	EU-DEM	Specification of terrain height
CLMS	Imperviousness	Specification of soil sealing % in grid cell
CLMS	NDVI	Specification of vegetation % in grid cell
C3S	ERA5	Large-scale meteorological input data

These data give a good overview of the spatial distribution of air temperatures (which don't vary much over short distances) and the Urban Heat Island effect of a city. However, air

temperatures don't tell the complete story of heat stress experienced by citizens. Also the radiation load (both shortwave and longwave), humidity and wind speed are important factors to quantify human thermal comfort. An indicator that takes all these variables into account is the Wet Bulb Globe Temperature (WBGT), which is calculated as follows:

$$WBGT=0.7×Tw+0.2×Tg+0.1×Ta$$

with Tw = the wet bulb temperature, Tg = the black globe temperature and Ta= the air temperature.

The Wet Bulb Globe Temperature has a long tradition of being used as a thermal comfort index and is the ISO standard for quantifying thermal comfort (ISO, 1989). It is currently in use by a number of bodies including the US and UK Military, civil engineers, sports associations and the Australian Bureau of Meteorology (Willett and Sherwood, 2012). It is the only heat index to have known thresholds based on a large number of observations, developed by the U.S. Army (2003) (Table 9). The WBGT can be measured easily with rather cheap equipment, making it an ideal indicator for model validation and citizen science campaigns to raise awareness about heat stress issues.

Table 9. Heat stress category limits of the U.S. Army (2003).

Heat Stress Category	WBGT [°C]
1	≤ 25.6-27.7
2	27.8-29.4
3	29.4-31.0
4	31.1-32.1
5	≥ 32.2

By combining the standard output of VITO's UrbClim model with detailed radiation calculations based on 3D building and vegetation data, it is possible to calculate the WBGT with a very high spatial resolution (Lauwaet et al. 2020). The methodology used by VITO is adopted from the paper by Liljegren et al. (2008), the recommended method to calculate outdoor WBGT values (Lemke and Kjellstrom 2012). As input for these calculations, additional Copernicus data sets are needed, which are listed in Table 10. Figure 44 shows an example of the high resolution input data for the city center of Copenhagen.

Table 10. Overview of the input datasets for the high resolution WBGT module.

Copernicus service	Dataset	Usage
CLMS	Urban Atlas Street Tree layer	Specification of tree locations in cities
Copernicus Data Warehouse	Very High Resolution land cover map	Specification of land use classes

Buildings
Trees
Sealed surface
Low vegetation
Water
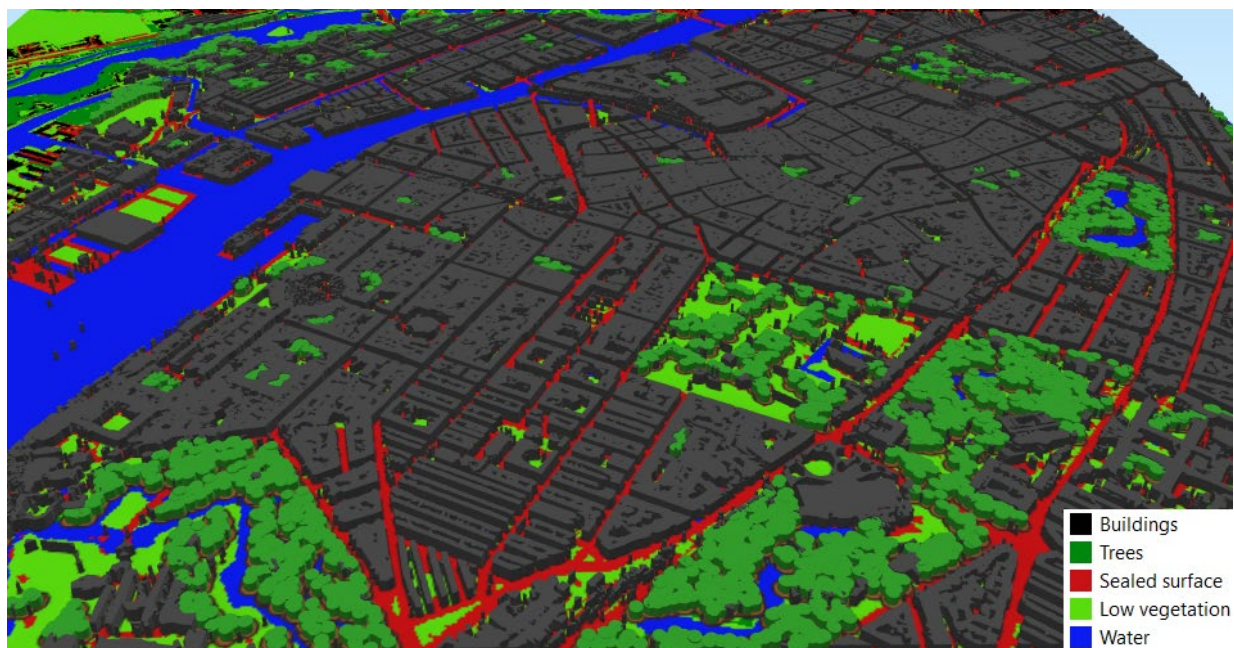
Figure 44. Detailed land cover input map for the city of Copenhagen. Buildings are assumed to have a height of 20m, and trees have a height of 15m.

When assessing WBGT values, it is best to focus on typical hot summer days, because it is during these type of days that people will suffer from heat stress issues. The CURE Thermal Comfort Application delivers WBGT maps for a selected hot summer day.

A complete overview of the whole modelling chain is shown in Figure 45.
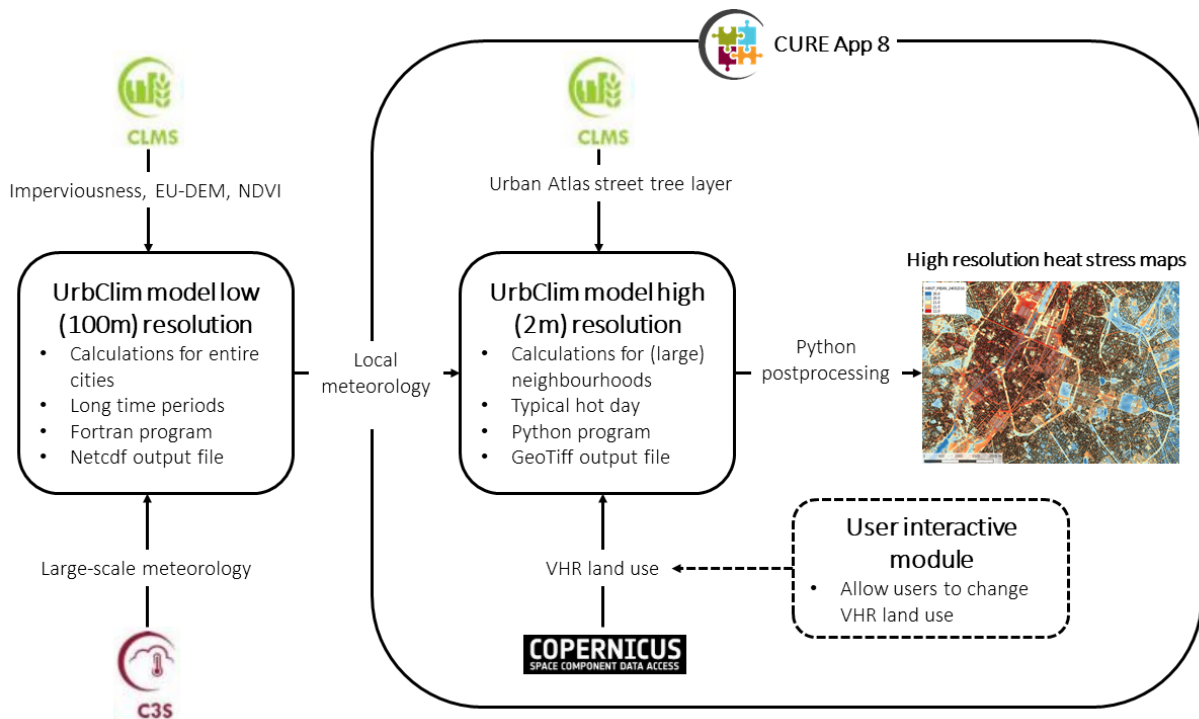
Figure 45. *Overview of the Thermal Comfort Application.*

The WBGT maps of this application will be made available to the users of the CURE system. This will allow stakeholders (e.g. urban planners and city administrations) to identify hotspots and give them insight in the local variation of heat stress with a high level of spatial detail. From these maps, overview statistics can be calculated (e.g. city quarter averages, area above/below defined threshold values). Furthermore, the intention is that the application will allow users to modify the input land cover map and upload different land use scenarios from which new WBGT maps will be calculated instantly. As a result, the users will be able to assess the effectiveness of e.g. green-blue adaptation measures and justify their adaptation strategies, in the sense of providing evidence of their climate-friendliness. Also, they will be enabled to assess the impact of specific intentions of developers on the local thermal comfort conditions in the city, which can help them to decide which intentions should be realized and which not, from an environmental point of view.

9.2   Sample results for the front-runner and follower cities

The CURE Urban Thermal Comfort Application delivers Wet Bulb Globe Temperature maps (Geotiff format) for a typical hot summer day for 4 European cities: Copenhagen, Ostrava, San Sebastian and Sofia. Both daily maximum and daily mean WBGT maps are calculated from the hourly model output. When assessing the WBGT values, it is good to keep in mind that the values are typically a few degrees lower than regular air temperature values, and a difference of a few degrees can already have a strong effect on human thermal comfort.

Daily maximum WBGT maps focus on the hottest hours of the day, when shading is crucial to lower the local heat stress. The variability in the temperatures is typically at least 3°C, up to 6°C (e.g. in San Sebastian) if there are large height differences. From the example maps shown below it is clear that forested areas are the coolest locations in cities, as the trees provide shade and cool the air through evapotranspiration. Water areas can also provide some cooling during the hottest hours of the day. Open areas without shade from trees or buildings are the hottest locations. There is typically not much difference in the maximum temperatures between the city center and the surrounding areas as the urban heat island effect is usually low during daytime.

The daily mean WBGT maps show a time-average of the heat stress situation and take also the nighttime into account, when the urban heat island is at its strongest. The variability in the temperatures is a bit lower than for the maximum temperatures, and is typically around 2 to 4°C. Again, forested areas are the coolest locations on the map, and the bigger they are, the larger the cooling effect. Water areas show less cooling in these maps, as they often keep a high temperature during the night, aggravating the urban heat island problem. The sealed areas in the cities are the hottest locations. The urban heat island effect is more visible in these maps.

9.2.1 Copenhagen – 30 June 2019
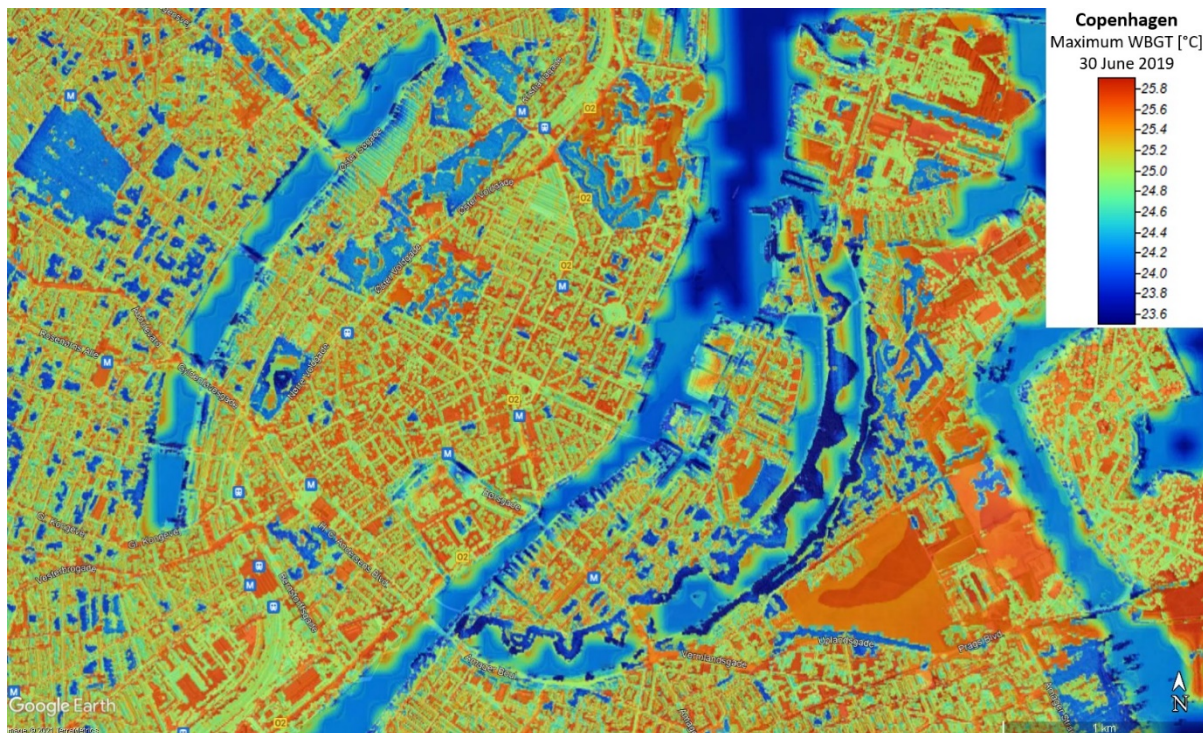
Figure 46. *Daily maximum Wet Bulb Globe Temperature in Copenhagen (Denmark) for 30 June 2019.*
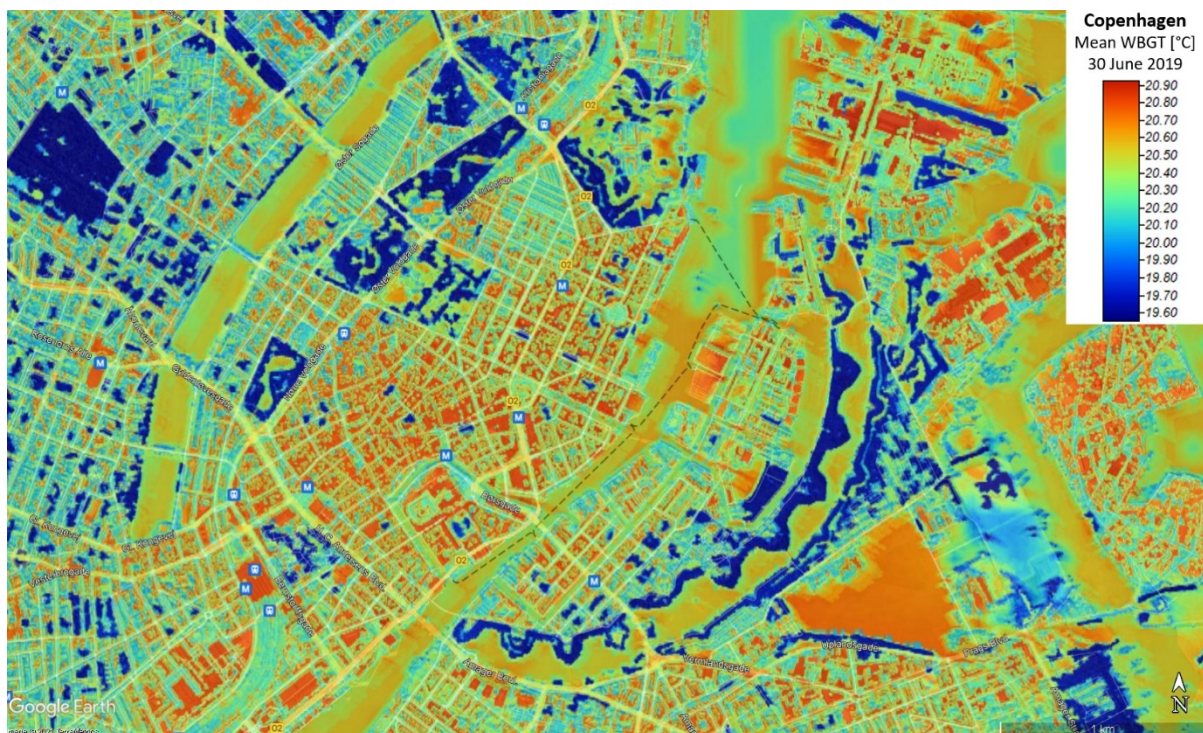
Figure 47. *Daily mean Wet Bulb Globe Temperature in Copenhagen (Denmark) for 30 June 2019.*

9.2.2   Sofia – 2 July 2019

Figure 48. *Daily maximum Wet Bulb Globe Temperature in Sofia (Bulgaria) for 2 July 2019.*
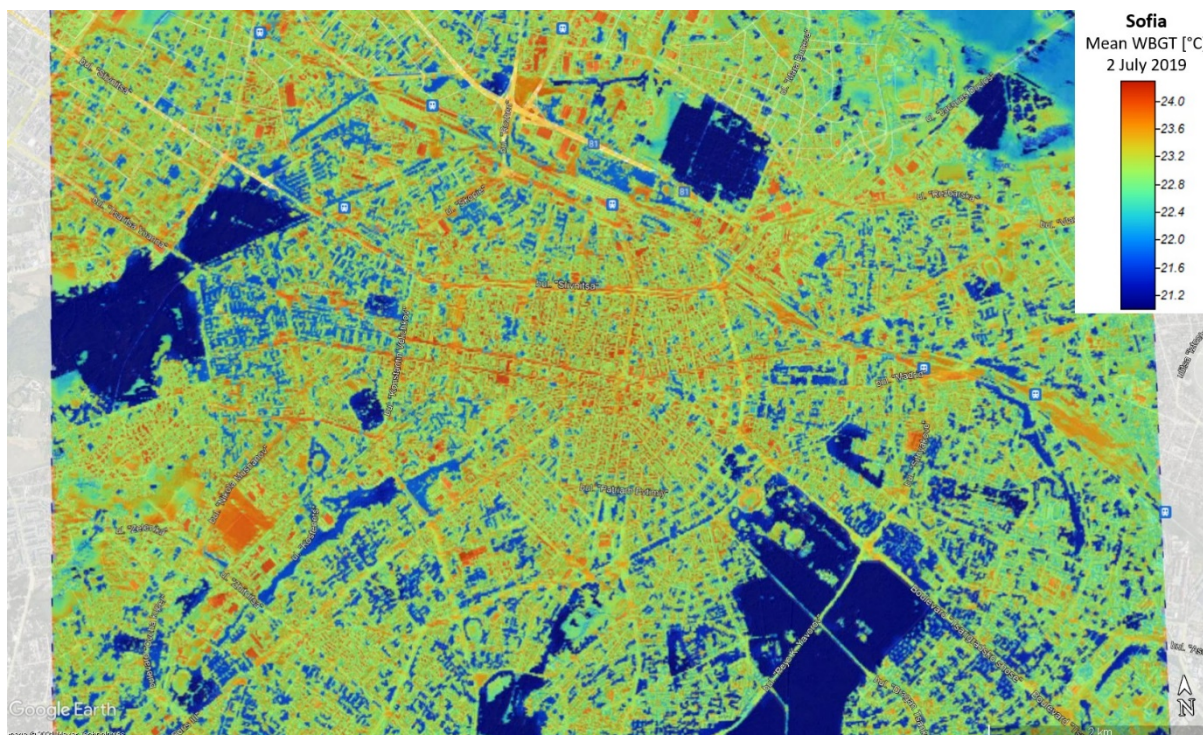
Figure 49. *Daily mean Wet Bulb Globe Temperature in Sofia (Bulgaria) for 2 July 2019.*

9.2.3   Ostrava – 30 June 2019
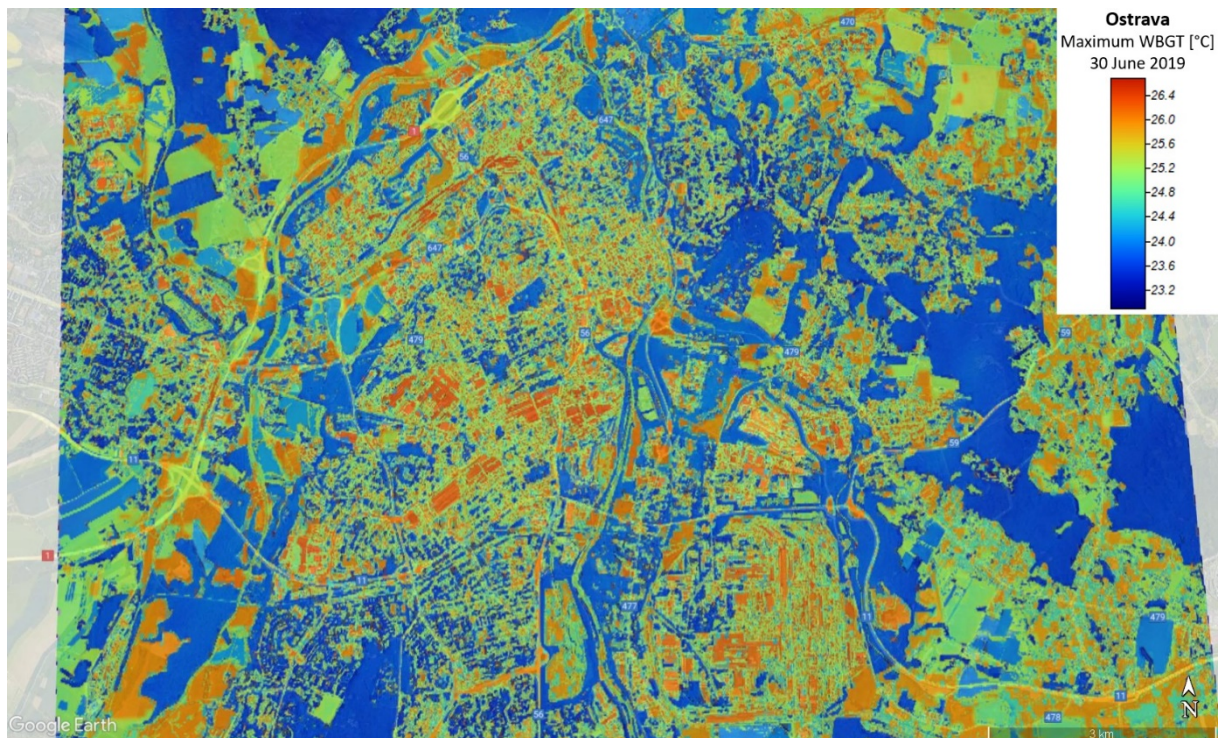
Figure 50. Daily maximum Wet Bulb Globe Temperature in Ostrava (Czech Republic) for 30 June 2019.
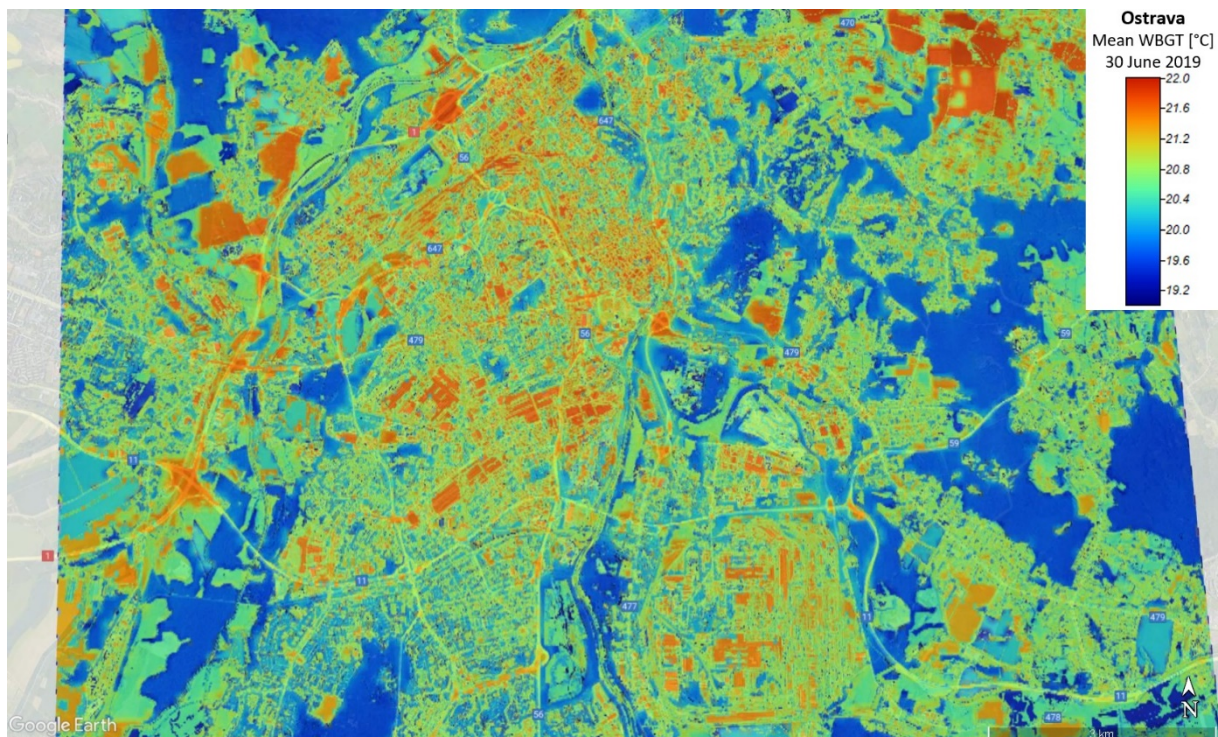
Figure 51. Daily mean Wet Bulb Globe Temperature in Ostrava (Czech Republic) for 30 June 2019.

9.2.4   San Sebastian – 23 July 2019
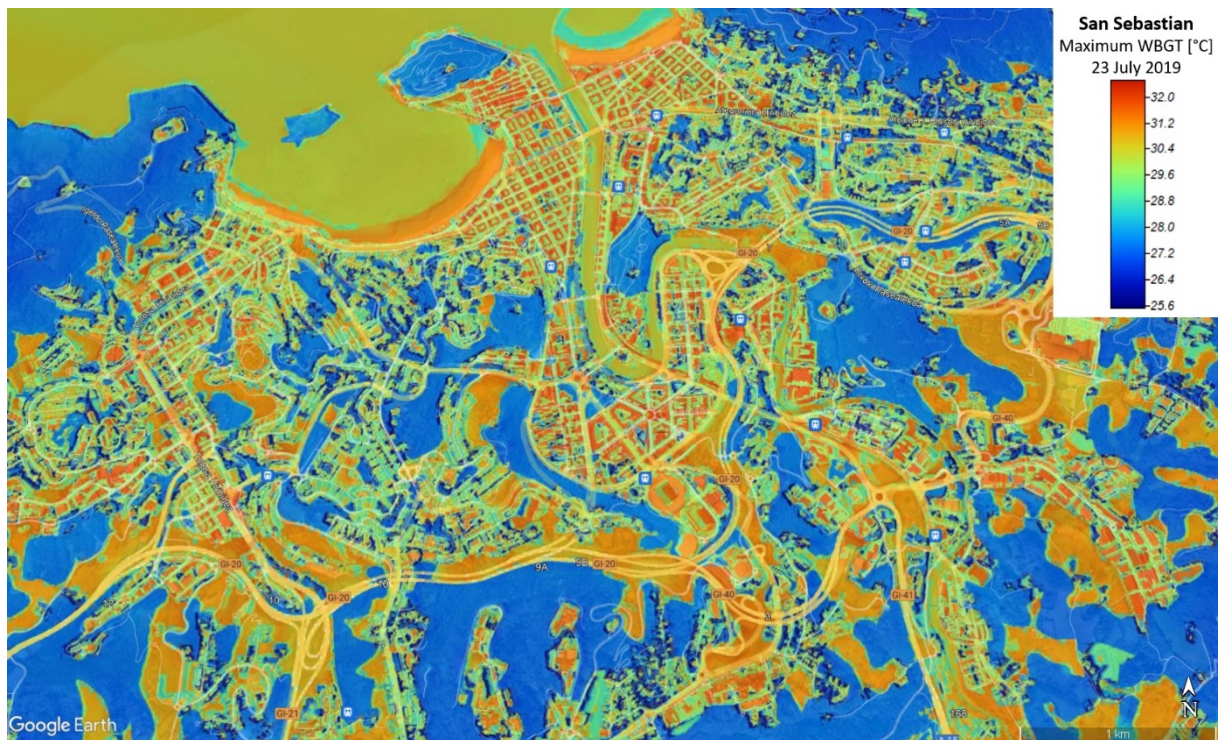
Figure 52. *Daily maximum Wet Bulb Globe Temperature in San Sebastian (Spain) for 23 July 2019.*
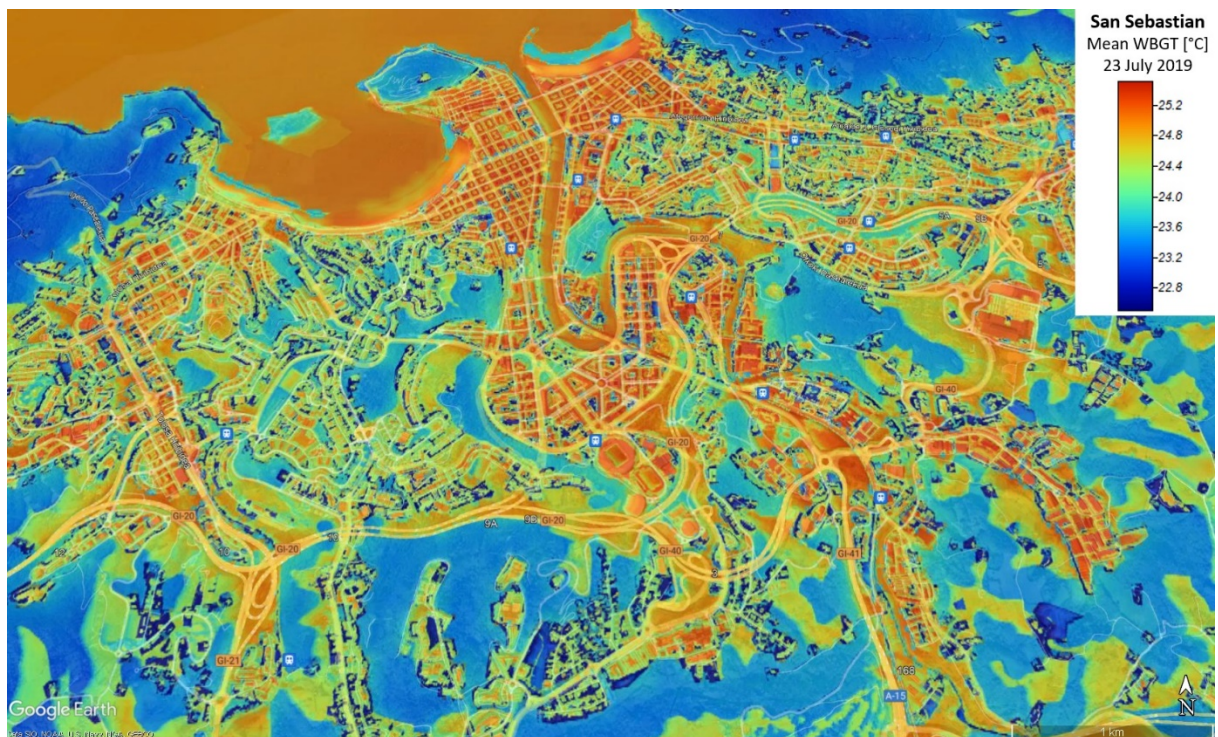
Figure 53. *Daily mean Wet Bulb Globe Temperature in San Sebastian (Spain) for 23 July 2019.*

10 AP09 Urban Heat Storage Monitoring

10.1 Final Input Data & Methodology

10.1.1 Data

AP09 is implemented for Heraklion (front-runner) and Basel (follower) cities. Table 11 lists the data that are used for the AP09. AP09 is using data from three Copernicus Services (CLMS,CAMS and C3S), very high resolution optical third-party data from the Copernicus Contributing missions Data Warehouse (Copernicus, 2020) and data products from AP01.

Table 11. Summary of data used for AP09.

Data Source	Description of the Product
CAMS	Clear-sky surface solar irradiation
C3S	ERA5 Air Temperature
CLMS	Urban Atlas
CLMS	Urban Atlas: Building Heights
CLMS	EU-DEM
CLMS	High Resolution Vegetation Phenology and Productivity (Under Development)
Copernicus Satellite	Sentinel-2, Level-2A Bottom Of Atmosphere (BOA) reflectance images
Third-party	Baseline Land Cover from VHR (from the DWH)

10.1.2 Methodology

Heat storage flux (ΔQs) is the net flow of heat stored in urban canopy and represents all the mechanisms of energy storage within the volume, i.e., the air, on trees, in buildings constructed in the ground, etc. (Offerle et al. 2005). An updated version of the Objective Hysteresis Model (OHM) (Lindberg et al. 2018) is used in CURE to estimate heat storage at local scale (100 m). The method is adapted to Copernicus Core Services. The hysteresis effect on energy flux storage indicates how quickly the urban surface responds to the input of energy and its association with the diurnal evolution of the boundary layer, varying according to latitude, cloud cover, soil characteristics, wetness and vegetation cover. OHM is based on the following expression (Grimmond and Oke, 1999):

$$\Delta Q_S = \sum_i^N (f_i a_{1i}) Q^* + \sum_i^N (f_i a_{2i}) \frac{\partial Q^*}{\partial t} + \sum_i^N (f_i a_{3i})$$

where Q^* is the net all-wave radiation, $\partial Q^*/\partial t$ is the time rate of change for net all-wave radiation at the surface and f_i the fraction of each of the N surface components within each grid cell and a_1, a_2 and a_3 are coefficients associated to response of the surface cover due the energy input. Coefficient a_1 indicates the intensity of the relationship between the stored

energy flux and the net all-wave radiation. Coefficient a_2 quantifies the magnitude of hysteresis, indicating the direction and degree of the phase relationship between stored energy flux and net all-wave radiation. Coefficient a_3 is an intercept term and indicates the extent to which a negative storage energy flux occurs before the net all-wave radiation starts to become negative. The methodology followed in CURE is outlined in Figure 54.

The surface cover fractions f_i are estimated as in AP01, using VHR baseline land cover corrected with Urban Atlas CLMS information and using Sentinel-2 imagery and CLMS imperviousness and vegetation dynamics layers for monitoring the dynamic surface cover fraction change.

Coefficients a_1, a_2 and a_3 are approximated from CLMS Urban Atlas and Building Height information (Grimmond and Oke, 1999; Ward et al., 2016). Table 12 lists the coefficients, as these were determined for the city of Heraklion.

Table 12. Coefficients used for the case study of Heraklion, Greece (buildings class: Yoshida et al., 1990, 1991; remaining: Ward et al., 2016).

Class	a_1	a_2	a_3
Water	0.5	0.21	-39.1
Vegetation	0.336	0.313	-31.4
Bare soil	0.355	0.335	-35.275
Asphalt	0.64	0.32	-43.6
Buildings	0.71	0.04	-39.7

Q^* (W m^{-2}) is estimated using the Net All-Wave Radiation Parameterization (NARP) (Offerle et al., 2003):

$$Q^* = K_\downarrow - K_\uparrow + L_\downarrow - L_\uparrow$$

where $K_\downarrow$ is the incoming shortwave radiation (W m^{-2}), $K_\uparrow$ is the outgoing shortwave radiation (W m^{-2}), $L_\downarrow$ is the incoming longwave radiation (W m^{-2}) and $L_\uparrow$ is outgoing longwave radiation (W m^{-2}).

$K_\downarrow$ is given from the CAMS clear-sky surface solar irradiation product.

$K_\uparrow$ is estimated as:

$$K_\uparrow = a\, K_\downarrow$$

where a is the albedo provided in CURE from the blue-sky albedo product of rslab (Chrysoulakis et al., 2018).

$L_\downarrow$ is estimated as:

$$L_\downarrow = \varepsilon_a \sigma T_\alpha^4$$

where ε_a is the broadband atmospheric emissivity, σ is the Stefan's constant and T_α is the bulk atmospheric temperature (K) approximated by the air-temperature near the surface (2 m) as derived from the C3S ERA5 Air Temperature (2 m) product.

ε_a is estimated as:

$$\varepsilon_a = 1 - (1 + w)e^{-\sqrt{1.2+3w}}$$

where w is the precipitable water content (g cm^{-2}), derived from C3S ERA5.

$L_\uparrow$ is estimated as:

$$L_\uparrow = \varepsilon_s \sigma T_s^4 + 0.08K_\downarrow(1 - \alpha) + (1 - \varepsilon_s)L_\downarrow$$

where ε_s is the surface emissivity and T_s is the LST, as derived from AP01.

The coefficients a_1, a_2 and a_3 are determined from CLMS, based on the land cover as explained earlier. The parameter $\vartheta Q^*/\vartheta t$ is calculated by assuming the Q* difference between two times instances t_1 and t_2, i.e. $\partial Q^*/\partial t = (Q_2^* - Q_1^*)/(t_2 - t_1)$, with time difference smaller than an hour. To achieve this, LST from more sources was necessary. Therefore, thermal images from MODIS (Moderate Resolution Imaging Spectroradiometer) were used in AP01 to produce LST maps with minor time difference to the Sentinel-3 ones.
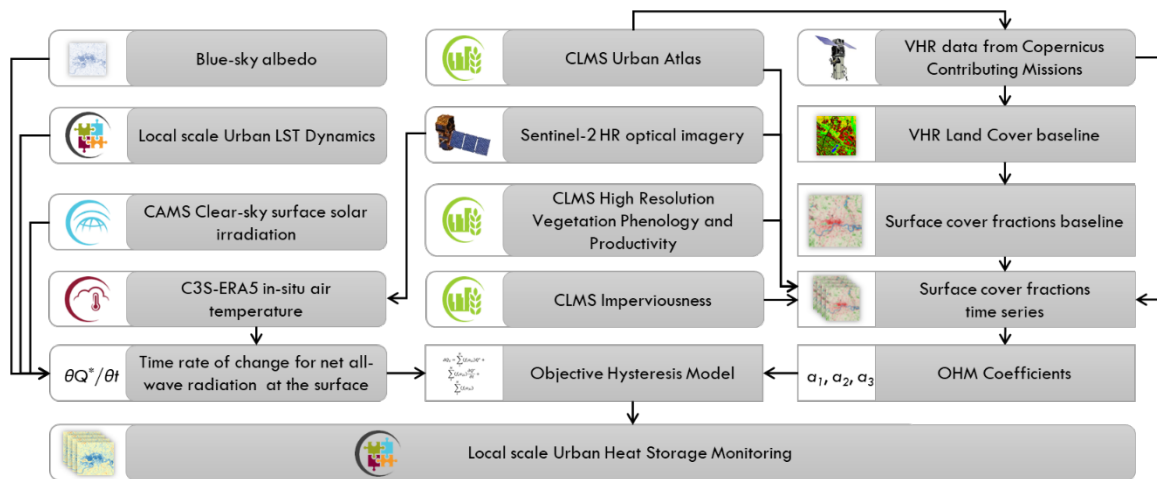
Figure 54. *Methodology for the estimation of Urban Heat Storage at local scale.*

10.2 Sample results for the front-runner and follower cities

Figure 55 shows a sample result of AP09 for the front-runner city of Heraklion, Greece. A daytime and a nighttime map of heat storage flux ΔQS in W m^{-2} are displayed. The sea is masked out of the computations and therefore the area appears white. Missing values (also in white), i.e. in the coastline and some inside the images, are due to the cloud cover mask of Sentinel-3 and/or MODIS.

Resulting maps indicate high amount of energy stored inside the urban area of Heraklion during daytime. As expected, the energy from solar radiation during noon is trapped inside the city and it is stored particularly in buildings with an increased pace ranging from 350 to 500 W m^{-2}. While in the surrounding rural areas, energy is stored in a much lower pace (lower than 200 W m^{-2}). The opposite phenomenon is evident during nighttime in this example. This nighttime map corresponds to almost midnight, with sunset around 21.00 local time. The city has released most of the available energy stored during daytime and it is currently releasing in a lower pace (~30-50 W m^{-2}).
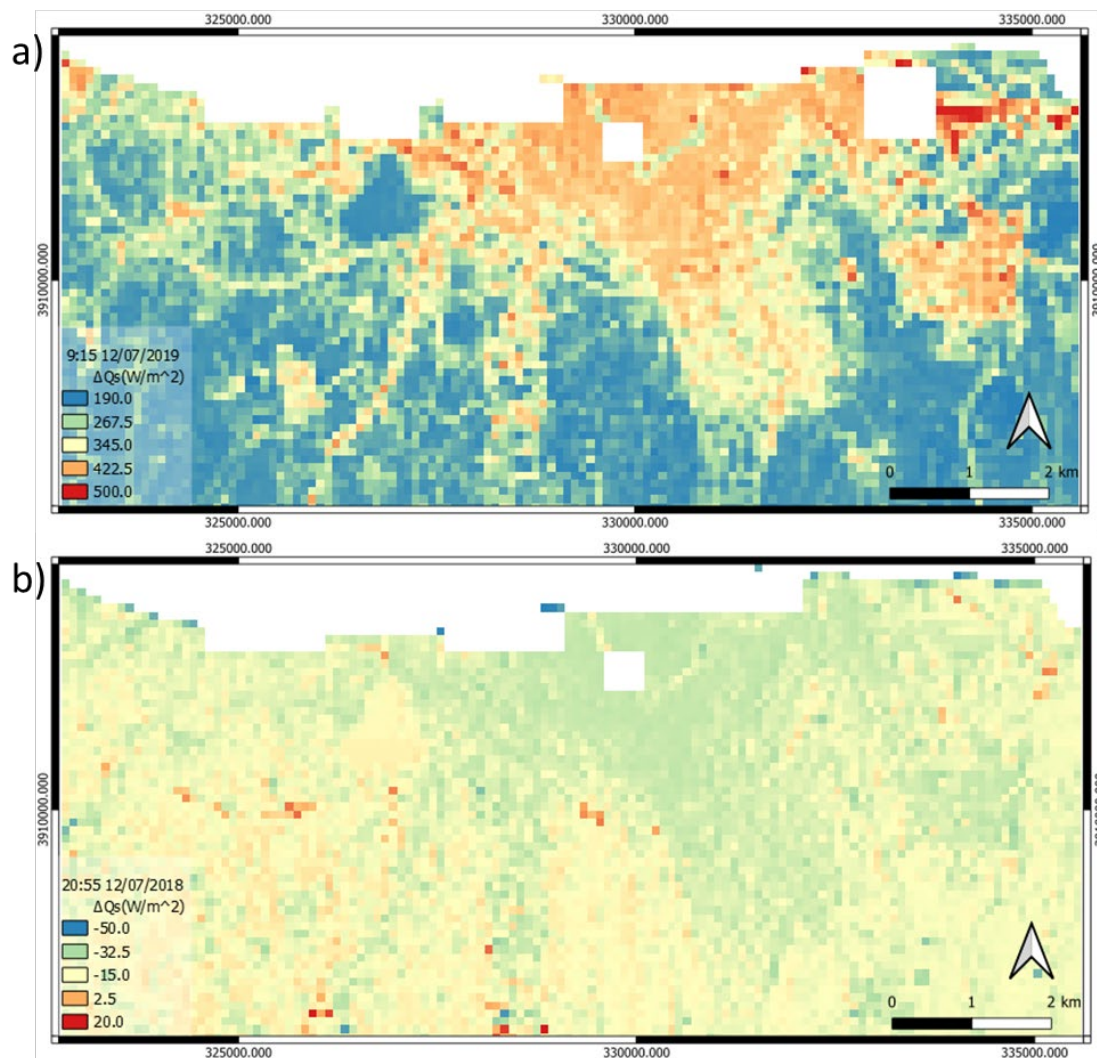
Figure 55. *Sample AP09 product: Spatial distribution of the heat storage flux ΔQs [W m^{-2}] for Heraklion a) daytime on 21 July 2019, 12.15 local time and b) nighttime on 12 July 2018, 23.55 local time.*

11 AP10 NATURE BASED SOLUTIONS

11.1 Final Input Data & Methodology

In urban areas, contribution of green roofs is a valid alternative to increase the green area, especially where available land for greening is limited. The methodology proposed aims to estimate the potential for green coverage at rooftop level by identifying suitable locations for green roof deployment and supporting decision-making towards broader sustainable urban development.

With the objective of comparing the results of the analysis and their accuracy, three inputs for object detection will be considered:

- LiDAR: From LIDAR data digital surface model is derived, which includes elevation data of the urban environment, including the elevations of urban elements such as buildings, vegetation or roads, among others. The number of points and point density improves data accuracy, which is crucial.
- Stereo Imagery DSM: Out of the granted VHR WorldView-1 and WorldView-3 images acquired at different time steps with different viewing angles, we generate a sub-meter (i.e., 50 cm) spatial resolution DSM. In particular, the DLR "Catena" operational infrastructure is used. Here, the standard chain generates orthorectified images using a worldwide reference image database. For this task, ground control points are automatically extracted from the satellite and reference images, which are used to correct attitude and ephemeris data. Next, the original satellite image is orthorectified using a high-resolution digital elevation model. Finally, automatic atmospheric correction is performed and concurrently the DSM is generated.
- Euro-Maps 3D DSM: Euro-Maps 3D products developed by GAF are DEMs semi-automatically derived from 2.5 m in-flight stereo data provided by IRS-P5 Cartosat-1 and. Among these, the Euro-Maps 3D DSM layer is a homogeneous 5m spaced DSM product including detailed flanking information consisting of several pixel-based quality and traceability layers. A sophisticated and tailored algorithm based on semi-global matching is applied and the reliability of the information is increased by using multiple overlapping stereo pairs. Since 2020, Euro-Maps 3D products are available from ESA as Third Party Mission data for on demand ordering upon submission of a Project Proposal subject to evaluation and acceptance. In this regard, the CORE consortium is going to submit a dedicated proposal in early 2021.

Buildings outlines are derived from cadastral map in form of vector file.

The methodological process for the calculation as described below:

Identification of the maximum green roof potential

As flat or quasi flat roofs are the ones more suitable to host a green cover, slope computation is performed (step 1). For each unit (building), an analysis of the slope is performed on the basis of each DSM by measuring the actual slope at each point/pixel of the roof. The slope map of the building is analyzed using a statistical algorithm that gives us the estimation of the real slope and the flat area available. Buildings with a suitable flat surface are labeled as flat roof by noting their flat zone percentage. The threshold for the slope computation is adjusted on a case by case, considering local regulations and policies. Consequently, for each building, the percentage of flat surface is calculated (step 2), considering roofs whose flat surface percentage is greater than 10% if their size is lower than 100 m² or greater than 5% if their size is greater than 100 m², which are those considered as suitable for hosting a green roof (Marconcini et al. 2016). This process allows for determining the maximum green roof potential (step 3) of each building, which is the maximum area that is suitable to host a green roof.

Prioritization of areas with highest potential/benefit

Benefits of green roofs are larger if these solutions are installed in areas characterized by low NDVI, impervious surface and high LST (step 4), contributing also to reduce the Urban Heat Island effect. All these characteristics determine the priority of the area where the buildings are located.

Identification of buildings with highest potential

The building outlines is read from a vector file where the 2D geometry is defined. The data model needs to be completed with all the available semantic information (step 5). Cadastral information will be used to include the year of construction. In addition, information on flat surface percentage of the building is assigned from the calculated flat surface map and maximum green roof potential (step 3) is calculated.

Prioritization of green roofs

Finally, to prioritize the buildings for implementing green roofs, the area priority and the building priority is combined (step 6). The prioritization of areas is based on LST, NDVI and Imperviousness (step 3), and the prioritization of buildings is based on year of construction and maximum green roof potential. These prioritizations are calculated through a weighted combination that might be specified by the user depending on the city characteristics.

The following graph shows the overall approach and methodological steps for the development of the NBS App:
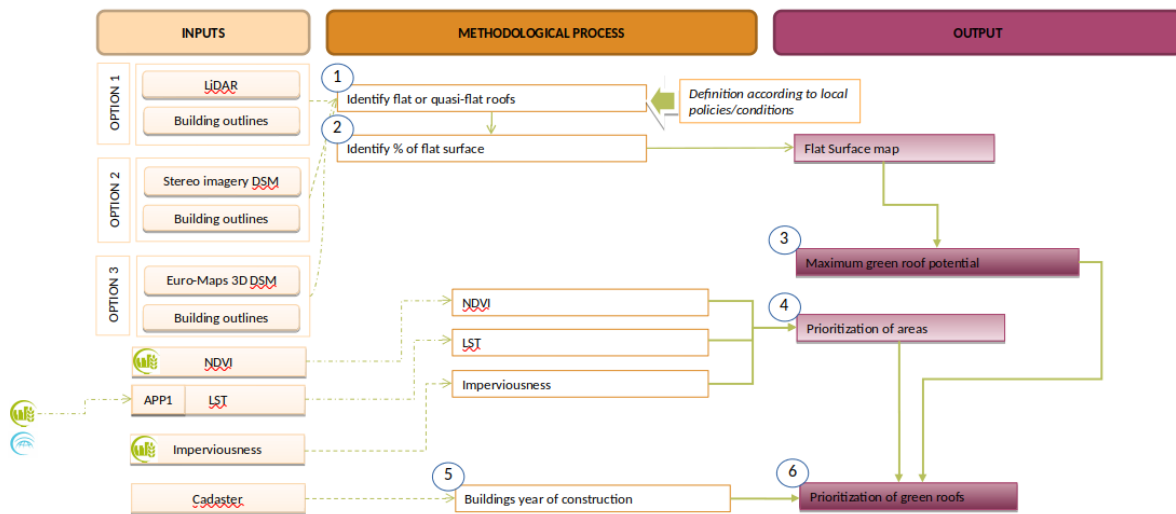
Figure 56. *Overview of the Nature Based Solution App*

Table 13. *Overview of the input datasets for the prioritization of green roofs*

INPUT	Copernicus service	Dataset	Usage
LIDAR (option 1)			Identify flat surface of the roofs
Stereo imagery DSM (option 2)			Identify flat surface of the roofs
Euro-Maps 3D DSM (option 3)			Identify flat surface of the roofs
Building outlines			Identify flat surface of the roofs
NDVI	CLMS	NDVI	Identify already existing green roofs (with vegetation >10%)
LST	CLMS, CAMS	LST (APP1)	Prioritize intervention areas
Imperviousness	CLMS	Imperviousness	Prioritize intervention areas
Cadaster			Inclusion of cadastral semantic information (year of construction)

11.2 Sample results for the front-runner and follower cities

11.2.1 Sofia
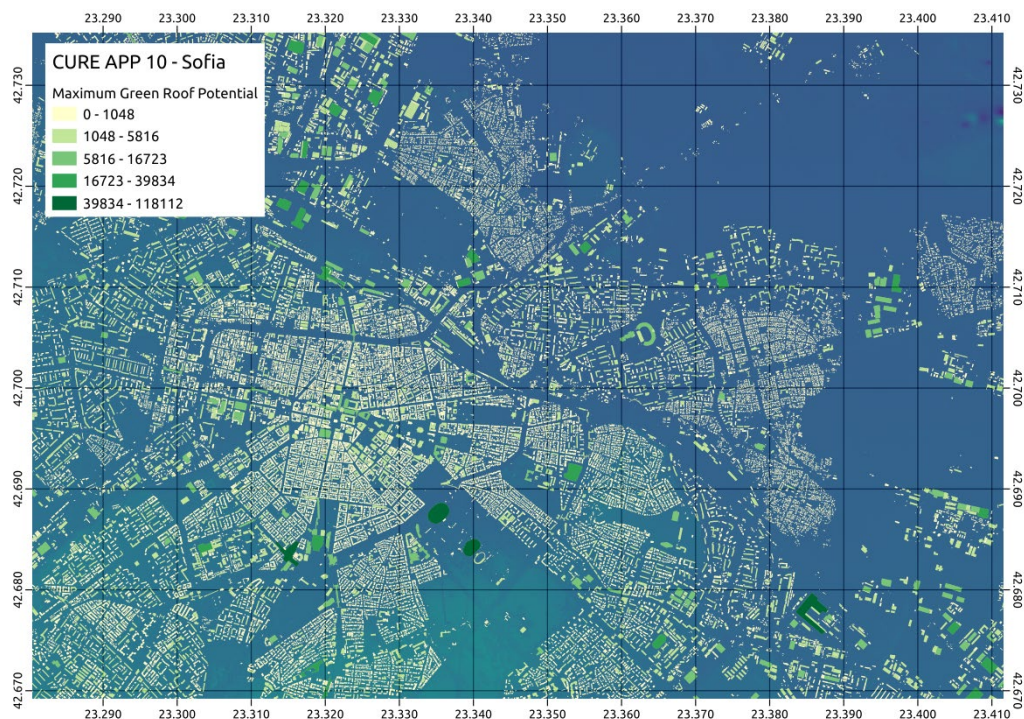
Figure 57. Maximum green roof potential in Sofia.
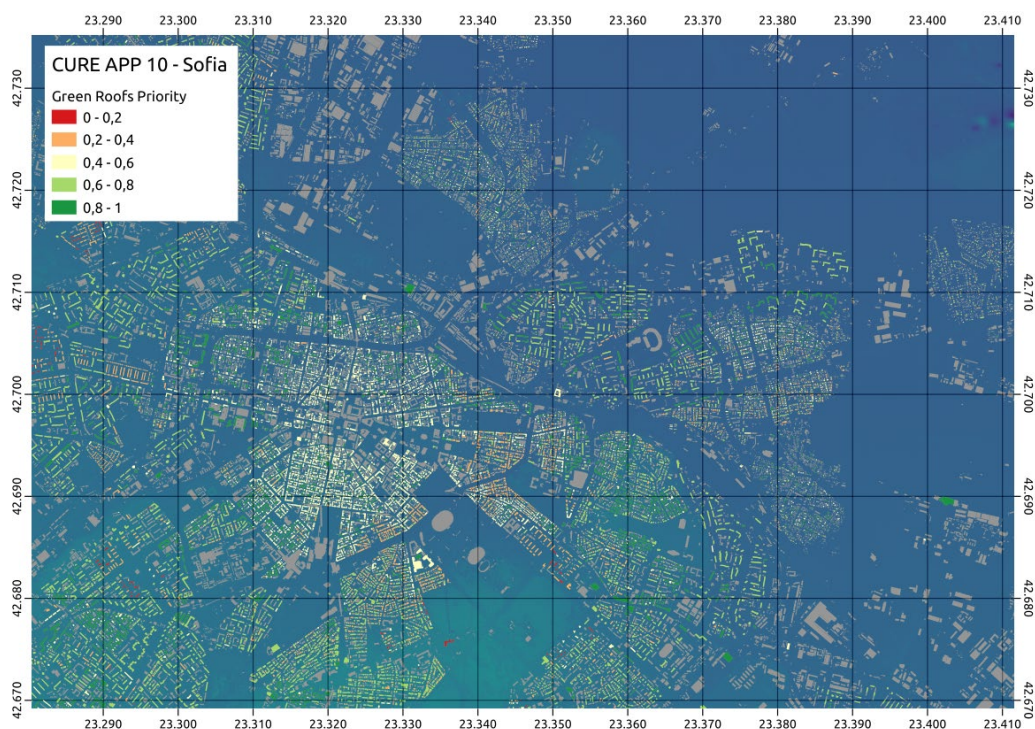
Figure 58. Green roofs priority in Sofia.

11.2.2 San Sebastian
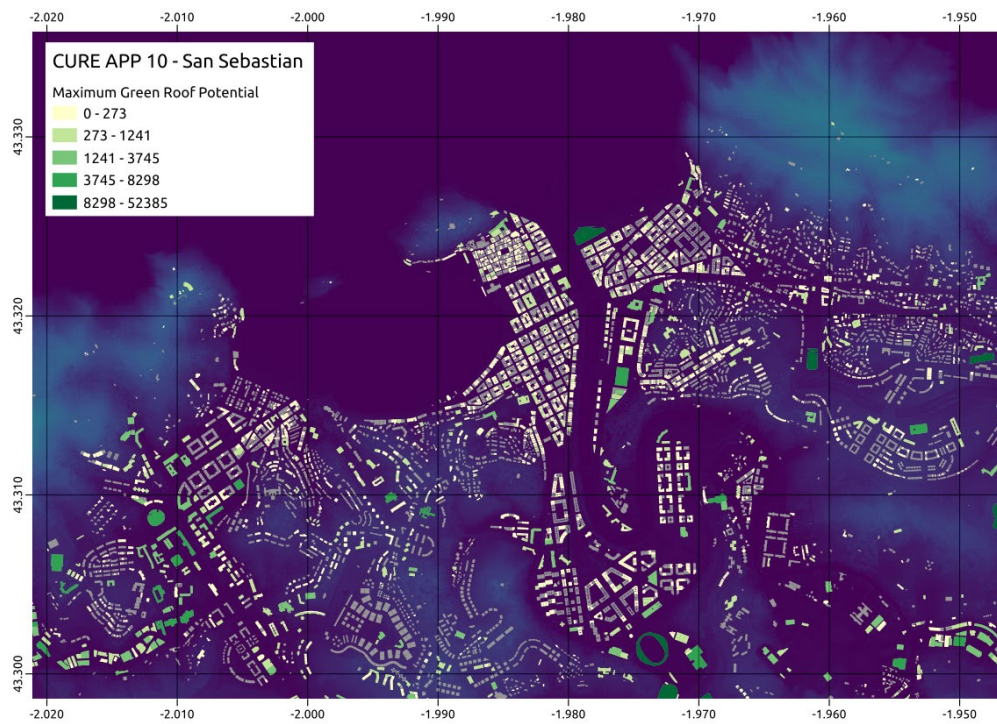
Figure 59. *Maximum green roof potential in San Sebastian.*
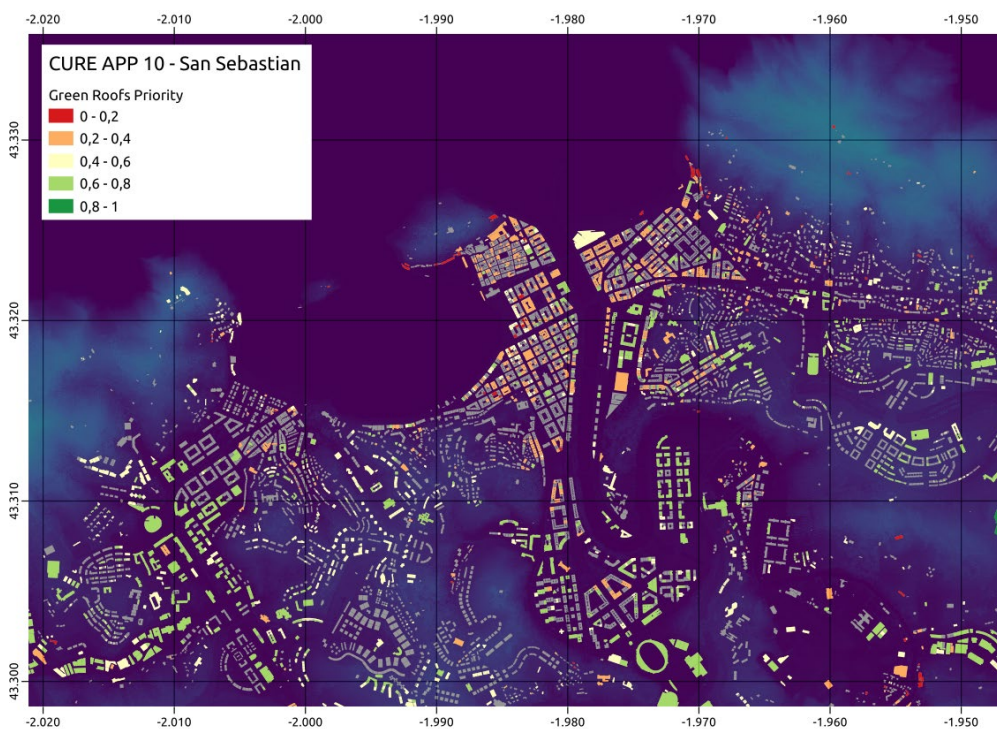
Figure 60. *Green roofs priority in San Sebastian.*

12 AP11 HEALTH IMPACTS

12.1 Final Input Data & Methodology

12.1.1 The EVA model

The integrated model system is based on the impact-pathway chain and is used for assessment of health impacts from air pollution, including both health effects and related external costs (sometimes also referred to as "indirect costs") which can be attributed to air pollution exposure.
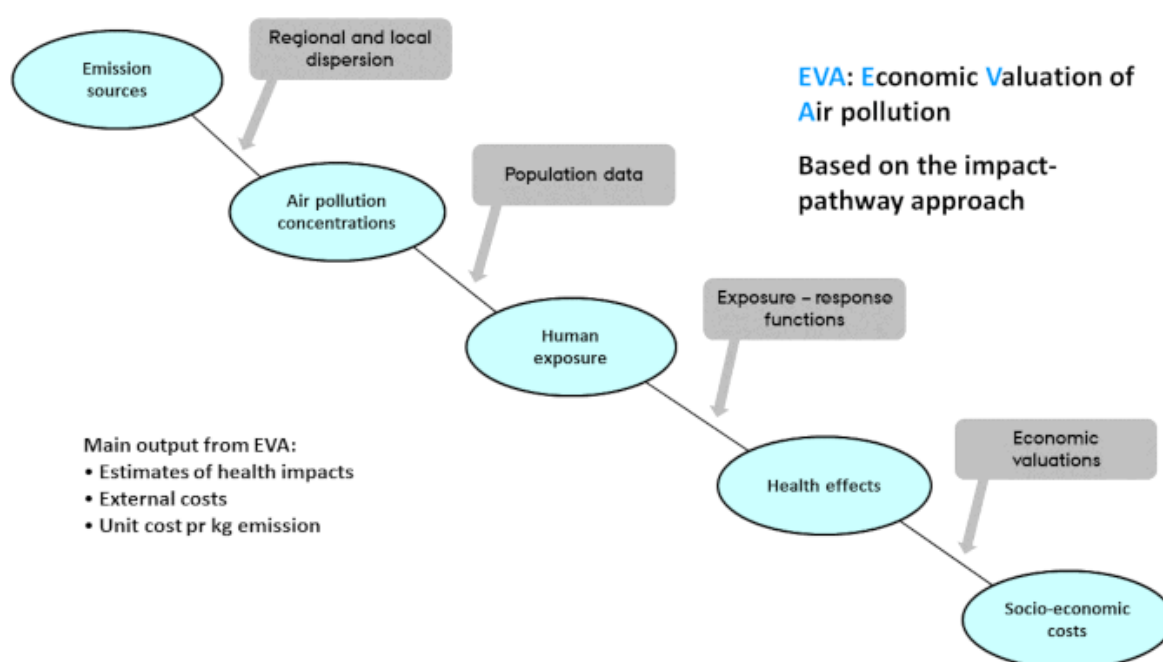
Figure 61. *A schematic diagram of the impact-pathway methodology. The site-specific emissions result (via atmospheric transport and chemistry) in a concentration distribution, which together with detailed population data, can be used to estimate the population-level exposure. Using exposure-response functions and economic valuations, the exposure can be transformed into impacts on human health and related external costs.*

Chemical components important for health impacts and included in the EVA system are: nitrogen dioxide (NO2), sulphur dioxide (SO2), ozone (O3) and particulate matter (PM2.5), where the individual constituents of PM2.5 are: mineral dust, black carbon (BC), organic matter (OM), secondary inorganic aerosols (SIA – i.e. nitrate, sulphate and ammonia), secondary organic aerosols (SOA) and sea salt.

The EVA model is coupled to the air pollution models DEHM (Danish Eulerian Hemispheric Model) and UBM (Urban Background Model) for regional-scale and local-scale health impact assessments, respectively. EVA includes gridded population data, exposure-response functions for health impacts in terms of morbidity and mortality, and economic valuation of the health impacts from air pollution.

The EVA system uses comprehensive and thoroughly tested chemistry-transport models when calculating air pollution levels in general as well as scenarios describing how specific changes in emissions of pollutants to the air affect air pollution levels at regional and local scale.

Modelling of air quality is based on the regional air pollution model DEHM and the urban background model UBM resulting in calculations performed on a 1 km x 1 km grid resolution. Urban background concentrations are the general air pollution in the city and reflect the concentrations in a park, a backyard or the roof of buildings. Urban background concentrations differ from street concentrations, which represent the concentrations in the height of 2 m at the facade of buildings. Street concentrations are calculated using air quality model OSPM.

To estimate the effect of a specific emission source or emission sector, emission inventories for the specific sources are implemented in DEHM, together with all other relevant anthropogenic and natural emission sources, see Table 14 for description of emission sources.

Table 14. Definition of the SNAP categories and a short description of the emissions of interest.

Region	SNAP	Emission scenario (or the "tag")
	1	Combustion in energy and transformation industries
	2	Non-industrial combustion plants, including private wood combustion
	3	Combustion in manufacturing industry
	4	Production processes
	5	Extraction and distribution of fossil fuels and geothermal energy
EU/DK	6	Solvents and other product use
	7	Road transport
	8	Other mobile sources and machinery (excl. international ship traffic)
	9	Waste treatment and disposal
	10	Agriculture
	Sum 1–10	Sum of the above 10 SNAP categories
	All	All anthropogenic emissions (SNAP 1–SNAP 10)

To calculate the impacts of the total air pollution levels or of emissions from a specific source or sector, concentrations and address-level population data are combined to estimate human exposure, and then the response is calculated using an exposure-response function (ERF) of the following form: $R = A \cdot C \cdot P$, where R is the response (e.g. in cases, days, or episodes), C the concentration (i.e. the total concentration or additional concentration resulting from emissions of a particular emission source), P the affected share of the population, and A is an empirically determined constant for the particular health outcome, typically obtained from published cohort studies, see Table 15 for exposure-response functions.

Table 15. *Example of health effects, exposure-response functions and economic valuation (applicable for Danish/European conditions) included in the EVA model system (note, prices are from 2006). (PM is particulate matter, including primary PM2.5, NO_3^- and SO_4^{2-}. YOLL is years of life lost. SOMO3 (Sum of Ozone Means Over 35 ppb) is the sum of means over 35 ppb for the daily maximum 8-hour values of ozone.*

Health effects (compounds)	Exposure-response coefficient (α)	Valuation, euros (2006 prices)
Morbidity		
Chronic bronchitis (PM)	8.2×10^{-5} cases/μgm^{-3} (adults)	52 962 per case
Restricted activity days (PM)	$= 8.4 \times 10^{-4}$ days/μg m^{-3} (adults) -3.46×10^{-5} days/μg m^{-3} (adults) -2.47×10^{-4} days/μg m^{-3} (adults > 65) -8.42×10^{-5} days/μg m^{-3} (adults)	131 per day
Congestive heart failure (PM) Congestive heart failure (CO)	3.09×10^{-5} cases/μg m^{-3} 5.64×10^{-7} cases/μg m^{-3}	16 409 per case
Lung cancer (PM)	1.26×10^{-5} cases/μg m^{-3}	21 152 per case
Hospital admissions		
Respiratory (PM) Respiratory (SO$_2$)	3.46×10^{-6} cases/μg m^{-3} 2.04×10^{-6} cases/μg m^{-3}	7931 per case
Cerebrovascular (PM)	8.42×10^{-6} cases/μg m^{-3}	10 047 per case
Asthma, children (7.6 % <16 yr)		
Bronchodilator use (PM)	1.29×10^{-1} cases/μg m^{-3}	23 per case
Cough (PM)	4.46×10^{-1} days/μg m^{-3}	59 per day
Lower respiratory symptoms (PM)	1.72×10^{-1} days/μg m^{-3}	16 per day
Asthma, adults (5.9 % >15 yr)		
Bronchodilator use (PM)	2.72×10^{-1} cases/μg m^{-3}	23 per case
Cough (PM)	2.8×10^{-1} days/μgm^{-3}	59 per day
Lower respiratory symptoms (PM)	1.01×10^{-1} days/μg m^{-3}	16 per day
Loss of IQ		
Lead (Pb) (<3 year)*	1.3 points/μg m^{-3}	24 967 per point
Mercury (Hg) (foetus)*	0.33 points/μg m^{-3}	24 967 per point
Mortality		
Acute mortality (SO$_2$) Acute mortality (O$_3$)	7.85×10^{-6} cases/μg m^{-3} 3.27×10^{-6}*SOMO35 cases/μg m^{-3}	2 111 888 per case
Chronic mortality, YOLL (PM) Infant mortality (PM)	1.138×10^{-3} YOLL/μg m^{-3} (>30 yr) 6.68×10^{-6} cases/μg m^{-3} (>9 months)	77 199 per YOLL 3 167 832 per case

EVA calculates and uses the annual mean concentrations of CO, SO2 and PM2.5, while for O3, it uses the SOMO35 metric that is defined as the yearly sum of the daily maximum of 8 h running average over 35 ppb, following WHO (2013) and EEA (2017).

In EVA, the number of lost life years for a Danish population cohort with normal age distribution, when applying the ERF of Pope et al. (2002) for all-cause mortality (relative risk, RR of 1.062 (1.040–1.083) on a 95 % confidence interval), and the latency period indicated, sums to 1138 years of life lost (YOLL) per 100.000 individuals for annual PM2.5 increase of 10 µg m−3 (Andersen et al., 2008). EVA uses a counterfactual PM2.5 concentration of 0 µgm−3 following the EEA methodology, meaning that the impacts have been estimated for the full range of modelled concentrations from 0 µg m−3 upwards.

For Copenhagen the results will be obtained through this method:

1. *Air Quality Assessment*

An air quality assessment is carried out that describes the spatial distribution of background concentrations with a resolution of 1 km x 1 km, as well as street concentrations at address level in the Capital Region. This description is based on data from a national data set, which is called Air Quality at Your Street (http://luftenpaadinvej.au.dk). For our second frontrunner city, Sofia, we will rely on a local air pollution data set. Furthermore, a summary of the results from the fixed measuring stations in the Capital Region is carried out and compared with EU limit values for air quality and WHO air quality guidelines.

   2. *Health impacts and related external costs*

Health effects and related external costs are calculated for the total air pollution in the Capital Region. The total air pollution includes all sources from the Capital Region, and all other sources in Denmark and abroad. This also describes how much of total air pollution originates from local sources and how much is from sources outside the Capital Region. Moreover, calculations are carried out for each type of emission source in the Capital Region to quantify the contribution of the different sources. In principle, the Capital Region is able to regulate these sources.

Then we add calculations on the health impacts and related external costs based on information about the sources of pollution and their location, the dispersion of air pollution as well as exposure of the population, the dose-response relationship between exposure and health effects, and the valuation of health effects, also referred to as external costs related to health effects from air pollution. The EVA system includes population data with a spatial resolution of 1 km x 1 km.

12.2 Sample results for the front-runner and follower cities

Application 11 models the health and economic costs of air pollution for the city of Copenhagen and Sofia (frontrunner cities). Here we use the air quality maps developed by VITO in Application 7 (Urban Air Quality) for Sofia, where they have mapped the yearly mean concentrations of Nitrogen dioxide and PM2.5 for the year of 2018 based on Copernicus data and also supplemented with local data. The air quality has furthermore been grouped according to sector contribution (road traffic, industry, power plants and residential heating). Using these results, stakeholders can identify key sectors for which measures are prioritized. The sector contribution also provides a rough estimate for the (theoretical) maximal pollution reduction due to local measures for the sector under consideration. The results for particulate matter for instance highlight the importance of the urban residential emissions at this specific location. Also, the urban traffic emissions contribute a significant fraction to the total concentrations, whereas the urban power plant and industrial emissions are responsible for only a negligible fraction of the total pollution. Approximately a third of the pollution at this specific location is emitted outside the domain, or by sectors that are not explicitly considered

in the modelling. The results for NO_2 can be interpreted in a similar way, indicating the importance of the traffic emissions at this specific location. This is then coupled to the Evaluation of Air Pollution Model, which models the effect of the air pollution on different health parameters, such as:

AD "Acute" premature deaths from short term exposure of O3 and PM25
CD "Chronic" premature deaths from long-term exposure to PM25
ADCD Sum of AD and CD
RHA Respiratory hospital admissions
CHA Cardiovascular hospital admission
COU_C Asthma symptoms/cough
CB Chronic Bronchitis
CB_C Chronic Bronchitis - Children
WLD Work loss days
RAD Restricted activity days
MRAD Minor Restricted activity days
LC Lung Cancer
IM Infant Mortality
PWM_PM25 Population weighted mean for PM25

Figure 62. Health parameters from the EVA model.

The results will be visualized in an online interface, where the economics health impact costs will also be shown, see draft of interface below. This shows results for Sofia, and will soon be populated by results from Copenhagen as well.
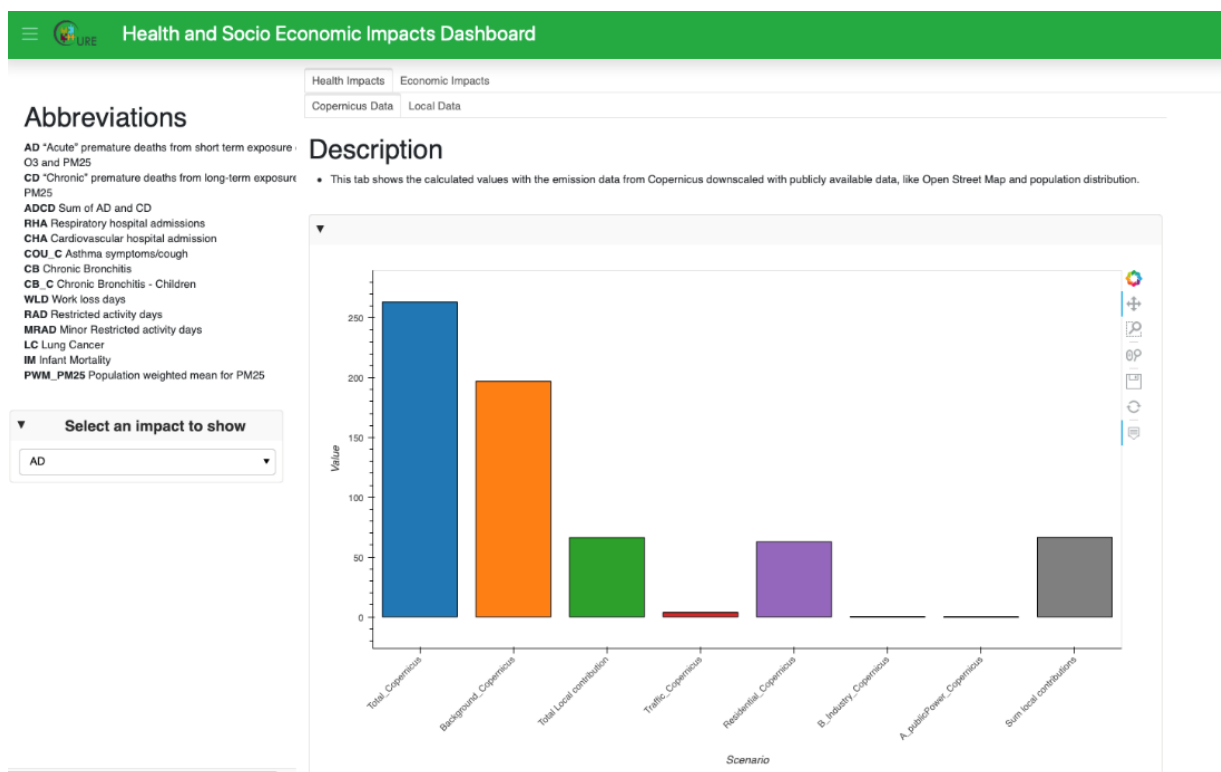
Figure 63. *Screenshot of draft interface of health and economic costs of air pollution for Sofia, Bulgaria (Frontrunner city). Shown here Acute Premature deaths (AD) based on Copernicus data (total, background, residential, traffic and industry, local).*

13 CONCLUSION

This is the second deliverable of WP3 of the CURE project, which focusses on the individual applications development. The CURE applications described in this deliverable form the basis for the development of an umbrella cross-cutting CURE service on urban resilience (WP4) and feed into the demonstration phase (WP5), in which users will give feedback on the resulting service through two demonstration workshops. After two iterations, a final set of cross-cutting applications related to urban resilience, with high automation and upscaling potential, is the expected outcome of WP3.

This deliverable explains how each application contributes to the concept of urban resilience and how different Copernicus Core Services products are used in order to build the cross-cutting service. The final methodological framework of each application is explained in detail, along with details on the necessary input information, arising from the interaction with WP2. Furthermore, a detailed description is given of the sample results for the front-runner and follower cities from each application, that are submitted in Deliverable 3.3.

REFERENCES

Andersen MS, Frohn LM, Nielsen JS, Nielsen M, Jensen SS, Christensen JH, Brandt J. A Non-linear Eulerian Approach for Assessment of Health-cost Externalities of Air Pollution. Proceedings of the European Association of Environmental and Resource Economists 16th Annual Conference; Gothenburg, Sweden. 25–28 June 2008; 2008. p. 23.

Aubinet, M., Vesala, T., Papale, D., 2012. Eddy Covariance – A Practical Guide to Measurement and Data Analysis. Springer Atmospheric Sciences

Berkowicz, R., Hertel, O., Larsen, S., Sørensen, N., Nielsen, M., 1997. Modelling traffic pollution in streets. URL: https://orbit.dtu.dk/files/128001317/Modelling_traffic_pollution_in_streets.pdf

Berkowicz, R., Ketzel. M., Lofstrom, P., Rordam, H., 2008. NO2 chemisty scheme in OSPM and other Danish models. URL: https://www2.dmu.dk/AtmosphericEnvironment/Docs/NO2scheme.pdf

Brutsaert, W., 1982. Evaporation into the Atmosphere. Springer Netherlands. ISBN: 978-90-481-8365-4

CAMS, 2019. The Copernicus Atmosphere Monitoring Service global and regional emissions (April 2019 version). https://doi.org/10.24380/d0bn-kx16

Christen, A., Coops, N.C., Crawford, B.R., Kellett, R., Liss, K.N., Olchovski, I., Tooke, T.R., Van Der Laan, M., Voogt, J.A., 2011. Validation of modeled carbon-dioxide emissions from an urban neighborhood with direct eddy-covariance measurements. *Atmos. Environ.* 45, 6057–6069. https://doi.org/10.1016/j.atmosenv.2011.07.040

Chrysoulakis, N., Grimmond, S., Feigenwinter, C., Lindberg, F., Gastellu-Etchegorry, J.-P., Marconcini, M., Mitraka, Z., Stagakis, S., Crawford, B., Olofson, F., Landier, L., Morrison, W., Parlow, E., 2018. Urban energy exchanges monitoring from space. *Sci. Rep.* 8, 11498. https://doi.org/10.1038/s41598-018-29873-x

Copernicus, 2020. Copernicus Space Component Data Access system (CSCDA) [WWW Document]. URL https://spacedata.copernicus.eu/ (accessed 12.9.20).

Crawford, B., Grimmond, C.S.B., Gabey, A., Marconcini, M., Ward, H.C., Kent, C.W., 2018. Variability of urban surface temperatures and implications for aerodynamic energy exchange in unstable conditions. *Q. J. Royal Meteorol. Soc.* 144, 1719-1741.

Cyrys J, Eeftens M, Heinrich J, Ampe C, Armengaud A, Beelen R, Bellander T, Beregszaszi T, Birk M, Cesaroni G, Cirach M, de Hoogh K, De Nazelle A, de Vocht F, Declercq C, Dedele A, Dimakopoulou K, Eriksen K, Galassi C, Graulevičiene R, Grivas G, Gruzieva O, Gustafsson

AH, Hoffmann B, Iakovides M, Ineichen A, Krämer U, Lanki T, Lozano P, Madsen C, Meliefste K, Modig L, Mölter A, Mosler G, Nieuwenhuijsen M, Nonnemacher M, Oldenwening M, Peters A, Pontet S, Probst-Hensch N, Quass U, Raaschou-Nielsen O, Ranzi A, Sugiri D, Stephanou EG, Taimisto P, Tsai MY, Vaskövi É, Villani S, Wang M, Brunekreef B, Hoek G (2012) Variation of NO2 and NOx concentrations between and within 36 European study areas: Results from the ESCAPE study. Atmos Environ 62:374–390 . doi: 10.1016/j.atmosenv.2012.07.080

De Ridder K., Lauwaet D., Maiheu B. 2015. UrbClim - a fast urban boundary layer climate model. Urban Climate 12, 21-48.

De Ridder K., Schayes G., 1997. The IAGL Land Surface Model, Journal of Applied Meteorology 36, 167–182.

Del Grosso, S.J., Parton, W.J., Derner, J.D., Chen, M., Tucker, C.J., 2018. Simple models to predict grassland ecosystem C exchange and actual evapotranspiration using NDVI and environmental variables. *Agric. Forest Meteorol.*, 249, 1-10.

EEA Report No 13/2017 Air Quality in Europe - 2017 report https://www.eea.europa.eu/publications/air-quality-in-europe-2017

EEA, 2019. Air quality in Europe 2019]. URL https://www.eea.europa.eu/publications/air-quality-in-europe-2019

ESA, 2019. Copernicus High Priority Candidate Missions [WWW Document]. URL https://www.esa.int/Applications/Observing_the_Earth/Copernicus/Candidate_missions (accessed 10.25.19).

European Ground Motion Service: Service Implementation Plan and Product Specification Document (2020), EEA https://land.copernicus.eu/user-corner/technical-library/egms-specification-and-implementation-plan

Feigenwinter, C., Vogt, R., Christen, A., 2012. Eddy Covariance Measurements Over Urban Areas, in: Eddy Covariance. Springer Netherlands, Dordrecht, pp. 377–397. https://doi.org/10.1007/978-94-007-2351-1_16

Foken, T., 2006. 50 Years of the Monin–Obukhov Similarity Theory. *Boundary-Layer Meteorol* 119, 431–447. https://doi.org/10.1007/s10546-006-9048-6

García-Díez M., Lauwaet D., Hooyberghs H., Ballester J., De Ridder K., Rodó X., 2016. Advantages of using a fast urban boundary layer model as compared to a full mesoscale model to simulate the urban heat island of Barcelona. Geoscientific Model Development 9, 4439–4450.

Grimmond, C.S.B., Oke, T.R., 1999. Heat Storage in Urban Areas: Local-Scale Observations and Evaluation of a Simple Model. J. Appl. Meteorol. 38, 922–940. https://doi.org/10.1175/1520-0450(1999)038<0922:hsiual>2.0.co;2

Hlavacova, I., Halounova, L., Stanislav, P.: Sentinel-1 INSAR processing of corner reflector information in the northern-bohemian coal basin. The International Archives of the Photogrammetry, Remote Sensing and Spatial Information Sciences, Volume XLI-B7, 2016 XXIII ISPRS Congress, 12–19 July 2016, Prague, Czech Republic.

Hooyberhs H, De Craemer S, Lefebvre W, Vranckx S, Maiheu B, Trimpeneers Em Vanpoucke C, Janssen S, Meysman F, Fierens F. 2020. Validation and optimization of the ATMO-Street model chain by means of a large-scale citizen-science dataset. In review

ISO (1989), Hot Environments - Estimation of the heat stress on working man, based on the WBGT-index (wet bulb globe temperature). ISO Standard 7243. Geneva: International Standards Organization.

Jensen, S.S., Ketzel, M., Becker, T., Christensen, J., Brandt, J., Plejdrup, M., Winther, M., Nielsen, O.K., Hertel, O., Ellermann, T., 2017. High resolution multi-scale air quality modelling for all streets in Denmark. Transp. Res. Part D Transp. Environ. 52, 322–339. https://doi.org/10.1016/j.trd.2017.02.019

Kanda, M., Inagaki, A., Miyamoto, T., Gryschka, M., Raasch, S., 2013. A new aerodynamic parametrization for real urban surfaces. *Boundary-Layer Meteorol.* 148, 357–377. https://doi.org/10.1007/s10546-013-9818-x.

Kanda, M., Kanega, M., Kawai, T., Moriwaki, R., Sugawara, H., 2007. Roughness Lengths for Momentum and Heat Derived from Outdoor Urban Scale Models. *J. Appl. Meteor. Climatol.*, 46, 1067 - 1079

Karagulian, F., Belis, C.A., Dora, C.F.C., Prüss-Ustün, A.M., Bonjour, S., Adair-Rohani, H., Amann, M., 2015. Contributions to cities' ambient particulate matter (PM): A systematic review of local source contributions at global level. Atmos. Environ. 120, 475–483. https://doi.org/10.1016/j.atmosenv.2015.08.087

Kato, S., Yamaguchi, Y., Liu, C. C., Sun C. Y., 2008. Surface Heat Balance Analysis of Tainan City on March 6, 2001 Using ASTER and Formosat-2 Data. *Sensors*, 8, 6026 - 6044

Khan, Z., Ludlow, D., Mitraka, Z., Chrysoulakis, N., Feigenwinter, C., Marconcini, M., Lauwaet, D., Hooyberghs, H., Soukup, T., Jupova, K., Torres, E.F., Kjær-Hansen, L., 2020. CURE Project Deliverable D1.1 Summary of User Requirements.

Kljun, N., Calanca, P., Rotach, M.W., Schmid, H.P., 2015. A simple two-dimensional parameterisation for Flux Footprint Prediction (FFP). *Geosci. Model Dev.* 8, 3695–3713. https://doi.org/10.5194/gmd-8-3695-2015

Kohsiek W., De Bruin H.A.R., The H., van den Hurk B.J.J.M., 1993. Estimation of the sensible heat flux of a semi-arid area using surface radiative temperature measurements. *Boundary-Layer Meteorol*, 63, 213–230

Kolomaznik, J., Hlavacova, I., Lazecky, M., Pelant, M. (2016) TACR CZ Certified method for terrain movements and deformation monitoring on transport infrastructure by means of SAR Interferometry http://www.gisat.cz/download/projekt/TACR/GST-TB0400MD003_D3_v1-1.pdf, Technological Agency CZ (TACR)

Kolomaznik, J., Hlavacova, I., Stonacek, V., Lorenzo, A. (2020) Earth Observation for Sustainable development: Detailed terrain deformation analysis in urban areas, EO4SD Service Technical Report.

Kotthaus, S., Smith, T.E.L., Wooster, M.J., Grimmond, C.S.B., 2014. Derivation of an urban materials spectral library through emittance and reflectance spectroscopy. ISPRS J. Photogramm. Remote Sens. 94, 194–212. https://doi.org/10.1016/j.isprsjprs.2014.05.005

Lauwaet D., De Ridder K., Saeed S., Brisson E., Chatterjee F., van Lipzig N.P.M., Maiheu B., Hooyberghs H., 2016. Assessing the current and future urban heat island of Brussels. Urban Climate, 15, 1-15.

Lauwaet D., Hooyberghs H., Maiheu B., Lefebvre W., Driesen G., Van Looy S., De Ridder K., 2015. Detailed Urban Heat Island projections for cities worldwide: dynamical downscaling CMIP5 global climate models. Climate, 3, 391-415.

Lauwaet D., Maiheu B., De Ridder K., Boënne W., Hooyberghs H., Demuzere M., Verdonck M.-L., 2020. A New Method to Assess Fine-Scale Outdoor Thermal Comfort for Urban Agglomerations. Climate, 8, 6; doi:10.3390/cli8010006.

Lazecky, M., Bakon, M., Sousa, J. J., Perissin, D., Hlavacova, I., Patricio, G., Papco, J.,Rapant, P., Real, N. (2015) Potential of Multi-Temporal InSAR Techniques for Structural Health Monitoring, Proceedings of [FP1] FRINGE'15, http://proceedings.esa.int/files/324.pdf

Lazecky, M., Jirankova, E., Bohmova, D. (2010). Usage of insar techniques to detect and monitor terrain subsidence due to mining activities. https://www.researchgate.net/publication/277748130_Usage_of_insar_techniques_to_detect_and_monitor_terrain_subsidence_due_to_mining_activities

Lefebvre, W., Degraeuwe, B., Beckx, C., Vanhulsel, M., Kochan, B., Bellemans, T., Janssens, D., Wets, G., Janssen, S., De Vlieger, I., Int Panis, L., Dhondt, S., 2013b. Presentation and evaluation of an integrated model chain to respond to traffic- and health-related policy questions. Environ. Model. Softw. 40, 160–170.

Lefebvre, W., Van Poppel, M., Maiheu, B., Janssen, S., Dons, E., 2013a. Evaluation of the RIO-IFDM-street canyon model chain. Atmos. Environ. 77, 325–337. https://doi.org/10.1016/j.atmosenv.2013.05.026

Lefebvre, W., Vercauteren, J., Schrooten, L., Janssen, S., Degraeuwe, B., Maenhaut, W., de Vlieger, I., Vankerkom, J., Cosemans, G., Mensink, C., Veldeman, N., Deutsch, F., Van Looy, S., Peelaerts, W., Lefebre, F., 2011. Validation of the MIMOSA-AURORA-IFDM model chain for policy support: Modeling concentrations of elemental carbon in Flanders. Atmos. Environ. 45, 6705–6713. https://doi.org/10.1016/j.atmosenv.2011.08.033

Lemke B., Kjellstrom T. (2012) Calculating Workplace WBGT from Meteorological Data: A Tool for Climate Change Assessment. Industria Health 50, 267–278.

Leuning R, Kelliher FM, De Pury DGG, Schulze ED, *Plant. Cell Environ.* **18**, 1183–1200 (1995).

Li, H., Zhou, Y., Li, X., Meng, L., Wang, X., Wu, S., Sodoudi, S. (2018). A new method to quantify surface urban heat island intensity. Science of The Total Environment 624, 262–272.

Liljegren J.C., Carhart R.A., Lawday P., Tschopp S., Sharp R. (2008) Modeling the Wet Bulb Globe Temperature Using Standard Meteorological Measurements. Journal of Occupational and Environmental Hygiene 5(10), 645-655. DOI:10.1080/15459620802310770.

Lindberg, F., Grimmond, C.S.B., Gabey, A., Huang, B., Kent, C.W., Sun, T., Theeuwes, N.E., Järvi, L., Ward, H.C., Capel-Timms, I., Chang, Y., Jonsson, P., Krave, N., Liu, D., Meyer, D., Olofson, K.F.G., Tan, J., Wästberg, D., Xue, L., Zhang, Z., 2018. Urban Multi-scale Environmental Predictor (UMEP): An integrated tool for city-based climate services. *Environ. Model. Softw.* 99, 70–87. https://doi.org/10.1016/j.envsoft.2017.09.020

Marconcini, M., Gorelick, N., Metz-Marconcini, A., Esch, T. (2018). Mapping the Global Settlement Growth from 1985 to 2015 - the World Settlement Footprint Evolution Dataset. 2018 AGU Fall Meeting Conference Paper

Marconcini, M., Metz-Marconcini, A., Üreyen, S. et al. Outlining where humans live, the World Settlement Footprint 2015. Sci Data 7, 242 (2020).

Minderhoud, P. S. J., Hlavacova, I., Kolomaznik, J., and Neussner, O.: Towards unraveling total subsidence of a mega-delta – the potential of new PS InSAR data for the Mekong delta, Proc. IAHS, 382, 327–332, https://doi.org/10.5194/piahs-382-327-2020, 2020

Mitraka, Z., Chrysoulakis, N., Doxani, G., Del Frate, F., Berger, M., 2015. Urban Surface Temperature Time Series Estimation at the Local Scale by Spatial-Spectral Unmixing of Satellite Observations. Remote Sens. 7, 4139–4156. https://doi.org/10.3390/rs70404139

Mitraka, Z., Chrysoulakis, N., Kamarianakis, Y., Partsinevelos, P., Tsouchlaraki, A., 2012. Improving the estimation of urban surface emissivity based on sub-pixel classification of

high resolution satellite imagery. Remote Sens. Environ. 117, 125–134. https://doi.org/10.1016/j.rse.2011.06.025

NASA/METI/AIST/Japan Spacesystems, and U.S./Japan ASTER Science Team. ASTER Level 2 Surface Temperature Product. 2001, distributed by NASA EOSDIS Land Processes DAAC, https://doi.org/10.5067/ASTER/AST_08.003. Accessed 2020-12-10.

Offerle, B., Grimmond, C. S. B, Oke, T. R. 2003. Parameterization of Net All-Wave Radiation for Urban Areas, *Journal of Applied Meteorology*, 42(8), pp. 1157–1173. doi: 10.1175/1520-0450(2003)042<1157:PONARF>2.0.CO;2.

Offerle, B., Grimmond, C.S.B.B., Fortuniak, K., 2005. Heat storage and anthropogenic heat flux in relation to the energy balance of a central European city centre. Int. J. Climatol. 25, 1405–1419. https://doi.org/10.1002/joc.1198

Oke, T.R., Mills, G., Christen, A., Voogt, J.A., 2017. Urban Climates. Cambridge University Press, Cambridge. https://doi.org/10.1017/9781139016476

Parastatidis, D., Mitraka, Z., Chrysoulakis, N., Abrams, M., 2017. Online Global Land Surface Temperature Estimation from Landsat. Remote Sens. 9, 1208. https://doi.org/10.3390/rs9121208

Pepe, A., Calò, F. (2017) A review of interferometric synthetic aperture RADAR (InSAR) multi-track approaches for the retrieval of Earth's surface displacements Appl. Sci., 7 (12), 1264: https://www.mdpi.com/2076-3417/7/12/1264/htm

Pope CA, Burnett RT, Thun MJ, Calle EE, Krewski D, Ito K, Thurston GD. Lung cancer, cardiopulmonary mortality and long-term exposure to fine particulate air pollution. JAMA-J Am Med Assoc. 2002;287:1132–1141.

Poursanidis, D., Mitraka, Z., Somarakis, G., Dohr, M., Chrysoulakis, N., 2020. CURE Project Deliverable D7.4 Data Management Plan.

Stagakis, S., Chrysoulakis , N., Spyridakis , N., Feigenwinter, C., Vogt, R., 2019. Eddy Covariance measurements and source partitioning of CO_2 emissions in an urban environment: Application for Heraklion, Greece . *Atm. Environ*., 201, 278-292. https://doi.org/10.1016/j.atmosenv.2019.01.009

U.S. Army (2003) Technical Bulletin Medical 507 and Air Force Pamphlet 48-152(I). Heat stress control and heat casualty management.

Voogt, J.A., Grimmond, C.S.B., 2000. Modeling Surface Sensible Heat Flux Using Surface Radiative Temperatures in a Simple Urban Area. *J. Appl. Meteorol.* 39, 1679–1699. https://doi.org/10.1175/1520-0450-39.10.1679

Ward, H. C. *et al.* (2016) 'Surface Urban Energy and Water Balance Scheme (SUEWS): Development and evaluation at two UK sites', *Urban Climate*, 18, pp. 1–32. doi: 10.1016/j.uclim.2016.05.001.

WHO, 2016. Ambient air pollution: A global assessment of exposure and burden of disease. URL: https://www.who.int/publications/i/item/9789241511353

WHO. Health risks of air pollution in Europe – HRAPIE: Recommendations of concentration-response functions for cost-benefit analysis of particulate matter, ozone and nitrogen dioxide. World Health Organization; [last access: 25 April 2018]. 2013. available at: http://www.euro.who.int/__data/assets/pdf_file/0006/238956/Health_risks_air_pollutio n_HRAPIE_project.pdf?ua=1.

Willett, K. M. & Sherwood, S. (2012) Exceedance of heat index thresholds for 15 regions under a warming climate using the wet-bulb globe temperature. Int. J. Climatol., 32, 161–177.

Yoshida, A., Tominaga, K. and Watatani, S. (1990) 'Field measurements on energy balance of an urban canyon in the summer season', *Energy and Buildings*, 15(3–4), pp. 417–423. doi: 10.1016/0378-7788(90)90016-C.

Yoshida, A., Tominaga, K. and Watatani, S. (1991) 'Field investigation on heat transfer in an urban canyon', *Heat Transfer - Japanese Research; (United States)*. Available at: https://www.osti.gov/biblio/5496556.

Zhou B., Lauwaet D., Hooyberghs H., De Ridder K., Kropp J. P., Rybski D., 2016. Assessing seasonality in the surface urban heat island of London. Journal of Applied Meteorology and Climatology, 55, 493-505.